Ricci Flow And Its Applications

A Dissertation presented

by

Min Zhang

to

The Graduate School

in Partial Fulfillment of the

Requirements

for the Degree of

Doctor of Philosophy

in

Computer Science

Stony Brook University

December 2014

Stony Brook University

The Graduate School

Min Zhang

We, the dissertation committe for the above candidate for the

Doctor of Philosophy degree, hereby recommend

acceptance of this dissertation

Xianfeng Gu - Dissertation Advisor
Associate Professor, Computer Science Department

Jie Gao - Chairperson of Defense
Associate Professor, Computer Science Department,Stony Brook University

Long Lu, Assistant Professor, Computer Science Department, Stony Brook University

Feng Luo, Professor, Department of Mathematics, Rutgers University

This dissertation is accepted by the Graduate School

Charles Taber
Dean of the Graduate School

Abstract of the Dissertation

Ricci Flow and Its Applications

by

Min Zhang

Doctor of Philosophy

in

Computer Science

Stony Brook University

2014

Abstract

This thesis introduces the Ricci Flow and Its applications. Ricci flow has demonstrated its great potential by solving various problems in many fields, which can be hardly handled by alternative methods so far. General Ricci flow is defined on arbitrary dimensional Riemannian manifolds. Surface (2-manifold) Ricci flow has unique characteristics, which are crucial for developing discrete theories and designing computational algorithms.

The unified theoretic framework for discrete Surface Ricci Flow is innovated, including all the common schemes: Tangential Circle Packing, Thurston's Circle Packing, Inversive Distance Circle Packing and Discrete Yamabe Flow. Furthermore, we also introduce novel schemes, Virtual Radius Circle Packing and the Mixed Type schemes, under the unified framework. It gives explicit geometric interpretation to the discrete Ricci energies for all the schemes with all back ground geometries, and the corresponding Hessian matrices. The unified frame work deepens our understanding to the discrete surface Ricci flow theory, and has inspired us to discover the new schemes, improved the flexibility and robustness of the algorithms, greatly simplified the implementation and improved the efficiency.

Ricci flow has a lot of applications. Some are introduced in this thesis. First, Combine the Ricci flow and koebe's iteration for computing the canonical mapping for uniformizaiton of open surfaces, and give the theoretical proof of convergence. Second, a novel shape signature based on surface Ricci flow and optimal mass transportation is introduced for the purpose of surface comparison. Third, consider Ricci flow as conformal visualization technique and applied to immersive systems such as the CAVE. We can establishes a conformal mapping between the full 360 degree field of view and the display geometry of a given visualization system.

The major challenges of visualizing the abstract Ricci curvature are to represent the intrinsic Riemannian metric of a surface by extrinsic embedding in the three dimensional Euclidean space and demonstrate the deformation process which preserves the conformal structure. A series of rigorous and practical algorithms are introduced to tackle the problem.

Keywords: Ricci Flow, Discrete Ricci Flow, Ricci energy, Conformal mapping, Gauss curvature, Poincaré conjecture, Uniformization, Curvature, Metric, Surface parameterization, Hessian matrix.

Contents

List of Figures

Acknowledgements

Foremost, I would like to express my sincere gratitude to my advisor Prof. Xianfeng Gu for the continuous support of my Ph.D study and research, for his patience, motivation, enthusiasm, and immense knowledge. His guidance helped me in all the time of research and writing of this thesis. I could not have imagined having a better advisor and mentor for my Ph.D study.

I would like to thank the rest of my thesis committee: Prof. Feng Luo, Prof. Jie Gao, and prof.Long Lu, for their encouragement and insightful comments.

A special thanks to Prof. Shing-tung Yau and Prof. Kefeng Liu, who taught me mathematics and introduced me to the fields "Conformal Geometry". I would also like to all the faculties and staffs in Computer Science department, Stony Brook university. who give me a lot of help during my Ph.D study and research. Thank you very much, Prof. Arie E. Kaufman, Prof. I.V. Ramakrishnan, Prof. Hong Qin, Prof. Jie Gao, Prof. Michael Bender, Prof. Long Lu, Prof. Himanshu Gupta, Prof. Eugene Stark, Prof. Larry Wittie, Prof. Anita Wasilewska, Prof. Annie Liu, Prof. Ellen Liu, etc.

I thank my fellow labmates in 3D Scanning Lab, Wei Zeng, Xiang Zeng, Xiaotian Yin, Ruirui Jiang, Rui Shi, Zhengyu Su, Hao Peng, Yuyao Lin, Junwei Zhang, Jian Jiang, Ming Ma, Xiao Cui. for the stimulating discussions, for the sleepless nights we were working together before deadlines, and for all the fun we have had in the past years. I also wanted to thank all my friends who incented me to strive towards my goal.

A special thanks to my family. Words cannot express how grateful I am to my parents. Your support for me was what sustained me thus far.

Vita, Publications and/or Fields of Study

Scientific Publications:

- Generalized Koebe's method for conformal mapping multiply connected domains. *SPM '09 2009 SIAM/ACM Joint Conference on Geometric and Physical Modeling*
- Conformal Visualization for Partially-Immersive Platforms. *2011 IEEE Virtual Reality and 2011 IEEE TVCG*
- Canonical conformal mapping for high genus surfaces with boundaries.*2012 Shape Modeling International (SMI) Conference and Computers and Graphics*
- Stable Geodesic Surface Signatures. *2012 Tsinghua Science and Technology*
- Visualization of 2-dimensional Ricci Flow. *2013 Pure and Applied Mathematics Quarterly*
- Shape Signature based on Ricci Flow and Optimal Mass Transportation. *2014 Optical Engineering*
- The Unified Ricci flow. *2014 Geometric Modeling and Processing and 2014 Graphical Models*

Chapter 1

Introduction

Ricci flow deforms the Riemannian metric proportionally to the curvature, such that the curvature evolves according to a heat diffusion process and eventually becomes constant everywhere. Ricci flow is a powerful tool in geometric analysis for studying low dimensional topology. It has been successfully applied for the proofs of Poincaré's conjecture and Thurstonąŕs geometrization conjecture. Recently, Ricci flow has started making impacts on practical fields and tackling fundamental engineering problems.

General Ricci flow is defined on arbitrary dimensional Riemannian manifolds. Surface (2-manifold) Ricci flow has unique characteristics, which are crucial for developing discrete theories and designing computational algorithms. First, surface Ricci flow never blows up, namely, the Gauss curvature during the flow is always bounded. This phenomenon ensures the numerical stability of discrete surface Ricci flow. In contrast, 3-manifold Ricci flow will produce singularities, thus topological surgery is unavoidable. Second, surface Ricci flow is conformal, namely, the deformation of the Riemannian metric preserves angles. This fact greatly simplifies both theoretical arguments and algorithmic designs. General Ricci flow is governed by tensor differential equations, whereas surface Ricci flow is described by scalar differential equations. Third, surface Ricci flow has intuitive geometric interpretations, which directly lead to the design of data structures. A conformal deformation transforms infinitesimal circles to infinitesimal circles. This elucidates the geometric nature of the flow. Finally, Ricci flow is variational, namely, Ricci flow is the negative gradient flow of Ricci energy. Accordingly, discrete surface Ricci flow can be formulated as a convex optimization problem, which has a unique global optimum and can be carried out using the efficient Newton's method.

Ricci flow has demonstrated its great potential by solving various problems in many fields, which can be hardly handled by alternative methods so far.

In this Chapter, Firstly, I will give a brief introduction about some fundamental Mathematical Concepts and brief introduction about general Ricci Flow, which leads to the celebrated uniformization theorem. Then I will give the overview of this thesis.

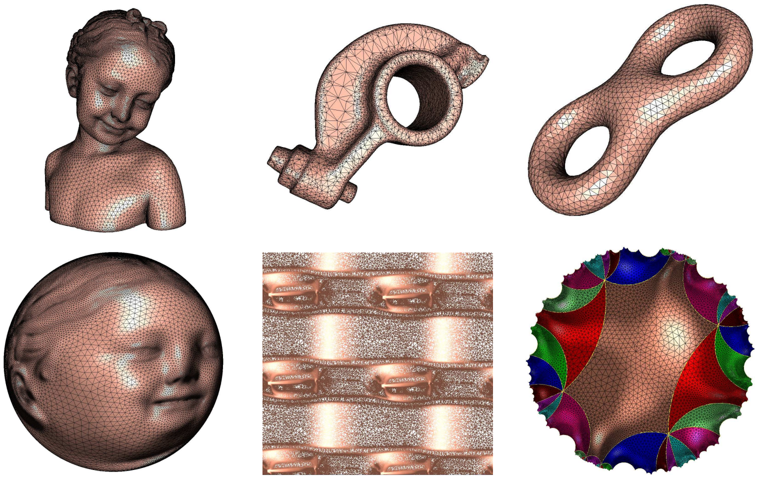

Figure 1.1: Uniformization for closed surfaces by Ricci flow.

1.1 Basic Concepts

1.1.1 Ricci Flow

Curvatures are determined by Riemannian metrics. One natural question to ask is whether the metric can be determined by the curvature. In practice, it is highly desirable to design Riemannian metrics with the user prescribed curvatures. Hamilton's Ricci flow is a powerful tool to achieve such a goal. On surfaces, Hamilton defined the Ricci flow as

$$\frac{dg_{ij}(t)}{dt} = -2K(t)g_{ij}(t),$$

where $g_{ij}(t)$ and $K(t)$ are functions of time t, $K(t)$ is the Gaussian curvature induced by $g_{ij}(t)$. Basically, Ricci flow deforms the Riemannian metric proportional to the curvature, such that the curvature evolves according to a nonlinear heat diffusion process, and eventually becomes constant everywhere. The curvature flow is represented as

$$\frac{dK(t)}{dt} = \Delta_{g(t)}K(t) + 2K(t)^2,$$

where $\Delta_{g(t)}$ is the Laplace-Beltrami operator induced by the metric $g(t)$. Hamilton and Chow proved that during the flow, the curvature $K(t)$ is always finite, never blows up, and when time goes to infinity, the curvature converges to constant, $K(\infty) \to const$. This leads to the celebrated *uniformization theorem*, which says all surfaces in real life can be deformed to one of three canonical spaces, the sphere $\mathbb{S}^2$, the plane $\mathbb{E}^2$ or the hyperbolic disk $\mathbb{H}^2$.

Surfaces with boundaries can be uniformized to the canonical spaces with circular boundaries. Figure 1.2 demonstrates the uniformization for surfaces with boundaries.

The uniformization transforms all the shapes in real life to canonical ones, and converts all 3D surface geometric processing problems to 2D planar problems. This greatly simplifies most of the

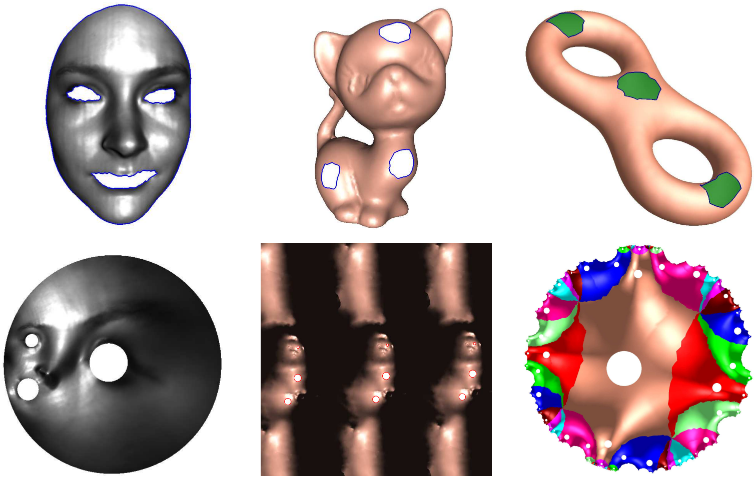

Figure 1.2: Uniformization for surfaces with boundaries by Ricci flow.

computational tasks and improves the efficiency and efficacy. The mappings among all surfaces can be easily established by composing the mappings from the surfaces to the canonical spaces (uniformization transformations) and the automorphisms of the canonical spaces. This allows different shapes to be matched, registered, tracked and compared.

1.1.2 Mappings among Manifolds

Suppose M_1 and M_2 are two manifolds, with local charts (U_α, ϕ_α) and (V_β, ψ_β), respectively. A mapping $f: M_1 \to M_2$ has local representation,

$$\psi_\beta \circ f \circ \phi_\alpha^{-1} : \phi_\alpha(U_\alpha) \to \psi_\beta(V_\beta).$$

For the convenience, we denote $\psi_\beta \circ f \circ \phi_\alpha^{-1}$ as f_α^β. Assume the local coordinates on $\phi_\alpha(U_\alpha)$ are (x,y), on $\psi_\beta(V_\beta)$ are (u,v), then $(u,v) := f_\alpha^\beta(x,y)$.

Homeomorphism

If all the local representations f_α^β are homeomorphisms, namely continuous and invertible and their inverses are also continuous, then f is called a *homeomorphism* between the two manifolds, and we say M_1 and M_2 are *topologically equivalent*.

Diffeomorphism

Similarly, if all the local representations f_α^β are orientation preserving diffeomorphisms, namely, the determinant of the Jacobian matrix is positive everywhere,

$$\left|\frac{\partial(u,v)}{\partial(x,y)}\right| := \left|\begin{array}{cc} \frac{\partial u}{\partial x} & \frac{\partial v}{\partial x} \\ \frac{\partial u}{\partial y} & \frac{\partial v}{\partial y} \end{array}\right| > 0,$$

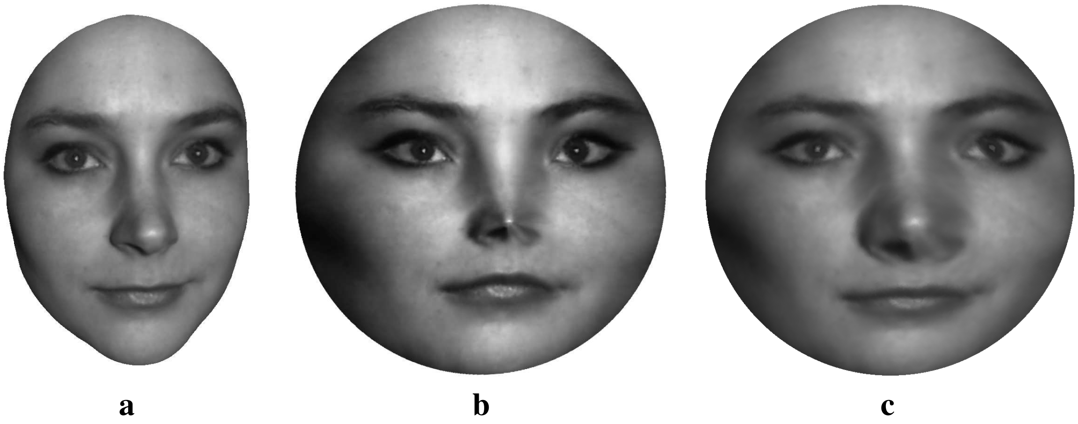

Figure 1.3: Diffeomorphisms.
a. A 3D human face surface, **b.** An angle preserving (conformal) mapping, **c.** An area preserving mapping

then we say f is a *diffeomorphism*, and the two manifolds are *diffeomorphically equivalent*.

Suppose the Riemannian metric on M_1 is $\mathbf{g}_1 = g^1_{11}dx^2 + 2g^1_{12}dxdy + g^1_{22}dy^2$, $\mathbf{g}_2 = g^2_{11}du^2 + 2g^2_{12}dudv + g^2_{22}dv^2$. A curve $C(t)$ on the source M_1 is mapped to a curve $f \circ C(t)$ on the target M_2, and its length can be measured by the metric $\mathbf{g}_2$. We can define the length of $C(t) \subset M_1$ as that of $f \circ C(t)$ on M_2, this gives another Riemannian metric on M_1, which is called the *pull back metric* induced by f, and denoted as $f^*\mathbf{g}_2$.

Definition 1 (Pull Back Metric). *Suppose $f : (M_1, \mathbf{g}_1) \to (M_2, \mathbf{g}_2)$ be a mapping between two Riemannian manifolds. The pull back metric induced by f has the local representation*

$$f^*\mathbf{g}_2 = \left[\frac{\partial(u,v)}{\partial(x,y)}\right]^T \mathbf{g}_2 \left[\frac{\partial(u,v)}{\partial(x,y)}\right].$$

Isometric Mapping

Suppose the mapping f is a diffeomorphism, and the pull back metric induced by f equals to the original metric

$$f * \mathbf{g}_2 = \mathbf{g}_1.$$

Then the mapping is called an *isometry*. Isometric mappings preserve lengths.

Conformal Mapping

Suppose the pull back metric induced by a diffeomorphism f satisfies

$$f^*\mathbf{g}_2 = e^{2\lambda}\mathbf{g}_1, \tag{1.1.1}$$

where $\lambda : M_1 \to \mathbb{R}$ is a function defined on M_1. Then the mapping f is called a *conformal mapping* and $e^{2\lambda}$ is called the *conformal factor*. We can conclude that a conformal mapping preserves angles.

Area Preserving Mapping

Suppose the pull back metric satisfies the following condition,

$$det(f^*\mathbf{g}_2) = det(\mathbf{g}_1).$$

Then the mapping is called an *area preserving mapping*, which preserves area element.

It is obvious that isometry is both angle preserving (conformal) and area preserving. The inverse is also true, if a mapping is both conformal and area preserving, then it must be isometric.

Rigid Motion

Suppose both M_1 and M_2 are embedded in the Euclidean space $\mathbb{E}^n$, f is a rotation composed with a translation in $\mathbb{E}^n$. Then f is called a *rigid motion*.

In each category discussed above, all the mappings form a transformation group. For example, considering all the angle preserving mappings, if f, g are two conformal mappings, then their compositions $g \circ f$ is still conformal; if f is conformal, then its inverse f^{-1} is conformal; identity map is also conformal. Hence all conformal mappings form a transformation group.

Figure 1.3 demonstrates angle preserving and area preserving mappings from a human face surface onto the planar disk. The left frame is the original facial surface, captured using a 3D scanner. The middle frame is the image of a conformal mapping. Conformal mapping can be interpreted as local scaling transformations, so local shapes are well preserved. The right frame shows the area preserving mapping, which preserves the area element.

1.1.3 Shape Space

We consider the space of all possible shapes, here shapes may refer to all one dimensional contours on the plane, or all surfaces embedded in three dimensional Euclidean space. We may assume their volumes are finite and compact. We denote the shape space as $\mathfrak{M}$, for example:

$$\mathfrak{M} = \{S \hookrightarrow \mathbb{E}^3\},$$

where S is a compact, orientable surface, embedded in $\mathbb{E}^3$.

Let G be a transformation group that acts on the shape space $\mathfrak{M}$, such as conformal transformations, $g(S)$ is another surface, denoted as a pair (g, S),

$$G \times \mathfrak{M} \to \mathfrak{M}, (g, S) \in \mathfrak{M}.$$

The orbits of G in $\mathfrak{M}$ can be defined as *equivalence classes*

$$[S] = \{(g, S) | g \in G\}.$$

For example, if G is the conformal transformation group, then each conformal equivalence class $[S]$ is called a *Riemann surface*.

The quotient space $\mathfrak{M}/G$ is the set of such equivalence classes

$$\mathfrak{M}/G = \{[S] | S \in \mathfrak{M}\}.$$

The space of all Riemann surfaces (with the same topology) is called the *moduli space*. The topology of Moduli space is complicated. Instead, we study its universal covering space, the so-called *Teichmüller space*. For genus $g > 1$ closed surfaces, the Teichmüller space is a $6g-6$ manifold. We can design Riemannian metric for the quotient space $\mathfrak{M}/G$, and measure the distances among orbits. The distance between two Riemann surfaces in Teichmüller space is given by the so called Teichmüller map, which is unique and minimizes the angle distortion. The distance is defined as the logarithm of the dilatation of the Teichmüller map, where the dilation is a measurement of angle distortions. Therefore, Teichmüller spaces are Riemannian manifolds.

In general, if $\mathfrak{M}$ has a Riemannian metric, the action of G on $\mathfrak{M}$ is isometric, namely $g \in G$, $S_1, S_2 \in \mathfrak{M}$,

$$d_{\mathfrak{M}}(S_1, S_2) = d_{\mathfrak{M}}(g(S_1), g(S_2)),$$

then the geodesic distance in the quotient space $\mathfrak{M}/G$ is given by

$$d_{\mathfrak{M}/G}([S_1],[S_2]) = \min_{g \in G} d_{\mathfrak{M}}(S_1, g(S_2)).$$

1.1.4 Mapping Space

For practical purposes, we are only interested in diffeomorphisms (generally, approximated by homeomorphisms). The diffeomorphic mappings between two surfaces also form a space, which we call *mapping space*. The mapping space is of infinite dimension. Given the source surface S_1 and the target surface S_2, all the mappings can be classified by their homotopy types. Fixing the homotopy class, each diffeomorphism $f : S_1 \to S_2$ corresponds to a unique complex function (or complex differential) μ_f, $\|\mu_f\|_\infty < 1$, called the *Beltrami coefficient* (or *Beltrami differential*) of the mapping f.

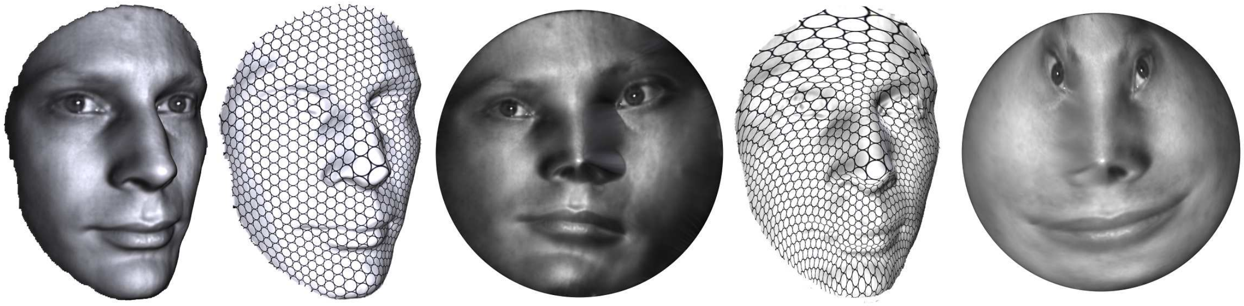

Figure 1.4: Diffeomorphisms and Beltrami coefficients

Figure 1.4 explains the geometric meaning of the concept of Beltrami coefficient. A diffeomorphism maps infinitesimal circles on the source surface to infinitesimal ellipses on the target.

The eccentricity of the ellipse at point p (ratio between the major axis and the minor axis) and the orientation (angle between the major axis and the horizontal direction) are encoded to a complex number $\mu(p)$. Note that, the size of the ellipse is not encoded, therefore the Beltrami coefficient has less information than the Jacobian matrix of the mapping.

Amazingly, the diffeomorphism can be fully recovered from its Beltrami coefficient. Essentially, each Beltrami coefficient μ uniquely determines a diffeomorphism. This converts the mapping space to a complex functional space $\{\mu|\mu : S_1 \to \mathbb{C}, \|\mu\|_\infty < 1\}$. Furthermore, the diffeomorphism f^μ depends on μ smoothly. The variation of the mapping with respect to the variation of its Beltrami coefficient has an explicit analytic relation. This allows us to perform optimization in the mapping space.

In practice, several special types of mappings are commonly used: harmonic mappings, which minimize the membrane energy; biharmonic mappings, which minimize the elastic energy; conformal mappings, which preserve angles; extremal quasi-conformal mappings, which minimizes the angle distortions; and area preserving mappings, which preserve area elements.

1.2 Computational Methodology

We briefly introduce the surface classification, registration and comparison based on Ricci flow.

1.2.1 Surface Classification

Surfaces are classified by different transformation groups. One transformation group G acts on the shape space $\mathfrak{M}$, and classifies the shape space to orbits, the orbits form the quotient space $\mathfrak{M}/G$. Different transformation groups correspond to different geometries, require different theoretical tools and computational methodologies.

Homeomorphism Group

The quotient space $\mathfrak{M}/G$ is a discrete point set. Two surfaces are in the same topological equivalence class, if and only if they have the same genus g, same number of boundary components b.

In practice, the surfaces are represented by polyhedral surfaces. The Euler characteristic number is given by

$$\chi(S) := 2 - 2g - b,$$

which can be computed by $\chi(S) = V + F - E$, where V, E, F are the number of vertices, edges and faces of the polyhedron surface. The number b of boundary components can be calculated by tracing the boundary edges, then the genus g can be obtained.

The computational algorithms are designed mainly based on algebraic topology.

Conformal Transformation Group

The quotient space $\mathfrak{M}/G$ is a finite dimensional space, which is the Teichmüller space. Two surfaces are conformally equivalent if and only if they share the same conformal module.

By using Ricci flow, we can compute the uniformizations of surfaces, and conformally map the surfaces to canonical domains, or circle domains on canonical spaces. Two surfaces are conformally equivalent, if and only if their images on canonical domains are isometric.

The conformal mappings from the surfaces to canonical domains. All genus zero closed surfaces can be conformally mapped to the unit sphere, so are conformally equivalent; all genus one surfaces can be mapped to a flat torus, which is the Euclidean plane $\mathbb{E}^2$ quotient a lattice Λ,

$$\mathbb{E}^2/\Lambda, \Lambda = \{m + n\omega m, n \in \mathbb{Z}\}, \omega \in \mathbb{C}.$$

Two points $p, q \in \mathbb{E}^2$ are equivalent if and only if $p - q \in \Lambda$. The Lattice parameter ω is the total conformal module. Similarly, all high genus surfaces with hyperbolic metric can be represented as $\mathbb{H}^2/\Lambda$, where Λ is a subgroup of hyperbolic isometry group, the so called *Möbius transformation group*. The group Λ is finitely generated by $2g$ generators. The conformal module is given by these generators.

Similarly, compact metric surfaces with boundaries can be deformed the circle domains on canonical spaces

$$\{\mathbb{S}^2, \mathbb{E}^2, \mathbb{H}^2\}/\Lambda - \cup_k D_k,$$

where D_k's are circles. The generators of Λ and the centers and radii of D_k's form the conformal module of the surface.

The computational algorithms are based on Ricci flow in geometric analysis and Riemann surface theory.

Isometry Group

If two surfaces $(S_1, \mathbf{g}_1), (S_2, \mathbf{g}_2)$ are isometrically equivalent, they must be conformally equivalent. Let $f_k : S_k \to D, k = 1, 2$ are the conformal mappings induced by Ricci flow, where D is the canonical space, let the Riemannian metric on D is $\mathbf{g}_0$, and

$$f_1^*\mathbf{g}_0 = e^{2\lambda_1}\mathbf{g}_1, f_2^*\mathbf{g}_0 = e^{2\lambda_2}\mathbf{g}_2.$$

Two surfaces are isometric if and only if we can choose f_1 and f_2, such that $\lambda_1 \equiv \lambda_2$.

The computational algorithms are based on surface differential geometry and Riemannian geometry.

Rigid Motion Group

Suppose two surfaces$(S_1, \mathbf{g}_1), (S_2, \mathbf{g}_2)$ differ by a rigid motion. We can find two conformal mappings $f_k : S_k \to D$ which map the surface onto the canonical domain, such that the corresponding conformal factor functions and mean curvature functions are equal,

$$\lambda_1 \circ f_1^{-1} \equiv \lambda_2 \circ f_2^{-1}, H_1 \circ f_1^{-1} \equiv H_2 \circ f_2^{-1}.$$

Geometric Structure	Transformations	Geometry	Main Representation
Second Fundamental Form	Rigid Motion	Differential Geometry	Mean Curvature H
Riemannian metric	Isometry	Riemannian Geometry	Conformal Factor λ
Conformal Structure	Conformal Mapping	Conformal Geometry	Conformal Module
Topological Structure	Homeomorphism	Topology	Fundamental Group π_1

Table 1.1: Surface hierarchical geometric structures

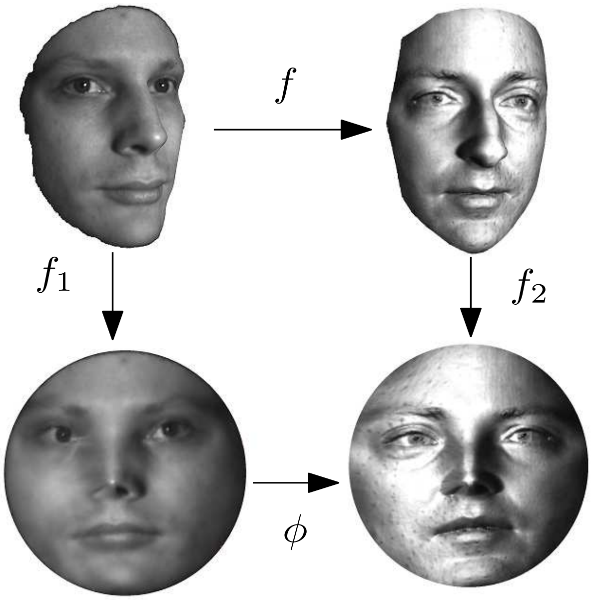

Figure 1.5: Computational framework for surface registration

The computational algorithms are based on surface differential geometry.

Table 1.1 summarizes the geometric structures for a surface embedded in $\mathbb{E}^3$. Each geometric structure corresponds to a geometry, and has a special representation. All the geometric structures form a hierarchy, the higher level structure is based on lower level ones, and represented as functions on lower level structures.

1.2.2 Surface Registration

Figure 1.5 explains the framework for surface registration. By using Ricci flow, two surfaces are mapped to the uniformization domains, $f_k : S_k \to \mathbb{D}$. We then compute a self mapping $\phi : \mathbb{D} \to \mathbb{D}$, then the registration between two surfaces is given by the composition

$$f_2^{-1} \circ \phi \circ f_1 : S_1 \to S_2.$$

Initially, the mapping ϕ can be chosen as a harmonic map between the canonical domains. If both the source and the target are closed genus zero surfaces, then the canonical domain is the unit sphere. Harmonic mapping ϕ must be a Möbius transformation; if the input shapes are genus zero surfaces with a single boundary, then the canonical domain is the unit disk, if the boundary mapping is a homeomorphism, the interior harmonic mapping is diffeomorphic; if the input shapes are genus one closed surfaces, then the canonical domains are flat torii, the harmonic mapping is an affine mapping; if the input surfaces are of high genus, then the canonical domains are hyperbolic surfaces. Harmonic maps between hyperbolic surfaces exist, and are unique in each homotopy class, and diffeomorphic.

The mapping can be further optimized by minimizing various energies, such as the one defined in (1.2.1). Other criteria can be added to the energy, such as the feature correspondence constraints, smoothness of the mapping, texture consistency, temporal consistency, prior knowledge about the mappings, and so on. The optimization can be performed in the diffeomorphism space of the canonical space. The variational calculus can be performed using quasi-conformal geometric method. If we choose the energy as the distortion of the global conformal structure, then the optimal mapping is the classical Teichmüller mapping.

1.2.3 Shape Comparison

By using Ricci flow, a metric surface $(S,\mathbf{g})$ is conformally deformed to the canonical space $f: S \to \mathbb{D}$. The uniformization gives a special surface parameterization, the so-called *isothermal coordinates* (x,y). Under the isothermal coordinates, the Riemannian metric tensor becomes a scalar $\mathbf{g} = e^{2\lambda}(dx^2+dy^2)$. All the geometric operators have the simplest forms under isothermal coordinates, such as the gradient $\nabla_{\mathbf{g}} = e^{-\lambda}(\frac{\partial}{\partial x}, \frac{\partial}{\partial y})^T$, the Laplace-Beltrami operator $\Delta_{\mathbf{g}} = e^{-2\lambda}(\frac{\partial^2}{\partial x^2} + \frac{\partial^2}{\partial y^2})$. This improves the efficiency for extracting local geometric features, such as the Gauss curvature

$$K = -\Delta_{\mathbf{g}}\lambda,$$

and the mean curvature

$$H = \langle \Delta_{\mathbf{g}}\mathbf{r}(x,y), \mathbf{n}(x,y)\rangle,$$

where $\mathbf{r}(x,)$ and $\mathbf{n}(x,y)$ are the position vector and the normal of the surface, the principle curvatures $k_1, k_2 = H \pm \sqrt{H^2 - K}$, shape index, geodesics, and so on.

The conformal module induced by Ricci flow are global shape features. The shortest geodesics in each homotopy class under the uniformization metric form the geodesic spectrum, which gives a global shape descriptor as well. The dynamics of the curvatures during Ricci flow can be also applied as a multi-resolution shape descriptor. Furthermore, Ricci flow preserves intrinsic symmetry of the surface, it can be applied for detecting global symmetry under the uniformization metric.

Various distances between two shapes $(S_1,\mathbf{g}_1)$ and $(S_2,\mathbf{g}_2)$ can be defined. Let $f_k: S_k \to \mathbb{D}$ be the uniformization transformation using Ricci flow, then the distance between the two surfaces is given by

$$d(S_1,S_2) = \int_{\mathbb{D}} (\lambda_1 \circ f_1^{-1} - \lambda_2 \circ f_2^{-1})^2 + (H_1 \circ f_1^{-1} - H_2 \circ f_2^{-1})^2 dxdy.$$

The distance is zero if and only if two surfaces differ by a rigid motion. If the first term is zero, then two surfaces are isometric. In practice, we can find an automorphism of the canonical space

$\mathbb{D}$, $\phi : \mathbb{D} \to \mathbb{D}$, such that the distance is the minimizer,

$$d(S_1, S_2) = \min_{\phi} \int_{\mathbb{D}} (\lambda_1 \circ f_1^{-1} - \lambda_2 \circ f_2^{-1} \circ \phi)^2 + (H_1 \circ f_1^{-1} - H_2 \circ f_2^{-1} \circ \phi)^2 dxdy. \tag{1.2.1}$$

1.3 Thesis Overview

This thesis is mostly devoted framework of discrete surface ricci flow and also some applications related to discrete surface ricci flow. Chapter 2 briefly reviews the fundamental concepts and theorems in algebraic topology, surface differential geometry and surface Ricci flow. Chapter 3 introduces the discrete surface Ricci flow theory [76]. Chapter 4 give the unified theoretic framework for discrete Surface Ricci Flow [78]. Chapter 5 aims at visualizing the abstract Ricci curvature flow partially using the recent work of Izmestiev [18]. Chapter 6 applied ricci flow and Koebe's iteration method to compute Conformal map of High-Genus open surface [61]. Chapter 7 create a novel shape signature based on surface Ricci flow and optimal mass transportation is introduced for the purpose of surface comparison [54]. Chapter 8 applied the Ricci flow method to immersive systems such as the CAVE, establishing a conformal mapping between the full 360 degree field of view and the display geometry of a given visualization system [46].

Chapter 2

Theoretical Background

This chapter briefly reviews the fundamental concepts and theorems in algebraic topology [7], surface differential geometry [21], and surface Ricci flow [13, 35]. Detailed discussion on Ricci flow on general Riemannian manifolds can be found in [14]. Advanced topics on differential geometry related to Yamabe equations can be found in [67].

2.1 Surface Topology

Topology studies the invariants under homeomorphism transformation group. Algebraic topology studies the topologies of spaces and the mappings among spaces by algebraic means. Generally, different groups are associated with different spaces, such as fundamental group, homology group, and cohomology group. The structures of these groups convey the topological information about the spaces. The homomorphisms among these groups reflect the properties of the mappings among the spaces. In reality, most surfaces are the boundaries of some finite volumes, therefore, they are compact and orientable. In the following, we focus on the fundamental groups and covering spaces of compact orientable surfaces.

Definition 2 (Connected Sum)**.** *The connected sum* $S_1 \# S_2$ *is formed by deleting the interior of disks* $D_i \subset S_i$ *and attaching the resulting punctured surfaces* $S_i - D_i$ *to each other by a homeomorphism* $h : \partial D_1 \to \partial D_2$*, where* ∂D_i *represents the boundary of* D_i*. Let* $p \in \partial D_1$ *and* $q \in \partial D_2$*,* p *is equivalent to* q*,* $p \sim q$ *if* $q = h(p)$*. So* $S_1 \# S_2 := \{(S_1 - D_1) \cup (S_2 - D_2)\}/\sim$*.*

Theorem 1 (Classification for Compact Orientable Surfaces)**.** *Any closed connected orientable surface is homeomorphic to either a sphere or a finite connected sum of tori,*

$$S = \mathbb{S}^2 \# T_1 \# T_2 \cdots \# T_g,$$

where $\mathbb{S}^2$ *is the unit sphere,* T_i *is a torus,* $i = 1, 2, \cdots, g$*.* g *is called the genus of the surface, and each* T_i *is a handle.*

In general, the genus g and the number of boundary components b are the total topological invariants. Surface topology is usually represented by its fundamental group.

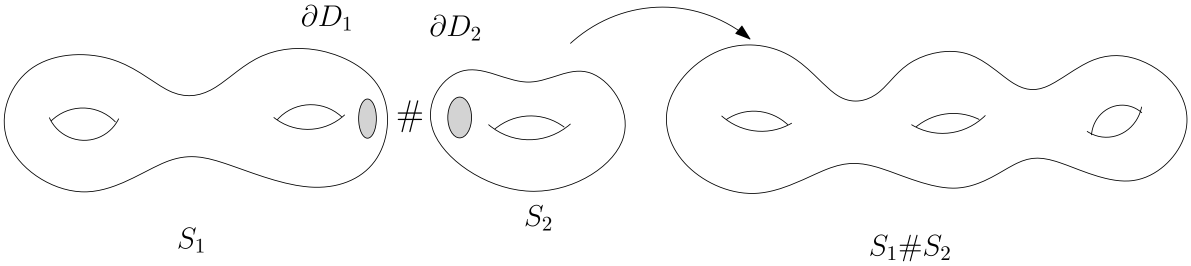

Figure 2.1: Connected sum.

2.1.1 Fundamental Group

Definition 3 (Homotopy)**.** *Two continuous maps* $f_0, f_1 : M \to N$ *are said to be* homotopic *if there is a continuous map* $F : M \times [0,1] \to N$ *such that* $F(\cdot,0) = f_0$ *and* $F(\cdot,1) = f_1$. *The map F is called a* homotopy *between* f_0 *and* f_1, *denoted as* $f_0 \cong f_1$ *or* $F : f_0 \cong f_1$. *For each* $t \in [0,1]$, *we denote* $F(\cdot,t)$ *by* $f_t : M \to N$, *where* f_t *is a continuous map.*

A map $f : [0,1] \to M$ from the unit interval to a topological space M is called a *path* in M. If f and g are two paths in M with $f(1) = g(0)$ then the *product* of f and g is a path $f \cdot g$, which is defined as

$$f \cdot g(t) = \begin{cases} f(2t) & 0 \le t \le \frac{1}{2} \\ g(2t-1) & \frac{1}{2} \le t \le 1. \end{cases} \tag{2.1.1}$$

Fix a base point $q \in M$, a *loop* with base point q is a path such that $f(0) = f(1) = q$. Two loops on a surface are homotopic to each other, if they can deform to each other without leaving the surface, as shown in Fig. 2.2.

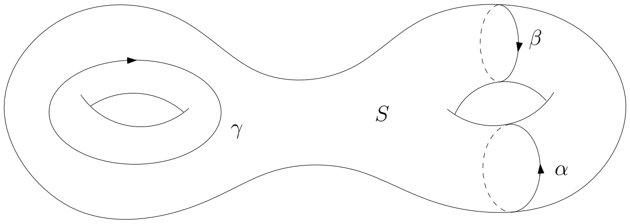

Figure 2.2: α is homotopic to β, not homotopic to γ

Definition 4 (Fundamental Group)**.** *All the homotopy classes of loops with base point q under the product (2.1.1) form a group, the so called* fundamental group *of the surface, denoted as* $\pi_1(M,q)$.

The fundamental group is finitely generated. Intuitively, each handle T_i is a torus, which is the direct product of two circles, $T_i = \mathbb{S}^1 \times \mathbb{S}^1$. We denote the first circle as a_i, and the second circle b_i, then all such $\{(a_i,b_i)\}$'s are the generators of $\pi_1(M,q)$.

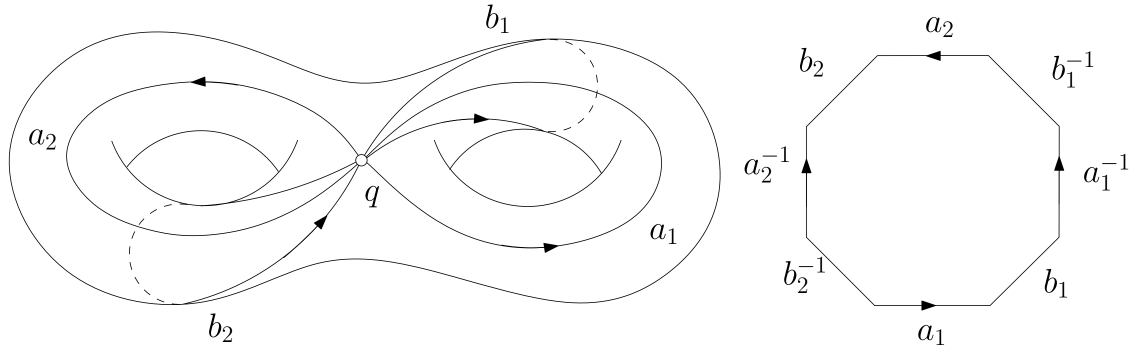

Figure 2.3: A set of canonical basis of the fundamental group $\pi_1(M,q)$

Definition 5 (Canonical fundamental group basis)**.** *A fundamental group basis* $\{a_1, b_1, a_2, b_2, \cdots, a_g, b_g\}$ *is canonical, if*

1. a_i *and* b_i *intersect at the same point* q*.*
2. a_i *and* a_j*,* b_i *and* b_j*,* a_i *and* b_j *only touch at* q*,* $i \neq j$*.*

As shown in Figure 2.3, if we slice the surface along the canonical fundamental group generators, we will get a $4g$-gon. The boundary is $a_1 b_1 a_1^{-1} b_1^{-1} \cdots a_g b_g a_g^{-1} b_g^{-1}$, which can shrink to a point. For general compact orientable closed surfaces, the following theorem holds:

Theorem 2 (Fundamental Groups of General Surfaces)**.** *The fundamental group of the surface* $M = S^2 \# g T^2$ *is the group with generators* $\{a_1, b_1, a_2, b_2, \cdots, a_g, b_g\}$ *and one relation* $\prod_{k=1}^{g} [a_k, b_k] = e$*, where* $[a,b] = aba^{-1}b^{-1}$*.*

2.1.2 Covering Spaces

Definition 6 (Covering Space)**.** *Let* $p : \tilde{M} \to M$ *be a continuous map and* p *is onto. Suppose for all* $q \in M$*, there is an open neighborhood* U *of* q *such that*

$$p^{-1}(U) = \cup_{j \in J} \tilde{U}_j,$$

for some collection $\{\tilde{U}_j, j \in J\}$ *of subsets of* $\tilde{M}$ *satisfying* $\tilde{U}_j \cap \tilde{U}_k = \emptyset$ *if* $j \neq k$*, and with* $p|_{\tilde{U}_j} : \tilde{U}_j \to U$ *a homeomorphism for each* $j \in J$*. Then* $p : \tilde{M} \to M$ *is a* covering.

The automorphisms of the covering space which are commutative with the projection are called deck transformations.

Definition 7 (Deck Transformation)**.** *Suppose* $p : \tilde{M} \to M$ *is a covering. An automorphism* $\tau : \tilde{M} \to \tilde{M}$ *is called a* deck transformation *if* $p \circ \tau = p$*.*

All the deck transformations form a group *Deck*$(\tilde{M})$, the *deck transformation group*. M is homeomorphic to the quotient space

$$\tilde{M}/Deck(\tilde{M}) \cong M.$$

Definition 8 (Fundamental Domain)**.** *A closed subset* $D \in \tilde{M}$ *is called a* fundamental domain *of the* $Deck(\tilde{M})$*, if*

$$\tilde{M} = \bigcup_{\tau \in Deck} \tau D,$$

$\tilde{M}$ is the union of conjugates of D, and the intersection of any two conjugates has no interior.

Among all covering spaces for a given surface, the one with the simplest topology is the so called universal covering.

Definition 9 (Universal Covering)**.** *Suppose* $p : \tilde{M} \to M$ *is a covering. If* $\tilde{M}$ *is simply connected* ($\pi(\tilde{M}, \tilde{q}) = \langle e \rangle$)*, then the covering is the* universal covering.

Theorem 3 (Universal Covering Space for Surfaces)**.** *The universal covering spaces of orientable closed surfaces are sphere* $\mathbb{S}^2$ *(genus zero), plane* $\mathbb{E}^2$ *(genus one) and disk* $\mathbb{H}^2$ *(high genus).*

2.2 Surface Differential Geometry

We will briefly review the fundamental concepts and theorems for surface differential geometry using movable frame method, due to its simplicity.

Movable Frame Method

We apply movable frame method to study surfaces in $\mathbb{E}^3$. Assume the equation for a surface S is $\mathbf{r} = \mathbf{r}(u,v)$. Select a frame field locally, at each point $\mathbf{r}(u,v)$ define an orthonormal frame

$$\{\mathbf{r}(u,v); \mathbf{e}_1(u,v), \mathbf{e}_2(u,v), \mathbf{e}_3(u,v)\},$$

such that $\mathbf{e}_3$ is the normal field, $\mathbf{e}_3(u,v) = \mathbf{n}(u,v)$. Take the exterior derivative of the movable frame $\{\mathbf{r}; \mathbf{e}_1, \mathbf{e}_2, \mathbf{e}_3\}$. We get the surface structure equation

$$d\mathbf{r} = \omega_1 \mathbf{e}_1 + \omega_2 \mathbf{e}_2,$$

$$d \begin{pmatrix} \mathbf{e}_1 \\ \mathbf{e}_2 \\ \mathbf{e}_3 \end{pmatrix} = \begin{pmatrix} 0 & \omega_{12} & \omega_{13} \\ -\omega_{12} & 0 & \omega_{23} \\ -\omega_{13} & -\omega_{23} & 0 \end{pmatrix} \begin{pmatrix} \mathbf{e}_1 \\ \mathbf{e}_2 \\ \mathbf{e}_3 \end{pmatrix}.$$

By direct computation, we obtain

$$\omega_{12} = \frac{d\omega_1}{\omega_1 \wedge \omega_2}\omega_1 + \frac{d\omega_2}{\omega_1 \wedge \omega_2}\omega_2. \tag{2.2.1}$$

From $d^2\mathbf{e}_1 = 0$, we can get the *Gauss equation*

$$d\omega_{12} = \omega_{13} \wedge \omega_{32} \tag{2.2.2}$$

and *Codazzi equation*

$$d\omega_{13} = \omega_{12} \wedge \omega_{23}. \tag{2.2.3}$$

Similarly, from $d^2\mathbf{e}_2 = 0$ we obtain another Codazzi equation

$$d\omega_{23} = \omega_{21} \wedge \omega_{13}. \tag{2.2.4}$$

First and Second Fundamental Forms

The first fundamental form of the surface is given by

$$I = \langle d\mathbf{r}, d\mathbf{r} \rangle = \langle \omega_1 \mathbf{e}_1 + \omega_2 \mathbf{e}_2, \omega_1 \mathbf{e}_1 + \omega_2 \mathbf{e}_2 \rangle = (\omega_1)^2 + (\omega_2)^2.$$

The second fundamental form is given by

$$II = -\langle d\mathbf{r}, d\mathbf{e}_3 \rangle = -\langle \omega_1 \mathbf{e}_1 + \omega_2 \mathbf{e}_2, \omega_{31} \mathbf{e}_1 + \omega_{32} \mathbf{e}_2 \rangle = \omega_1 \omega_{13} + \omega_2 \omega_{23}.$$

The fundamental theorem for surface differential geometry is as follows.

Theorem 4. *A surface embedded in $\mathbb{E}^3$ is determined by its first fundamental form and second fundamental from unique up to a rigid motion, the first fundamental form and the second fundamental form satisfy the Gauss equation and Codazzi equations.*

The proof can be found in classical differential geometry textbook, such as [21].

Because $d\mathbf{r} = \omega_1 \mathbf{e}_1 + \omega_2 \mathbf{e}_2$, the area element of the surface is $\omega_1 \wedge \omega_2$. Similarly, $d\mathbf{e}_3 = \omega_{31} \mathbf{e}_1 + \omega_{32} \mathbf{e}_2$, the area element of the unit sphere is $\omega_{31} \wedge \omega_{32}$, then the determinant of the Jacobian matrix of the Weingarten map $d\mathbf{r} \to d\mathbf{e}_3$ is given by

$$K = \frac{\omega_{31} \wedge \omega_{32}}{\omega_1 \wedge \omega_2}$$

From Gauss equation (2.2.2), we get the important equation for Gauss curvature

$$d\omega_{12} = -\omega_{31} \wedge \omega_{32} = -K \omega_1 \wedge \omega_2. \tag{2.2.5}$$

We say a geometric quantity is intrinsic, if it is solely determined by the first fundamental form, namely Riemannian metric. From (2.2.1) and (2.2.5), we see that Gauss curvature K is solely determined by ω_1 and ω_2, therefore

Theorem 5. *Gauss curvature is intrinsic.*

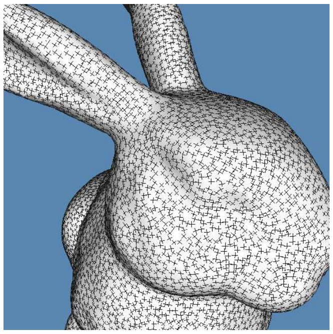

Figure 2.4: Principle directions on the Stanford bunny

Curves on Surfaces

Consider a curve C on a surface S with a local representation $C : (u(s), v(s))$, where s is the arc length parameter. Let α be the tangent direction of C, $\theta(s)$ is the angle from $\mathbf{e}_1$ to α. By direct computation, the *geodesic curvature* is given by

$$k_g = \frac{d\theta + \omega_{12}}{ds}. \tag{2.2.6}$$

If $k_g \equiv 0$, then the curve is called a *geodesic*. The *normal curvature* is

$$k_n = \frac{\omega_1\omega_{13} + \omega_2\omega_{23}}{ds^2} = \frac{II}{I}.$$

At each point, there are two orthogonal tangent directions along which the normal curvature reaches the minimum k_1 and maximum k_2. k_1 and k_2 are called the *principle curvatures* and the two directions are called the *principle directions*. The Gauss curvature is the product of principle curvatures, $K = k_1k_2$; the *mean curvature* is the mean value of the principle curvatures, $H = (k_1 + k_2)/2$.

From (2.2.5) and (2.2.6), we can prove the Gauss-Bonnet theorem, which claims that although the Gauss curvature is determined by the Riemannian metric, the total curvature is solely determined by the surface topology.

Theorem 6 (Gauss-Bonnet). *Suppose S is a surface with/without boundaries. Then*

$$\int_S KdA + \int_{\partial S} k_g ds = 2\pi\chi(S),$$

where $\chi(S)$ is the Euler characteristics of the surface.

2.3 Conformal Metric Deformation

2.3.1 Isothermal Coordinates

Given a metric surface, one can choose *isothermal coordinates* to facilitate geometric computations. Most differential operators, such as gradient, Laplace-Beltrami operators have the simplest form under isothermal coordinates.

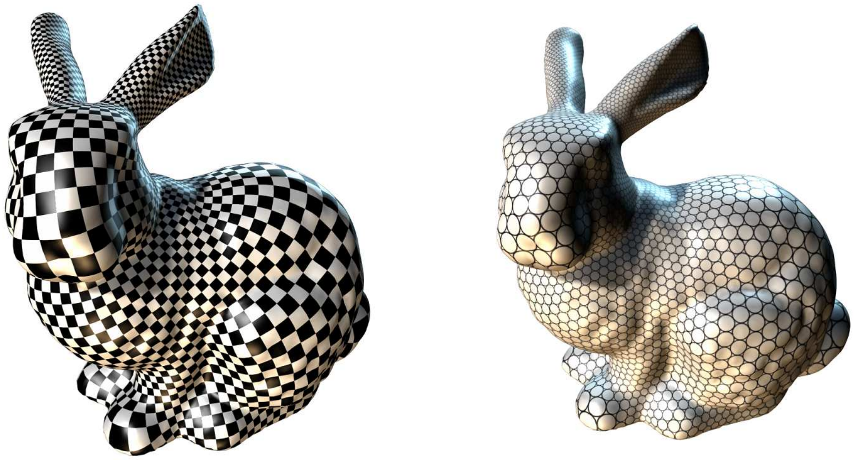

Figure 2.5: Isothermal coordinate system on the Stanford bunny surface.
The mapping from the surface to the parameter plane is conformal, which preserves angles and infinitesimal circles

Definition 10 (Isothermal Coordinates)**.** *On a surface S with a Riemannian metric* $\mathbf{g}$*, a local coordinates system* (u,v) *is an isothermal coordinate system, if*

$$\mathbf{g}(u,v) = e^{2\lambda(u,v)}(du^2+dv^2), \tag{2.3.1}$$

where $\lambda : S \to \mathbb{R}$ *is a function defined on the surface, and called conformal factor.*

Isothermal coordinates on metric surfaces always exist, which can be proven either using surface Ricci flow or quasi-conformal mapping. In the later part, we give a proof by solving a Beltrami equation. An elementary proof can be found in Chern's work [12].

Theorem 7 (Existence of Isothermal Coordinates)**.** *Let* $(S,\mathbf{g})$ *be a compact orientable surface, then every point of S has a neighborhood whose local coordinates are isothermal parameters.*

2.3.2 Gauss Curvature under Conformal Deformation

We use movable frame method to deduce Gauss curvature under isothermal coordinates. Let $(S,\mathbf{g})$ be a surface embedded in $\mathbb{E}^3$, with position vector function $\mathbf{r}(u,v)$ and isothermal coordinates (u,v). Then

$$\langle \mathbf{r}_u, \mathbf{r}_u\rangle = e^{2\lambda}, \langle \mathbf{r}_v, \mathbf{r}_v\rangle = e^{2\lambda}, \langle \mathbf{r}_u, \mathbf{r}_v\rangle = 0,$$

choose orthonormal frames

$$\mathbf{e}_1 = e^{-\lambda}\mathbf{r}_u, \mathbf{e}_2 = e^{-\lambda}\mathbf{r}_v, \mathbf{e}_3 = \mathbf{n}.$$

Then

$$d\mathbf{r} = \mathbf{r}_u du + \mathbf{r}_v dv = \mathbf{e}_1 e^{\lambda} du + \mathbf{e}_2 e^{\lambda} dv = \omega_1 \mathbf{e}_1 + \omega_2 \mathbf{e}_2,$$

where $\omega_1 = e^{\lambda} du$ and $\omega_2 = e^{\lambda} dv$. From (2.2.1), we get $\omega_{12} = -\lambda_v du + \lambda_u dv$. Therefore

$$d\omega_{12} = (\lambda_{vv} + \lambda_{uu}) du \wedge dv = -K\omega_1 \wedge \omega_2 = -Ke^{2\lambda} du \wedge dv,$$

we obtain

$$K(u,v) = -e^{-2\lambda(u,v)}(\frac{\partial^2}{\partial u^2} + \frac{\partial^2}{\partial v^2})\lambda = -\Delta_{\mathbf{g}}\lambda, \tag{2.3.2}$$

where the Laplace-Beltrami operator is

$$\Delta_{\mathbf{g}} = e^{-2\lambda(u,v)}(\frac{\partial^2}{\partial u^2} + \frac{\partial^2}{\partial v^2}).$$

Let $\bar{\mathbf{g}}$ be another Riemannian metric, conformal to the original metric

$$\bar{\mathbf{g}} = e^{2\tau}\mathbf{g}.$$

We choose isothermal coordinates for both $\mathbf{g}$ and $\bar{\mathbf{g}}$, then

$$\mathbf{g} = e^{2\lambda}(du^2 + dv^2), \bar{\mathbf{g}} = e^{2(\lambda+\tau)}(du^2 + dv^2),$$

The Gauss curvature $\bar{K}$ induced by $\bar{\mathbf{g}}$ becomes

$$\bar{K} = -e^{-2(\lambda+\tau)}\Delta(\lambda + \tau) = e^{-2\tau}(-e^{-2\lambda}\Delta\lambda - e^{-2\lambda}\Delta\tau) = e^{-2\tau}(K - \Delta_{\mathbf{g}}\tau).$$

So we obtain the Yamabe equation

$$\bar{K} = e^{-2\tau}(K - \Delta_{\mathbf{g}}\tau). \tag{2.3.3}$$

2.3.3 Geodesic Curvature under Conformal Deformation

Suppose C is a curve on the surface and the tangent direction α of the curve has the angle θ to the $\mathbf{e}_1$ direction. Then the geodesic curvature of C is

$$k_g = \frac{d\theta + \omega_{12}}{ds}.$$

Choose the isothermal coordinates, $\omega_{12} = \lambda_v du - \lambda_u dv$, $ds = e^{\lambda}\sqrt{du^2 + dv^2}$

$$\frac{du}{ds} = e^{-\lambda}\cos\theta, \frac{dv}{ds} = e^{-\lambda}\sin\theta,$$

$$k_g = \frac{d\theta}{ds} + \frac{\lambda_v du - \lambda_u dv}{ds} = \frac{d\theta}{ds} - e^{-\lambda}(\lambda_u \sin\theta - \lambda_v \cos\theta) = \frac{d\theta}{ds} - \langle\nabla_{\mathbf{g}}\lambda, \mathbf{n}\rangle,$$

where $\nabla_{\mathbf{g}} = e^{-\lambda}(\frac{\partial}{\partial u}, \frac{\partial}{\partial v})$, $\mathbf{n} = (\sin\theta, -\cos\theta)$ is the outward normal of the curve on the tangent plane. The geodesic curvature can also be written as:

$$k_g = \frac{d\theta}{ds} - \partial_{\mathbf{n},\mathbf{g}}\lambda,$$

Assume $\bar{\mathbf{g}}$ is another Riemannian metric, conformal to $\mathbf{g}$, $\bar{\mathbf{g}} = e^{2\tau}\mathbf{g}$, choose the isothermal coordinates (u,v),

$$\bar{\mathbf{g}} = e^{2(\tau+\lambda)}(du^2+dv^2), \mathbf{g} = e^{2\lambda}(du^2+dv^2),$$

Then

$$\bar{k}_g = \frac{d\theta}{d\bar{s}} - \partial_{\mathbf{n},\bar{\mathbf{g}}}(\lambda+\tau)$$

because $d\bar{s} = e^{\tau}ds$,

$$\frac{d\theta}{d\bar{s}} = e^{-\tau}\frac{d\theta}{ds}.$$

Because $\nabla_{\bar{\mathbf{g}}} = e^{-\tau-\lambda}(\frac{\partial}{\partial u}, \frac{\partial}{\partial v}) = e^{-\tau}\nabla_{\mathbf{g}}$,

$$\partial_{\mathbf{n},\bar{\mathbf{g}}} = \langle \nabla_{\bar{\mathbf{g}}}, \mathbf{n} \rangle = e^{-\tau}\langle \nabla_{\mathbf{g}}, \mathbf{n} \rangle = e^{-\tau}\partial_{\mathbf{n},\mathbf{g}}.$$

Therefore

$$\bar{k}_g = e^{-\tau}\frac{d\theta}{ds} - e^{-\tau}\partial_{\mathbf{n},\mathbf{g}}(\lambda+\tau) = e^{-\tau}(\frac{d\theta}{ds} - \partial_{\mathbf{n},\mathbf{g}}\lambda - \partial_{\mathbf{n},\mathbf{g}}\tau) = e^{-\tau}(k_g - \partial_{\mathbf{n},\mathbf{g}}\tau).$$

Theorem 8 (Yamabe Equation)**.** *Suppose S is a surface with a Riemannian metric $\mathbf{g}$, which induces Gauss curvature K and geodesic curvature k_g on the boundary. Let*

$$\bar{\mathbf{g}} = e^{2\lambda}\mathbf{g}$$

be another metric conformal to the original one, which induces Gaussian curvature $\bar{K}$ and geodesic curvature $\bar{k}_g$. Then the Yamabe equations are

$$\begin{array}{rcl} \bar{K} & = & e^{-2\lambda}(K - \Delta_{\mathbf{g}}\lambda), \\ \bar{k}_g & = & e^{-\lambda}(k_g - \partial_{\mathbf{n},\mathbf{g}}\lambda). \end{array}$$

Yamabe equations can be solved using surface Ricci flow.

2.4 Surface Ricci Flow

Given an n dimensional Riemannian manifold M with metric tensor $\mathbf{g} = (g_{ij})$, the normalized Ricci flow is defined by the geometric evolution equation

$$\partial_t \mathbf{g}(t) = -2Ric(\mathbf{g}(t)) + \rho\mathbf{g}(t). \tag{2.4.1}$$

where R_{ij} is the Ricci curvature tensor and ρ is the mean value of the scalar curvature

$$\rho = \frac{2}{n}\frac{\int_M R_{\mathbf{g}} d\mu_{\mathbf{g}}}{\int_M d\mu_{\mathbf{g}}},$$

where R_g and μ_g are the scalar curvature and the volume element with respect to the evolving metric $\mathbf{g}(t)$. Recall that a one-parameter family of metrics $\{\mathbf{g}(t)\}$, where $t \in [0,T)$ for some $0 < T \leq \infty$, is called a solution to the normalized Ricci flow if it satisfies the above equation at all $p \in M$ and $t \in [0,T)$.

In two dimensions, the Ricci curvature for a metric $\mathbf{g}$ is equal to $\frac{1}{2}R\mathbf{g}$, where R is the scalar curvature (or twice the Gauss curvature). Therefore, the normalized Ricci flow equation for surfaces takes the form

$$\partial_t \mathbf{g}(t) = (\rho - R(t))\mathbf{g}(t), \tag{2.4.2}$$

where ρ is the mean value of the scalar curvature,

$$\rho = \frac{4\pi\chi(M)}{A(0)}.$$

$A(0)$ is the total area of the surface M at time $t = 0$.

Let $(g^{ij}) = (g_{ij})^{-1}$ be the inverse of the matrix (g_{ij}). Set the area element with respect to metric $\mathbf{g}$ to be

$$\mu_{\mathbf{g}} = \sqrt{det g_{ij}}.$$

Then along the Ricci flow, we compute

$$\partial_t \mu_{\mathbf{g}} = \frac{1}{2} g^{ij} \partial_t g_{ij} \mu_{\mathbf{g}} = (\rho - R)\mu_{\mathbf{g}}.$$

For the total area $A = \int_M d\mu$, we have

$$\partial_t A(t) = \int_M (\rho - R) d\mu_{\mathbf{g}} = 0.$$

Therefore, the normalized Ricci flow preserves the total area, $A(t) = A(0), \forall t > 0$. During the Ricci flow (2.4.2), the metric deforms conformally, $\mathbf{g}(t) = e^{2\lambda(t)}\mathbf{g}(0)$,

$$\partial_t \lambda = \frac{1}{2}(\rho - R), \lambda(0) = 0, \tag{2.4.3}$$

and from Yamabe equation (2.3.3)

$$\Delta_0 \lambda - \frac{1}{2}R_0 + \frac{1}{2}Re^{2\lambda} = \Delta_0 \lambda - K_0 + Ke^{2\lambda} = 0.$$

We obtain the curvature evolution equation

$$\partial_t R = \Delta_{g(t)} R + R(R - \rho). \tag{2.4.4}$$

Let $u = e^{2\lambda}$, then we get the evolution equation for u,

$$\partial_t u = (\rho - R)u.$$

Plug in $R = u^{-1}(R_0 - \Delta_0 \log u)$, we get an evolution flow for u,

$$\partial_t u = \Delta_0 \log u + \rho u - R_0, u(0) = u_0. \tag{2.4.5}$$

For most evolution equations, one proves that solutions exist for all $t \geq 0$ by combining a short-time existence (and uniqueness) result with a prior bounds which show that solutions cannot develop singularities in finite time. Equation (2.4.5) is a parabolic equation. It can be set up as a fixed point problem for a contraction mapping. The mapping is obtained by applying the fundamental solution of the linearization at any given $u_0 > 0$ to (2.4.5); it is a contraction on any sufficiently short time interval. This gives the proof for the short-time existence of the solution. The long-time existence can be obtained by estimating both the lower and upper bounds of $R(t)$ and $u(t)$, which requires a generalization of Li-Yau's Harnack inequality [47]. The proofs require advanced background knowledge and sophisticated geometric skills, which is beyond the scope of the current book. Details can be found in Hamilton's [35] and chow's [13] works.

Theorem 9 (Hamilton [35])**.** *Let (M^2, g_0) be compact. If $\rho \leq 0$, or if $R(0) \geq 0$ on all of M^2, then the solution to (2.4.2) exists for all $t \geq 0$ and converges to a metric of constant curvature.*

Theorem 10 (Chow [13])**.** *If g_0 is any metric on S^2, then its evolution under (2.4.2) develops positive scalar curvature in finite time, and hence by Theorem 9 converges to the round metric as t goes to ∞.*

Chapter 3

Groundwork: Discrete Surface Ricci Flow

This chapter systematically introduces the discrete surface Ricci flow theory. The whole theory is explained using the variational principle on discrete surfaces based on derivative cosine law [53].

Ricci flow conformally deforms the Riemannian metrics, such that during the flow the infinitesimal circles are preserved. This phenomenon inspired Thurston to develop the circle packing method. In his work on constructing hyperbolic metrics on 3-manifolds, Thurston [70] studies a Euclidean (or a hyperbolic) circle packing on a triangulated closed surface with prescribed intersection angles. Thurston's work generalizes AndreevŠs and Koebe's results of circle packing on a sphere [5, 6, 45]. Thurston conjectured that the discrete conformal mapping based on circle packing converges to the smooth Riemann mapping when the discrete tessellation becomes finer and finer. Thurston's conjecture has been proven by Rodin and Sullivan [65]. Chow and Luo established the intrinsic connection between circle packing and surface Ricci flow [15].

3.1 Discrete Surface

In practice, smooth surfaces are usually approximated by discrete surfaces, namely, triangular meshes. Figure 3.2 demonstrates such an example. The surface of the sculpture of Michelangelo's David is approximated by a triangular mesh, each face of the mesh is a Euclidean triangle. With high sampling density, the discrete surface can approximate the smooth surface accurately.

The combinatorial structure of a discrete surface is represented by a simplicial complex. The fundamental concepts from smooth differential geometry, such as Riemannian metric, curvature and conformal structure, are generalized to the simplicial complex, respectively.

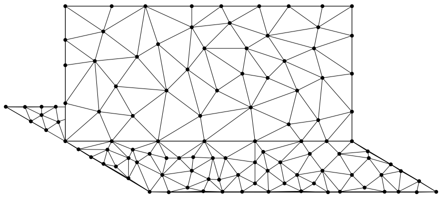

Figure 3.1: A non-manifold simplicial complex

3.1.1 Simplicial Complex

Definition 11 (Simplex)**.** *Suppose $n+1$ points $\{v_0, v_1, \cdots, v_n\}$ in the general positions in $\mathbb{R}^n$. The standard simplex $[v_0, v_1, \cdots, v_n]$ is the minimal convex set including all*

$$\sigma = [v_0, v_1, \cdots, v_n] := \{\sum_{i=0}^{n} \lambda_i v_i | \sum_{i=0}^{n} \lambda_i = 1, \lambda_i \geq 0\}.$$

We call $v_0, v_1, \cdots, v_n$ the vertices of the simplex σ.

Definition 12 (Facet)**.** *Suppose σ is a simplex, $\tau \subset \sigma$ is also a simplex. Then we say τ is a facet of σ.*

The simplex has an orientation. Suppose $(i_1, i_2, \cdots, i_n)$ is a permutation of $(1, 2, \cdots, n)$. $[v_{i_1}, v_{i_2}, \cdots, v_{i_n}]$ has the same orientation with $[v_1, v_2, \cdots, v_n]$, if the permutation is the product of even number of swaps. Otherwise, they have opposite orientations, if the permutation can be decomposed to odd number of swaps.

Definition 13 (Boundary Operator)**.** *The boundary of a simplex σ is*

$$\partial\sigma = \sum_{i=0}^{n} (-1)^j [v_0, \cdots, v_{j-1}, v_{j+1}, \cdots, v_n].$$

The combinatorial structure of a discrete surface is usually represented as a simplicial complex

Definition 14 (Simplicial Complex)**.** *A simplicial complex Σ is a union of simplicies, such that*

1. *If a simplex σ belongs to Σ, then all its facets also belongs to Σ.*
2. *If two simplicies $\sigma_1, \sigma_2 \subset \Sigma$, $\sigma_1 \cap \sigma_2 \neq \emptyset$, then their intersection is a common facet.*

A simplicial complex may not necessarily to be a manifold. Figure 3.1 gives a counter example, where three half planes meet together at their boundaries.

In practice, smooth surfaces are usually approximated by *discrete surfaces*. Discrete surfaces are represented as two dimensional simplicial complexes which are manifolds, as shown in Fig. 3.2.

Definition 15 (Triangular Mesh)**.** *Suppose Σ is a two dimensional simplicial complex, furthermore it is also a manifold, namely, for each point p of Σ, there exists a neighborhood of p, $U(p)$, which is homeomorphic to the whole plane or the upper half plane. Then Σ is called a triangular mesh.*

If $U(p)$ is homeomorphic to the whole plane, then p is called an interior point; if $U(p)$ is homeomorphic to the upper half plane, then p is called a boundary point.

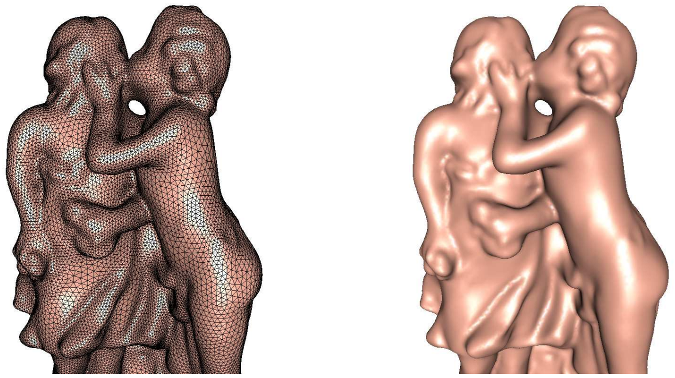

Figure 3.2: Smooth surfaces are approximated by discrete Surfaces

3.1.2 Discrete Riemannian Metric and Curvature

The fundamental concepts from smooth differential geometry, such as Riemannian metric, curvature and conformal structure, are generalized to the simplicial complex, respectively.

In the following discussion, we use $\Sigma = (V,E,F)$ to denote the mesh with vertex set V, edge set E and face set F. A discrete surface is with Euclidean (hyperbolic or spherical) background geometry if it is constructed by isometrically gluing triangles in $\mathbb{E}^2$ ($\mathbb{H}^2$ or $\mathbb{S}^2$).

Definition 16 (Discrete Riemannian Metric). *A discrete metric on a triangular mesh is a function defined on the edges, $l : E \to \mathbb{R}^+$, which satisfies the triangle inequality: on each face $[v_i, v_j, v_k]$, l_i, l_j, l_k are the lengths of edges against v_i, v_j, v_k respectively,*

$$l_i + l_j > l_k,\ l_j + l_k > l_i,\ l_k + l_i > l_j.$$

A triangular mesh with a discrete Riemannian metric is called a discrete metric surface.

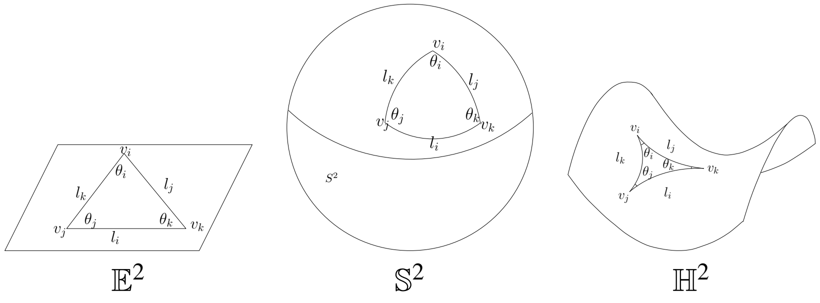

Figure 3.3: Different background geometry, Euclidean, spherical and hyperbolic.

Definition 17 (Background Geometry). *Suppose Σ is a discrete metric surface, if each face of Σ is a spherical, (Euclidean or hyperbolic) triangle, then we say Σ is with spherical, (Euclidean or hyperbolic) background geometry. We use $\mathbb{S}^2$, $\mathbb{E}^2$ and $\mathbb{H}^2$ to represent spherical Euclidean or hyperbolic background metric.*

Triangles with different background geometries satisify different cosine laws:

$$\begin{array}{rcll} 1 & = & \frac{\cos\theta_i+\cos\theta_j\cos\theta_k}{\sin\theta_j\sin\theta_k} & \mathbb{E}^2 \\ \cos l_i & = & \frac{\cos\theta_i+\cos\theta_j\cos\theta_k}{\sin\theta_j\sin\theta_k} & \mathbb{S}^2 \\ \cosh l_i & = & \frac{\cosh\theta_i+\cosh\theta_j\cosh\theta_k}{\sinh\theta_j\sinh\theta_k} & \mathbb{H}^2 \end{array}$$

3.1.3 Discrete Gauss-Bonnet Theorem

The discrete Gaussian curvature is defined as angle deficit, as shown in Fig. 3.4.

Definition 18 (Discrete Gauss Curvature)**.** *The discrete Gauss curvature function on a mesh is defined on vertices, $K : V \to \mathbb{R}$,*

$$K(v) = \begin{cases} 2\pi - \sum_{jk}\theta_i^{jk}, & v \notin \partial M \\ \pi - \sum_{jk}\theta_i^{jk}, & v \in \partial M \end{cases},$$

where θ_i^{jk}'s are corner angle at v_i in the face $[v_i, v_j, v_k]$, and ∂M represents the boundary of the mesh.

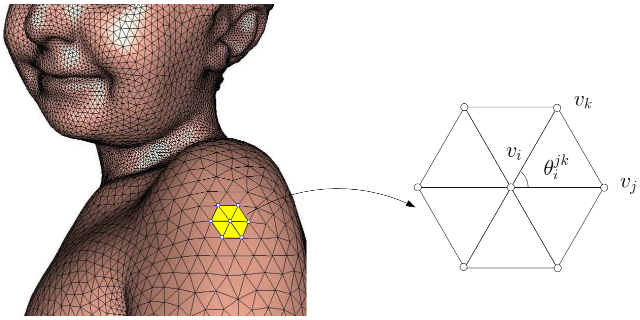

Figure 3.4: Discrete curvatures of an interior vertex

The Gauss-Bonnet theorem still holds in the discrete case.

Theorem 11 (Discrete Gauss-Bonnet Theorem)**.** *Suppose Σ is a triangular mesh with Euclidean background metric. The total curvature is a topological invariant,*

$$\sum_{v\notin\partial\Sigma} K(v) + \sum_{v\in\partial\Sigma} K(v) + \varepsilon A(\Sigma) = 2\pi\chi(\Sigma), \tag{3.1.1}$$

where χ is the characteristic Euler number, and K is the Gauss curvature, $A(\Sigma)$ is the total area, $\varepsilon = \{+1, 0, -1\}$ if Σ is with spherical, Euclidean or hyperbolic background geometry.

In the following, we give an elementary proof based on double covering technique.

Proof. First, we assume the mesh Σ is closed without boundary components. V,E,F represent the number of vertices, edges and faces. Then each face has 3 edges, each edge is shared by 2 faces, therefore $3F = 2E$. The Euler characteristic number is $\chi(\Sigma) = V + F - E = V - \frac{F}{2}$. Let v_i be a vertex, the corner angle at v_i in face $[v_i, v_j, v_k]$ is α_i^{jk}, then the Gauss curvature of v_i is

$$K(v_i) = 2\pi - \sum_{jk} \alpha_i^{jk}.$$

The total Gauss curvature is

$$\sum_i K(v_i) = \sum_i (2\pi - \sum_{jk} \alpha_i^{jk}) = 2\pi V - \sum_{ijk} (\alpha_i^{jk} + \alpha_j^{ki} + \alpha_k^{ij}) = 2\pi V - \pi F = 2\pi(V - \frac{F}{2}).$$

Second, we prove the theorem for meshes with boundary components. Suppose Σ has boundaries. We construct a duplicate mesh Σ', each vertex $v_i \in \Sigma$ has a corresponding vertex $v_i' \in \Sigma'$, each face $[v_i, v_j, v_k]$ has a corresponding face $[v_i', v_j', v_k']$. Then we reverse the orientation of all faces in Σ', namely, we change the order of the face vertices from $[v_i', v_j', v_k']$ to $[v_j', v_i', v_k']$. Then we identify each boundary vertex $v_i \in \partial\Sigma$ with the corresponding vertex $v_i' \in \partial\Sigma'$, this gives a equivalence relation $v_i \sim v_i'$. The doubled mesh $\bar{\Sigma}$ is given by the quotient space

$$\bar{\Sigma} := \Sigma \cup \Sigma' / \sim .$$

Suppose $v_i \in \Sigma$ is an interior vertex in Σ. Then it is included in $\bar{\Sigma}$, the Gauss curvature of v_i in Σ is same as that in $\bar{\Sigma}$,

$$K_\Sigma(v_i) = K_{\bar{\Sigma}}(v_i), v_i \notin \partial\Sigma.$$

If $v_i \in \partial\Sigma$ is a boundary vertex in Σ, then by the definition (18) of discrete geodesic and Gauss curvatures, the Gauss curvature of v_i in $\bar{\Sigma}$ doubles its geodesic curvature in Σ,

$$2K_\Sigma(v_i) = K_{\bar{\Sigma}}(v_i).$$

Therefore the total curvature of $\bar{\Sigma}$ doubles the total curvature of Σ.

On the other hand, let E_0 represent the number of interior edges in Σ, E_1 boundary edges; V_0 the interior vertices, V_1 boundary vertices. Then it is obvious that $V_1 = E_1$, the Euler characteristic number of $\bar{\Sigma}$ is given by

$$\chi(\bar{\Sigma}) = 2V_0 + V_1 + 2F - (2E_0 + E_1) = 2(V_0 + V_1) + 2F - 2(E_0 + E_1) = 2\chi(\Sigma),$$

therefore,

$$2\sum_{v\in\Sigma} K_\Sigma(v) = \sum_{v\in\bar{\Sigma}} K_{\bar{\Sigma}}(v) = 2\pi\chi(\bar{\Sigma}) = 4\pi\chi(\Sigma),$$

theorem holds for discrete surfaces with boundaries. □

3.2 Discrete Euclidean Surface Ricci Flow

Discrete surface Ricci flow can be interpreted in a variational framework. Ricci flow is the negative gradient flow of a convex energy. The convexity of the energy induces the one-to-one correspondence between the curvature functions and the conformal metrics.

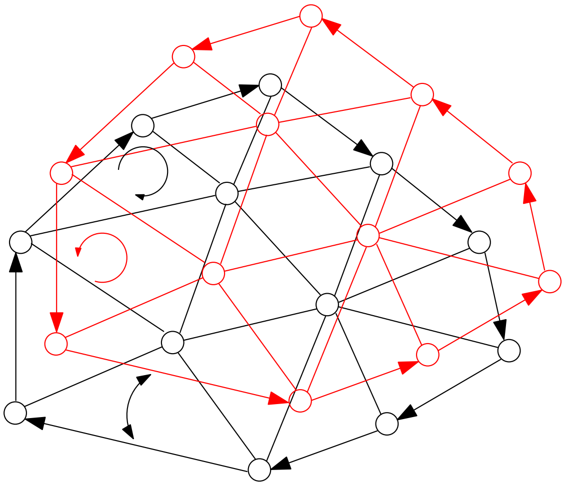

Figure 3.5: Double covering

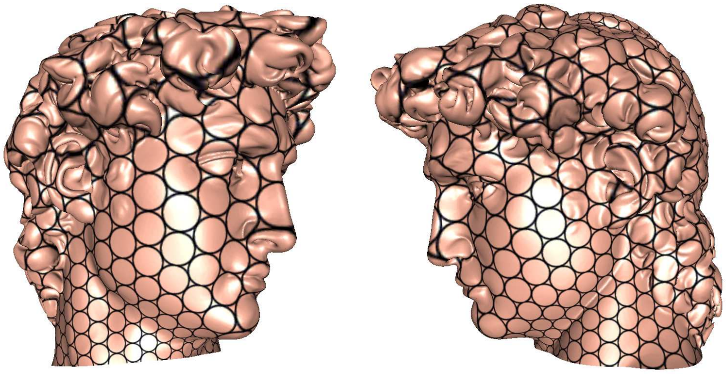

Figure 3.6: Conformal mapping preserves infinitesimal circles.

3.2.1 Discrete Conformal Metric Deformation

Surface Ricci flow conformally deforms the Riemannian metric. Conformal metric deformation preserves infinitesimal circles, as shown in Fig. 3.6. A conformal mapping transforms the infinitesimal circles to the infinitesimal circles. Inspired by the nature of conformal metric deformation, Thurston proposed to use circle packing metric to approximate conformal mapping, which replaces infinitesimal circles to circles with finite sizes.

Figure 3.7 demonstrates the principles. Suppose Ω is a planar simply connected domain. We would like to compute the Riemann mapping $\phi : \Omega \to \mathbb{D}$, which maps Ω to the unit disk. We triangulate the domain Ω, and associate each vertex with a circle. For each edge $[v_i, v_j]$, the two circles centered at the end vertices are tangent to each other. Then we change the radii of all circles, preserving their tangential relations, and the combinatorial structure of the triangulation. Then

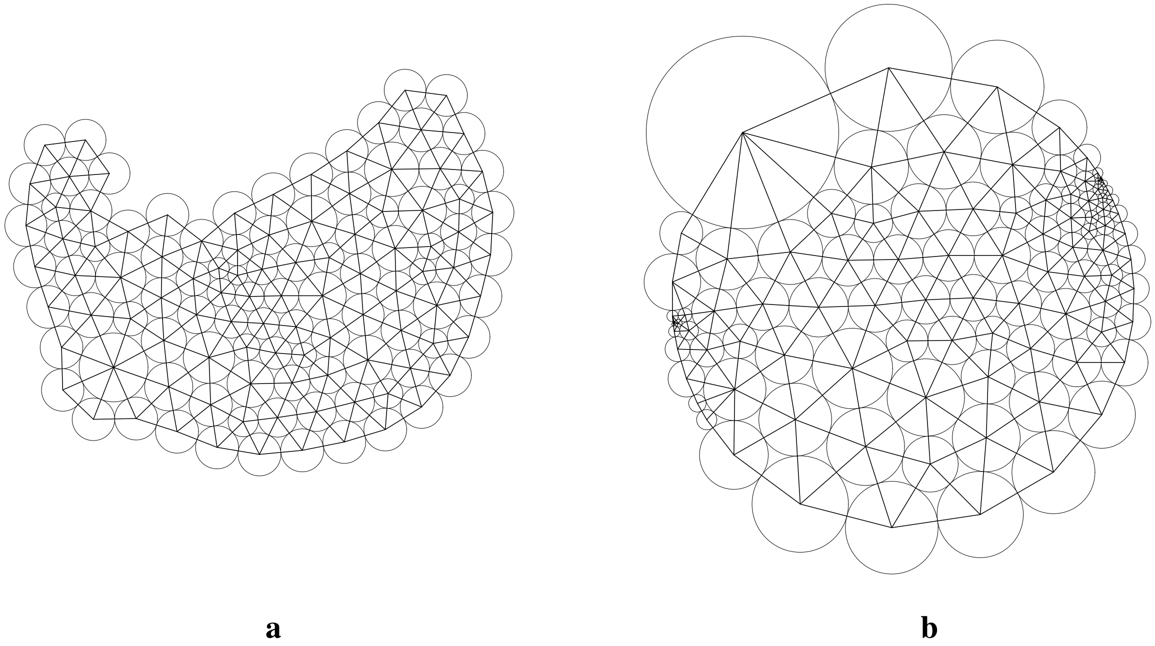

Figure 3.7: Discrete Riemann mapping using circle packing. **a** Domain, **b** Range

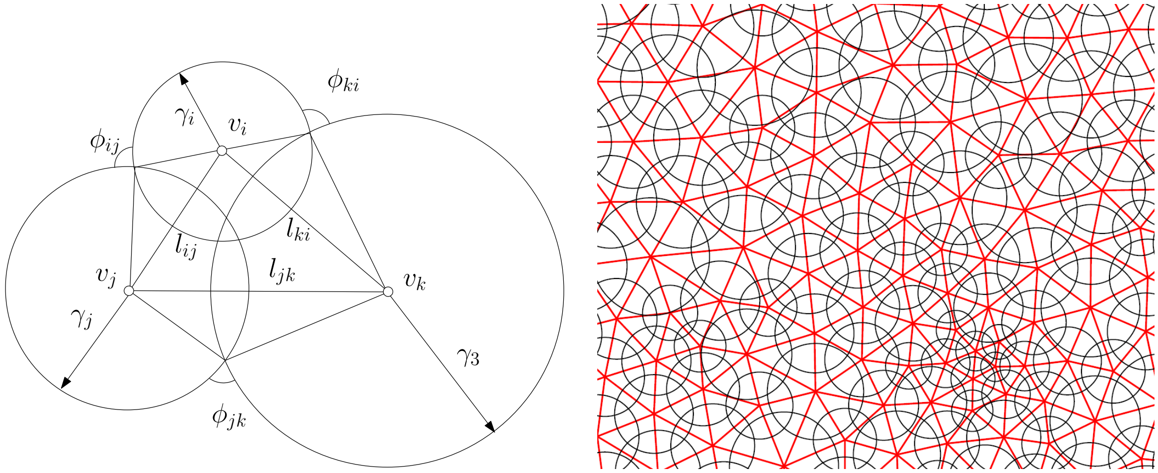

Figure 3.8: Circle packing metric

we deform the domain Ω to a convex polygon, which approximates the unit disk. The mapping constructed is a linear map on each triangle, the mapping also preserves the circle pattern. Thurston [70] conjectured that when the tessellation goes to infinitely refiner, then the piece-wise linear map converges to the real Riemannian mapping. The conjecture was proven by Sullivan and Rodin [65].

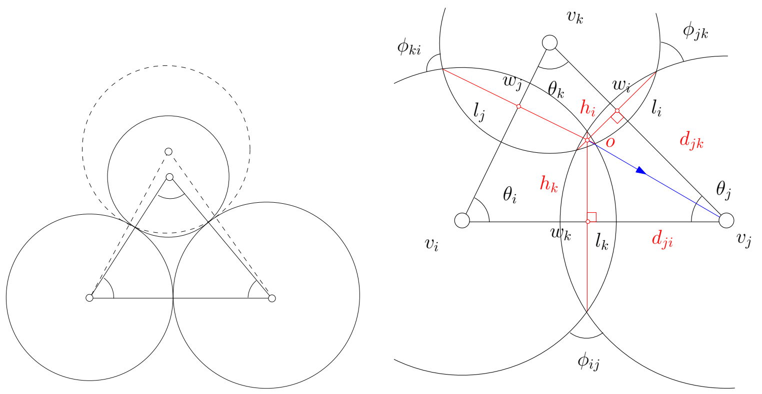

Figure 3.9: Dynamics Behavior
When a circle centered at a vertex is enlarged, the total area increases, the corner angle at the circle center shrinks, and the other two angles increase

Let Σ be a triangular mesh. We associate each vertex v_i with a circle with radius γ_i. As shown in Fig. 3.8, on one triangle face $[v_i, v_j, v_k]$, the circle at v_i and the circle at v_j intersect at the angle ϕ_{ij}, the length of the edge $[v_i, v_j]$ is denoted as l_{ij}. Then edge lengths are given by

$$l_{ij}^2 = \gamma_i^2 + \gamma_j^2 + 2\gamma_i\gamma_j \cos\phi_{ij}.$$

Definition 19 (Circle Packing Metric)**.** *A circle packing metric is a triple* (Σ, Γ, Φ)*,* Σ *represents the triangulation,*

$$\Gamma = \{\gamma_i | \forall v_i\}, \Phi = \{\phi_{ij} | \forall e_{ij}\}.$$

Definition 20 (Discrete Conformal Factor)**.** *Discrete conformal factor on a mesh* Σ *is a function defined on each vertex* $\mathbf{u} : V \to \mathbb{R}$,

$$u_i = \log\gamma_i.$$

Figure 3.9 shows the dynamics behavior for the tangential circle packing. Given a triangle $[v_i, v_j, v_k]$, the circles centered at v_i, v_j, v_k are C_i, C_j, C_k. There is a unique circle orthogonal to three circles $\{C_i, C_j, C_k\}$, which is called the *power circle*, the center of the power circle is called the *power center*. Intuitively, when one circle C_j centered at v_j is enlarged, the total area of the triangle will be increased. But the corresponding angle θ_j will be decreased, and the other two angles θ_i, θ_k are increased. We prove this intuition in a rigorous way.

Proposition 1. *Given a triangle* $[v_i, v_j, v_j]$ *with a circle packing, the positions of* v_i *and* v_k *are fixed. Let* o *be the power center, the position* v_j

$$\frac{\partial v_j}{\partial u_j} = v_j - o.$$

Proof. From $l_k^2 = \langle v_j - v_i, v_j - v_i \rangle$, we obtain

$$\frac{\partial l_k}{\partial u_j} = \langle \frac{\partial v_j}{\partial u_j}, \frac{v_j - v_i}{l_k} \rangle = d_{ji}.$$

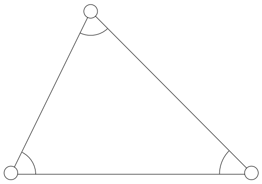

Figure 3.10: A Euclidean triangle

Similarly,

$$\frac{\partial l_i}{\partial u_j} = \langle \frac{\partial v_j}{\partial u_j}, \frac{v_j - v_k}{l_i} \rangle = d_{jk}.$$

Therefore $\frac{\partial v_j}{\partial u_j} = v_j - o$. □

3.2.2 Euclidean Derivative Cosine Law

Suppose $[v_i, v_j, v_k]$ is a Euclidean triangle. We treat each corner angle $\theta_i, \theta_j, \theta_k$ as the function of edge lengths l_i, l_j, l_k, then

Lemma 1 (Derivative Cosine Law)**.**

$$\frac{\partial \theta_i}{\partial l_i} = \frac{l_i}{A}, \frac{\partial \theta_i}{\partial l_j} = -\frac{\partial \theta_i}{\partial l_i} \cos\theta_k,$$

where $A = l_j l_k \sin\theta_i$.

Proof. The proof is by direct computation. From cosine law

$$2 l_j l_k \cos\theta_i = l_j^2 + l_k^2 - l_i^2.$$

On both sides, taking the derivative with respect to l_i, we obtain $d\theta_i/dl_i = l_i/A$. Taking the derivative with respect to l_j, we get

$$\frac{\partial \theta_i}{\partial l_j} = -\frac{l_i \cos\theta_k}{A} = -\frac{\partial \theta_i}{\partial l_i} \cos\theta_k.$$

□

We rewrite the lemma in the matrix format,

$$\begin{pmatrix} d\theta_i \\ d\theta_j \\ d\theta_k \end{pmatrix} = \frac{-1}{A} \begin{pmatrix} l_i & 0 & 0 \\ 0 & l_j & 0 \\ 0 & 0 & l_k \end{pmatrix} \begin{pmatrix} -1 & \cos\theta_k & \cos\theta_j \\ \cos\theta_k & -1 & \cos\theta_i \\ \cos\theta_j & \cos\theta_i & -1 \end{pmatrix} \begin{pmatrix} dl_i \\ dl_j \\ dl_k \end{pmatrix}. \tag{3.2.1}$$

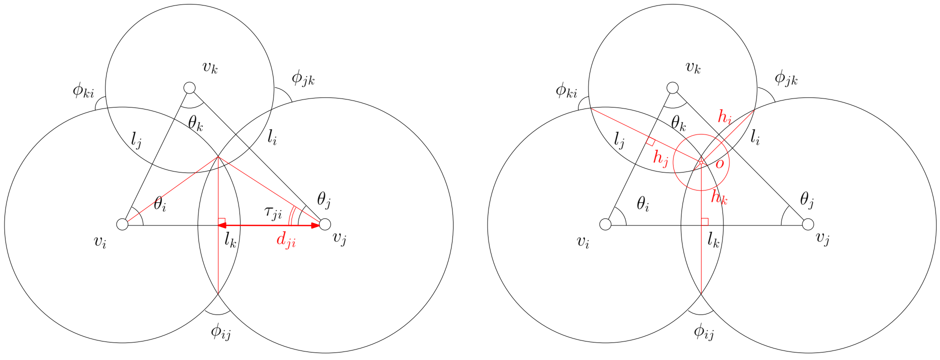

a **b**

Figure 3.11: Derivative cosine law

Lemma 2. *In triangle* $[v_i, v_j, w_k]$,

$$\frac{\partial l_k}{\partial u_j} = d_{ji},$$

as shown in Fig. 3.11 ***a****.*

Proof. According to the Euclidean cosine law $l_k^2 = r_i^2 + r_j^2 + 2\cos\phi_{ij} r_i r_j$, taking the derivative with respect to l_k on both sides, we get

$$\frac{\partial l_k}{\partial r_j} = \frac{r_j + r_i \cos\phi_{ij}}{l_k},$$

therefore

$$\frac{\partial l_k}{\partial u_j} = r_j \frac{\partial l_k}{\partial r_j} = \frac{2r_j^2 + 2r_i r_j \cos\phi_{ij}}{2l_k} = \frac{l_k^2 + r_j^2 - r_i^2}{2l_k} = 2\frac{l_k r_j \cos\tau_{ji}}{2l_k} = r_j \cos\tau_{ji} = d_{ji}.$$

□

Namely,

$$\begin{pmatrix} dl_i \\ dl_j \\ dl_k \end{pmatrix} = \begin{pmatrix} \frac{1}{2l_i} & 0 & 0 \\ 0 & \frac{1}{2l_j} & 0 \\ 0 & 0 & \frac{1}{2l_k} \end{pmatrix} \begin{pmatrix} 0 & l_i^2 + r_j^2 - r_k^2 & l_i^2 + r_k^2 - r_j^2 \\ l_j^2 + r_i^2 - r_k^2 & 0 & l_j^2 + r_k^2 - r_i^2 \\ l_k^2 + r_i^2 - r_j^2 & l_k^2 + r_j^2 - r_i^2 & 0 \end{pmatrix} \begin{pmatrix} du_i \\ du_j \\ du_k \end{pmatrix}. \tag{3.2.2}$$

Furthermore,

$$\begin{pmatrix} dl_i \\ dl_j \\ dl_k \end{pmatrix} = \begin{pmatrix} 0 & d_{jk} & d_{kj} \\ d_{ik} & 0 & d_{ki} \\ d_{ij} & d_{ji} & 0 \end{pmatrix} \begin{pmatrix} du_i \\ du_j \\ du_k \end{pmatrix}. \tag{3.2.3}$$

Suppose the distances from the power center o to the edges $[v_i, v_j]$, $[v_j, v_k]$ and $[v_k, v_i]$ are h_k, h_i and h_i. Now we can show a property for d_{ij}.

Lemma 3. *For the triangle* $[v_i, v_j, w_k]$*,,*

$$d_{ij}^2 + d_{jk}^2 + d_{ki}^2 = d_{ji}^2 + d_{kj}^2 + d_{ik}^2.$$

Proof. By Pythagorean theorem,

$$d_{ij}^2 + h_k^2 = d_{ik}^2 + h_j^2, d_{jk}^2 + h_i^2 = d_{ji}^2 + h_k^2, d_{ki}^2 + h_j^2 = d_{kj}^2 + h_i^2.$$

Adding both sides, we complete the proof. ☐

Lemma 4 (Symmetry)**.** *In triangle* $[v_i, v_j, w_k]$*,*

$$\frac{\partial \theta_i}{\partial u_j} = \frac{d\theta_j}{du_i} = \frac{h_k}{l_k}, \frac{\partial \theta_j}{\partial u_k} = \frac{d\theta_k}{du_j} = \frac{h_i}{l_i}, \frac{\partial \theta_k}{\partial u_i} = \frac{d\theta_i}{du_k} = \frac{h_j}{l_j}, \tag{3.2.4}$$

and

$$\frac{\partial \theta_i}{\partial u_i} = -\frac{\partial \theta_i}{\partial u_j} - \frac{\partial \theta_i}{\partial u_k}, \frac{\partial \theta_j}{\partial u_j} = -\frac{\partial \theta_j}{\partial u_k} - \frac{\partial \theta_j}{\partial u_i}, \frac{\partial \theta_k}{\partial u_k} = -\frac{\partial \theta_k}{\partial u_i} - \frac{\partial \theta_k}{\partial u_j}, \tag{3.2.5}$$

as shown in Fig. (3.11) ***b****.*

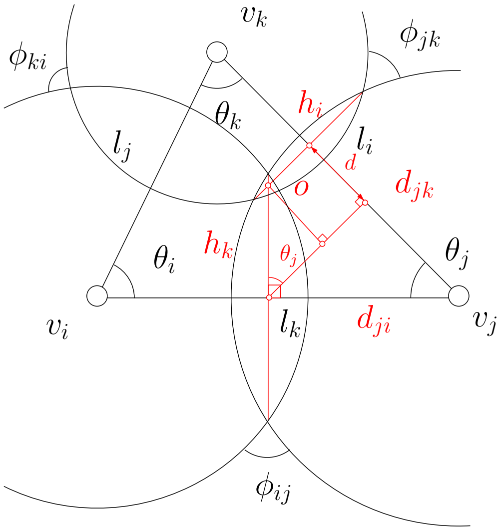

Figure 3.12: $\frac{d\theta_i}{du_j} = \frac{h_k}{l_k}$

Proof. First we prove equations in (4.1.7). From Lemma 1,

$$\frac{\partial \theta_i}{\partial u_j} = \frac{\partial \theta_i}{\partial l_i}\frac{\partial l_i}{\partial u_j} + \frac{\partial \theta_i}{\partial l_k}\frac{\partial l_k}{\partial u_j} = \frac{\partial \theta_i}{\partial l_i}\left(\frac{\partial l_i}{\partial u_j} - \frac{\partial l_k}{\partial u_j}\cos\theta_j\right).$$

From Lemma 2 and examine Fig. 3.12, the right hand side of the above equation equals

$$\frac{l_i}{A}(d_{jk} - d_{ji}\cos\theta_j) = \frac{dl_i}{l_i l_k \sin\theta_j} = \frac{h_k \sin\theta_j}{l_k \sin\theta_j} = \frac{h_k}{l_k}.$$

Then we prove equations in (3.2.5). Because $\theta_i + \theta_j + \theta_k = \pi$, therefore

$$\frac{\partial \theta_i}{\partial u_i} = -\frac{\partial \theta_j}{\partial u_i} - \frac{\partial \theta_k}{\partial u_i} = -\frac{\partial \theta_i}{\partial u_j} - \frac{\partial \theta_i}{\partial u_k}.$$

□

We formulate the lemma in the matrix format by combining the matrix formulae (3.2.1) and (3.2.3),

$$\begin{pmatrix} d\theta_i \\ d\theta_j \\ d\theta_k \end{pmatrix} = -\begin{pmatrix} \frac{h_k}{l_k} + \frac{h_j}{l_j} & -\frac{h_k}{l_k} & -\frac{h_j}{l_j} \\ -\frac{h_k}{l_k} & \frac{h_k}{l_k} + \frac{h_i}{l_i} & -\frac{h_i}{l_i} \\ -\frac{h_j}{l_j} & -\frac{h_i}{l_i} & \frac{h_j}{l_j} + \frac{h_i}{l_i} \end{pmatrix} \begin{pmatrix} du_i \\ du_j \\ du_k \end{pmatrix}. \tag{3.2.6}$$

Now let's consider the admissible space of (u_i, u_j, u_k).

Lemma 5 (Admissible Space)**.** *For any three non-obtuse angles $\phi_{ij}, \phi_{jk}, \phi_{ki} \in [0, \frac{\pi}{2}]$ and any three positive numbers r_1, r_2 and r_3, there is a configuration of* 3 *circles in Euclidean geometry, uniquely up to isometry, having radii r_i and meeting in angles ϕ_{ij}.*

Proof. It is sufficient and necessary to show triangle inequality holds.

$$max\{r_i^2, r_j^2\} < r_i^2 + r_j^2 + 2r_ir_j \cos\phi_{ij} \le (r_i + r_j)^2,$$

$$max\{r_i, r_j\} < l_k \le r_i + r_j,$$

so

$$l_k \le r_i + r_j < l_i + l_j.$$

□

Therefore, if the angles $\phi_{ij}, \phi_{jk}, \phi_{ki}$ are non-obtuse, the admissible space for (u_i, u_j, u_k) is $\mathbb{R}^3$.

Lemma 6. *The differential form*

$$\omega = \theta_i du_i + \theta_j du_j + \theta_k du_k$$

is an exact 1-form.

Proof. Because $\frac{\partial \theta_i}{\partial u_j} = \frac{\partial \theta_j}{\partial u_i}$, so

$$d\omega = (\frac{\partial \theta_i}{\partial u_j} - \frac{\partial \theta_j}{\partial u_i}) du_j \wedge du_i + (\frac{\partial \theta_j}{\partial u_k} - \frac{\partial \theta_k}{\partial u_j}) du_k \wedge du_j + (\frac{\partial \theta_k}{\partial u_i} - \frac{\partial \theta_i}{\partial u_k}) du_i \wedge du_k = 0.$$

Therefore ω is a closed 1-form. Furthermore, the admissible space for (u_i, u_j, u_k) is $\mathbb{R}^3$, so ω is exact. □

Because ω is an exact form, it is the gradient of a function, which is the discrete Ricci energy defined on all the circle packing metrics on the single triangle with inter section angles $(\phi_{ij}, \phi_{jk}, \phi_{ki})$.

Definition 21 (Discrete Ricci Energy)**.** *The discrete Ricci energy is given by*

$$E(u_i, u_j, u_k) = \int_{(0,0,0)}^{(u_i,u_j,u_k)} \omega.$$

Theorem 12 (Concavity of Discrete Ricci Energy)**.** *The Ricci energy $E(u_1, u_2, u_3)$ is strictly concave on the subspace $u_1 + u_2 + u_3 = 0$.*

Proof. The gradient $\nabla E = (\theta_1, \theta_2, \theta_3)$, the Hessian matrix is

$$H = \begin{pmatrix} \frac{\partial \theta_1}{\partial u_1} & \frac{\partial \theta_1}{\partial u_2} & \frac{\partial \theta_1}{\partial u_3} \\ \frac{\partial \theta_2}{\partial u_1} & \frac{\partial \theta_2}{\partial u_2} & \frac{\partial \theta_2}{\partial u_3} \\ \frac{\partial \theta_3}{\partial u_1} & \frac{\partial \theta_3}{\partial u_2} & \frac{\partial \theta_3}{\partial u_3} \end{pmatrix} = - \begin{pmatrix} \frac{h_3}{l_3} + \frac{h_2}{l_2} & -\frac{h_3}{l_3} & -\frac{h_2}{l_2} \\ -\frac{h_3}{l_3} & \frac{h_3}{l_3} + \frac{h_1}{l_1} & -\frac{h_1}{l_1} \\ -\frac{h_2}{l_2} & -\frac{h_1}{l_1} & \frac{h_2}{l_2} + \frac{h_1}{l_1} \end{pmatrix}.$$

$-H$ is diagonal dominant, with null space $(1, 1, 1)$. On the subspace $u_1 + u_2 + u_3 = 0$, H is strictly negative definite. Therefore the discrete Ricci energy $E(u_1, u_2, u_3)$ is strictly concave. ☐

3.2.3 Discrete Ricci Energy

Now, we can generalize the discrete Ricci energy to the whole triangular mesh.

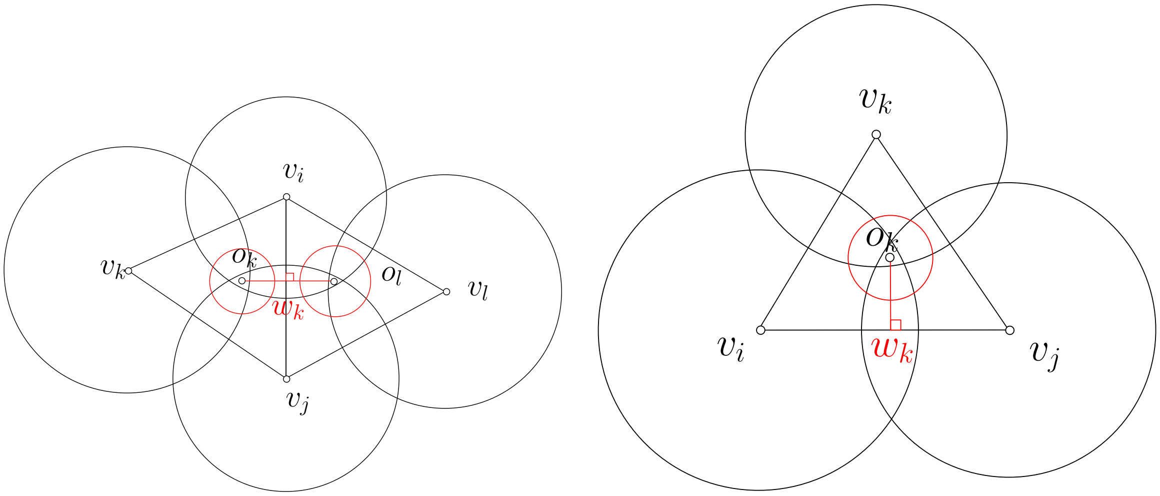

Figure 3.13: Edge weight w_{ij}

Definition 22 (Edge Weight)**.** *Suppose $[v_i, v_j]$ is an interior edge of a triangular mesh Σ, adjacent to two faces $[v_i, v_j, v_k]$ and $[v_j, v_i, v_l]$. Suppose the mesh is with a circle packing metric. Each face has a power center, o_k for $[v_i, v_j, v_k]$, o_l for $[v_j, v_i, v_l]$. After the two faces are flattened, the edge weight for $[v_i, v_j]$ is given by*

$$w_{ij} = \frac{|o_k - o_l|}{|v_i - v_j|},$$

If $[v_i, v_j]$ is a boundary edge, then draw a line from o_k perpendicular to the edge, the perpendicular foot is w_k, then the edge weight is given by

$$w_{ij} = \frac{|o_k - w_k|}{|v_i - v_j|}.$$

Lemma 7. *Suppose $[v_i, v_j]$ is an edge on the mesh Σ with a circle packing metric. Then*

$$\frac{\partial K_i}{\partial u_j} = \frac{\partial K_j}{\partial u_i} = -w_{ij}. \tag{3.2.7}$$

Proof. See Fig. 3.13. Suppose $[v_i, v_j]$ is an interior edge. According to (4.1.7),

$$\frac{\partial \theta_i^{jk}}{\partial u_j} = \frac{|o_k - w_k|}{|v_i - v_j|}, \frac{\partial \theta_i^{jl}}{\partial u_j} = \frac{|o_l - w_k|}{|v_i - v_j|},$$

we have

$$\frac{\partial K_i}{\partial u_j} = -\frac{\partial \theta_i^{jk}}{\partial u_j} - \frac{\partial \theta_i^{jl}}{\partial u_j} = -\frac{|o_k - o_l|}{|v_i - v_j|} = -w_{ij}.$$

Similarly, if $[v_i, v_j]$ is a boundary edge, then

$$\frac{\partial K_i}{\partial u_j} = -\frac{\partial \theta_i^{jk}}{\partial u_j} = -\frac{|o_k - d_k|}{|v_i - v_j|} = -w_{ij}.$$

Therefore, we get

$$\frac{\partial K_i}{\partial u_j} = \frac{\partial K_j}{\partial u_i}.$$

□

Lemma 8. *Suppose v_i is a vertex of a mesh Σ with a circle packing metric. Then*

$$\frac{\partial K_i}{\partial u_i} = -\sum_{j \neq i} \frac{\partial K_i}{\partial u_j} = \sum_{j \neq i} w_{ij}. \tag{3.2.8}$$

Proof. Consider all the faces adjacent to v_i, $[v_i, v_j, v_k]$, then according (3.2.5),

$$\frac{\partial \theta_i^{jk}}{\partial u_i} = -\frac{\partial \theta_j^{ki}}{\partial u_i} - \frac{\partial \theta_k^{ij}}{\partial u_i}$$

therefore

$$\frac{\partial K_i}{\partial u_i} = -\sum_{jk} \frac{\partial \theta_i^{jk}}{\partial u_i} = \sum_{jk} (\frac{\partial \theta_j^{ki}}{\partial u_i} + \frac{\partial \theta_k^{ij}}{\partial u_i}) = -\sum_j \frac{\partial K_j}{\partial u_i} = \sum_j w_{ij}.$$

□

Definition 23 (Admissible Metric Space)**.** *Suppose Σ is a triangular mesh. Fix the circle intersection angles $\Phi = \{\phi_{ij}\}$. Let the vector of logarithms of circle radii be $\mathbf{u} = (u_1, u_2, \cdots, u_n)^T$. Then if triangle inequalities hold on all faces of Σ, namely, (Σ, Φ, Γ) is a circle packing metric, then we say $\mathbf{u}$ is admissible. The space of all admissible $\mathbf{u}$ vectors is called the admissible metric space for (Σ, Φ), and denoted as $U(\Sigma, \Phi)$.*

Definition 24 (Curvature Map)**.** *Given an admissible metric $\mathbf{u} \in U(\Sigma, \Phi)$, it induces the Gauss curvature on the mesh. The curvatures on all vertices is represented as a vector $\mathbf{k} = (K_1, K_2, \cdots, K_n)$. The mapping from metric $\mathbf{u}$ to the curvature vector $\mathbf{k}$ is called the* curvature map*, and denoted as $\kappa : U(\Sigma, \Phi) \to \mathbb{R}^n$.*

The image of the curvature map is called the admissible curvature space.

Definition 25 (Admissible Curvature Space)**.** *Suppose Σ is a triangular mesh. Fix the circle intersection angles $\Phi = \{\phi_{ij}\}$. Then the space of all possible curvatures $\mathbf{k} = (K_1, K_2, \cdots, K_n)$, which is induced by an admissible metric $\mathbf{u} \in U(\Sigma, \Phi)$, is called the admissible curvature space and denoted as $K(\Sigma, \Phi)$.*

$$K(\Sigma, \phi) := \kappa(U(\Sigma, \Phi)).$$

Due to the discrete Gauss-Bonnet theorem 11, the total curvature is determined by the topology of Σ. Therefore

$$K(\Sigma, \phi) \subset \{\sum_{i=1}^n K_i = 2\pi\chi(\Sigma)\}.$$

Lemma 9 (Admissible Metric Space)**.** *Given a triangular mesh Σ, fix circle intersection angles Φ, such that all ϕ_{ij} are non-obtuse angles, $\phi_{ij} \in [0, \frac{\pi}{2}]$, then the admissible metric space with for (Σ, Φ) is $\mathbb{R}^n$,*

$$U(\Sigma, \Phi) = \mathbb{R}^n.$$

Proof. According to Lemma 5, for each face $[v_i, v_j, v_k]$, the admissible metric space $\Omega([v_i, v_j, v_k])$ is $\mathbb{R}^n$, the admissible metric space of the whole mesh Σ is the intersection of the admissible metric spaces of all faces

$$\Omega(\Sigma) = \bigcap_{[v_i, v_j, v_k] \in \Sigma} \Omega([v_i, v_j, v_k]) = \mathbb{R}^n.$$

□

Corollary 1. *The differential form*

$$\omega = \sum_{i=1}^{n} K_i du_i$$

is an exact 1-form.

Proof. Lemma 7 shows ω is closed. Because the admissible metric space is simply connected, therefore ω is exact. □

So we can define the Ricci energy, using ω as gradient.

Definition 26 (Discrete Ricci Energy)**.** *The discrete Ricci energy is defined on the admissible metric space for* (Σ, Φ)*,*

$$E(u_1, u_2, \cdots, u_n) = \int_{(0,0,\cdots,0)}^{(u_1,u_2,\cdots,u_n)} \omega.$$

Theorem 13 (Convexity of Ricci Energy)**.** *The discrete Ricci energy is strictly convex on the space*

$$\sum_{i=1}^{n} u_i = 0.$$

Proof. Here we give two proofs. The first proof is based on the concavity of the discrete Ricci energy on each triangle. Suppose there are V_0 interior vertices and V_1 boundary vertices. Let $E(\Sigma)$ represent the Ricci energy of the whole mesh, $E([v_i, v_j, v_k])$ the energy on the face.

$$E(\Sigma) = \sum_{v_i \notin \partial\Sigma} 2\pi u_i + \sum_{v_j \in \partial\Sigma} \pi u_j - \sum_{[v_i,v_j,v_k] \in \Sigma} E([v_i, v_j, v_k]),$$

the linear terms won't affect the convexity. For all the faces, according to Theorem 12, $E([v_i, v_j, v_k])$ is strictly concave on the space $u_i + u_j + u_k = 0$. The null space of the Hessian of $E([v_i, v_j, v_k])$ is $u_i = u_j = u_k$. Therefore, the null space of the Hessian of $E(\Sigma)$ is the intersection of all the face null spaces, namely the one dimensional space spanned by $(1, 1, 1, \cdots, 1)^T$. In the complement space $\sum_i u_i = 0$, $E(\Sigma)$ is the negative sum of concave functions $E([v_i, v_j, v_k])$, so it is strictly convex.

The second proof is to directly compute the Hessian matrix of the energy. The gradient of $E(\Sigma)$ is

$$\nabla E(\Sigma) = (K_1, K_2, \cdots, K_n)^T.$$

Therefore, the element of the Hessian matrix

$$\left(\frac{\partial^2 E(\Sigma)}{\partial u_i \partial u_j} \right) = \frac{\partial K_i}{\partial u_j}.$$

According to Lemmas 7 and 8, if v_i is adjacent to v_j, $\frac{K_i}{\partial u_j} = -w_{ij}$, otherwise 0. The diagonal elements $\frac{K_i}{\partial u_i} = \sum_{j \neq i} w_{ij}$. Therefore, the Hessian matrix is diagonal dominant, with one dimensional null space, spanned by $(1, 1, \cdots, 1)^T$. In the space $\sum_i u_i = 0$, the energy is strictly convex. □

Note that, the differential of the curvature and logarithm of radius satisfies the Laplace equation

$$dK_i = \sum_j w_{ij}(du_i - du_j).$$

The admissible curvature space is also convex, which can be described by the following lemma.

Lemma 10 (Admissible Curvature Space)**.** *Suppose Σ is a triangular mesh, Φ is the circle intersection, all the intersection angles are non-obtuse, $\phi_{ij} \in [0, \frac{\pi}{2}]$. Let I be a proper subset of vertices V. F_i is the collection of faces, whose vertices are in I. The link I is the set of pairs (e,v), where e is an edge, whose vertices are not in I, and vertex $v \in I$, so that (e,v) form a triangle. The for any admissible curvature, the following inequality holds:*

$$\sum_{v_i \in I} K_i > -\sum_{(e,v)\in Lk(I)} (\pi - \phi(e)) + 2\pi\chi(F_I). \tag{3.2.9}$$

Given a curvature vector $\mathbf{k} = (K_1, K_2, \cdots, K_n)$, if for any proper subset I, the inequality (3.3.3) holds, then the curvature is admissible.

3.2.4 Global Rigidity

In the smooth case, the Gauss curvature is determined by the Riemannian metric. The inverse is not true. Different Riemannian metrics may induce the same Gauss curvature functions, but if the Riemannian metrics are restricted to be within a conformal class, then the Gauss curvature can essentially determine the metric. Namely, the solution to the Yamabe equation:

$$\begin{cases} \bar{K} &= e^{-2\lambda}(K - \Delta_{\mathbf{g}}\lambda) \\ \bar{k}_g &= e^{-\lambda}(k_g - \partial_{\mathbf{n},\mathbf{g}}\lambda). \end{cases}$$

is essentially unique. In the discrete case, discrete metrics determine the discrete curvatures. Inversely, discrete curvatures determine the discrete conformal Riemannian metrics. This uniqueness is called the *rigidity*.

Theorem 14 (Global Rigidity)**.** *Suppose Σ is a triangular mesh, with circle packing metrics (Σ, Φ, Γ), where Φ is fixed and all the intersection angles are non-obtuse. Then the curvature map*

$$\kappa : U(\Sigma, \Phi) \bigcap \{\sum_i u_i = 0\} \to K(\Sigma, \Phi)$$

is a global diffeomorphism.

Proof. Consider the discrete Ricci energy $E : U(\Sigma, \Phi) \to \mathbb{R}$, which is with C^2 continuity. By Lemma 9, the domain $U(\Sigma, \Phi)$ is convex, so is the intersection between $U(\Sigma, \Phi)$ and the hyperplane $\sum_i u_i = 0$. By Theorem 13, in $U(\Sigma, \Phi) \bigcap \{\sum_i u_i = 0\}$ the energy is convex. The Legendre transformation [76] induced by the energy is the curvature mapping

$$\kappa : (u_1, u_2, \cdots, u_n) \to \nabla E = (K_1, K_2, \cdots, K_n).$$

By discrete Gauss-Bonnet theorem 11, the total curvature $\sum_i K_i = 2\pi\chi(\Sigma)$. By Theorem **??**, the curvature mapping is a global diffeomorphism. □

3.2.5 Convergence Analysis

The discrete surface Ricci flow is given by

$$\frac{dr_i}{dt} = -K_i r_i,$$

or equivalently, $u_i = \log r_i$,

$$\frac{du_i}{dt} = -K_i.$$

In practice, it is useful to consider normalized Ricci flow

Definition 27 (Normalized Discrete Surface Ricci Flow)**.**

$$\frac{du_i}{dt} = \bar{K} - K_i, \tag{3.2.10}$$

where $\bar{K}$ is the average vertex curvature, $\bar{K} = 2\pi\chi(\Sigma)/n$, and n is the number of vertices.

It is easy to see that the normalized Ricci flow (3.2.10) is the negative gradient flow of the energy,

$$E(\mathbf{u}) = \int \sum_{i=1}^{n} (K_i - \bar{K}) du_i = \int \sum_{i=1}^{n} K_i du_i - \bar{K} \sum_{i=1}^{n} u_i.$$

If we ignore the linear term, then the energy is convex. It has the unique global minimum, where the gradient is zero, namely $\nabla E(\mathbf{u}) = (K_1 - \bar{K}, K_2 - \bar{K}, \cdots, K_n - \bar{K})$ is zero vector. If the average curvature is in the admissible curvature space, then the negative gradient flow leads to the global minimum. Therefore, we show the convergence theorem: In order to check whether the average curvature is admissible, we can verify the inequality (3.3.3) for all proper vertex subsets.

Theorem 15 (Convergence of Discrete Ricci Flow)**.** *Suppose Σ is a triangular mesh with non-obtuse intersection angles $\phi_{ij} \in [0, \frac{\pi}{2}]$. If for any proper subset of the vertices $I \subset V$,*

$$\frac{2\pi|I|\chi(\Sigma)}{n} > -\sum_{(e,v)\in Lk(I)} (\pi - \phi(e)) + 2\pi\chi(F_I),$$

then the discrete surface Ricci flow converges to the metric of constant curvature $2\pi(\Sigma)/n$.

Furthermore, we can estimate the convergence rate of the discrete Ricci flow.

Theorem 16 (Exponential convergence rate)**.** *The discrete surface Ricci flow converges exponentially fast to the constant curvature metric, for every vertex v_i,*

$$(K_i(t) - \bar{K})^2 \leq c_2 e^{-c_1 t},$$

where c_1, c_2 are positive constants.

In order to prove the convergence and convergence rate of discrete Ricci flow, we need the following lemma,

Lemma 11. *Suppose Σ is a connected triangular mesh. Then there exists a constant $c_3 > 0$ depending only on Σ so that*

$$\sum_{i=1}^{n}(K_i - \bar{K})^2 \leq c_3 \sum_{[v_i,v_j]\in\Sigma}(K_i - K_j)^2. \tag{3.2.11}$$

for all time $t > 0$.

Proof. According to Cauchy's inequality $\langle \mathbf{x},\mathbf{y}\rangle^2 \leq \langle \mathbf{x},\mathbf{x}\rangle\langle \mathbf{y},\mathbf{y}\rangle$, let

$$\mathbf{x} = (a_i - a_1, a_i - a_2, \cdots, a_i - a_n)^T, \mathbf{y} = (1,1,\cdots,1),$$

then

$$(a_i - \bar{a})^2 \leq \frac{1}{n}\left(\sum_{j=1}(a_i - a_j)^2\right).$$

We obtain

$$\sum_{i=1}^{n}(K_i - \bar{K})^2 \leq \frac{1}{n}\sum_{i,j=1}^{n}(K_i - K_j)^2. \tag{3.2.12}$$

On the other hand, since the surface Σ is connected, for any two vertices $v_i, v_j \in \Sigma$, there exists a shortest path between them. The path is represented as a sequence of vertices $v_{m_1} = v_i, \cdots, v_{m_l} = v_j$, so that v_{m_k} and $v_{m_{k+1}}$ are adjacent. The value

$$(K_i - K_j)^2 = \left(\sum_{k=1}^{l-1}(K_{m_k} - K_{m_{k+1}})\right)^2 \leq \sum_{k=1}^{l-1}(K_{m_k} - K_{m_{k+1}})^2.$$

Therefore

$$\sum_{i,j=1}^{n}(K_i - K_j)^2 \leq c_3 n \sum_{[v_i,v_j]\in\Sigma}(K_i - K_j)^2. \tag{3.2.13}$$

By combining (3.2.12) and (3.2.13), we obtain

$$\sum_{i=1}^{n}(K_i - \bar{K})^2 \leq c_3 \sum_{[v_i,v_j]\in\Sigma}(K_i - K_j)^2.$$

This completes the proof for the lemma. □

Now we prove the convergence theorems for discrete Ricci flow.

Proof. During the flow, the energy $E(\mathbf{u})$ decreases monotonously. The path $\mathbf{u}(t)$ in the admissible metric space is contained in a compact subset, $\{\mathbf{u}|E(\mathbf{u}) \leq E_0\}$, where E_0 is the initial energy value. So all $u_i(t)$'s are bounded. The edge weight w_{ij} are smooth functions of $\mathbf{u}$, therefore there exists a constant $c_1 > 0$, such that for all $[v_i, v_j] \in \Sigma$

$$w_{ij}(t) > c_4, t \in [0,\infty). \tag{3.2.14}$$

Consider the energy

$$g(t) := \sum_{i=1}^{n} (K_i(t) - \bar{K})^2.$$

From $n\bar{K} = \sum_{i=1}^{n} K_i(t)$,

$$g(t) = \sum_{i=1}^{n} (K_i^2 + \bar{K}^2 - 2K_i\bar{K}) = \sum_{i=1}^{n} K_i^2 + n\bar{K}^2 - (2\sum_{i} K_i)\bar{K} = \sum_{i=1}^{n} K_i^2(t) - n\bar{K}^2.$$

From $K_i' = \sum_j w_{ij}(u_i' - u_j') = \sum_j w_{ij}(K_j - K_i)$,

$$g'(t) := 2\sum_{i=1}^{n} \sum_{[v_i,v_j]\in\Sigma} w_{ij}K_i(K_j - K_i).$$

By switching the order of i, j, we also have

$$g'(t) = 2\sum_{j=1}^{n} \sum_{[v_i,v_j]\in\Sigma} w_{ij}K_j(K_i - K_j).$$

Thus from (3.2.14) and (3.2.11),

$$g'(t) = -\sum_{[v_i,v_j]\in\Sigma} w_{ij}(K_i - K_j)^2 \leq -c_1 \sum_{[v_i,v_j]\in\Sigma} (K_i - K_j)^2 \leq -\frac{c_4}{c_3}\sum_{i=1}^{n}(K_i - \bar{K})^2 = -\frac{c_1}{c_3}g(t).$$

This implies that $g(t) \leq c_2 e^{-\frac{c_1}{c_3}t}$ for all time $t \geq 0$ and for some constant c_2. Then we obtain

$$(K_i(t) - \bar{K})^2 \leq \sum_{i=1}^{n}(K_i - \bar{K})^2 = g(t) \leq c_2 e^{-\frac{c_4}{c_3}t}.$$

Let c_1 be $\frac{c_4}{c_3}$. This completes the proof. □

3.3 Hyperbolic Discrete Surface Ricci Flow

In practice, it is crucial to handle surfaces with negative Euler characteristic numbers. This requires us to generalize the discrete surface Ricci flow to meshes with hyperbolic background geometry. In the following, we generalize the theoretical frameworks to hyperbolic discrete surfaces. Figure 3.14 shows the uniformization of genus two surfaces, which are computed using the discrete hyperbolic Ricci flow method.

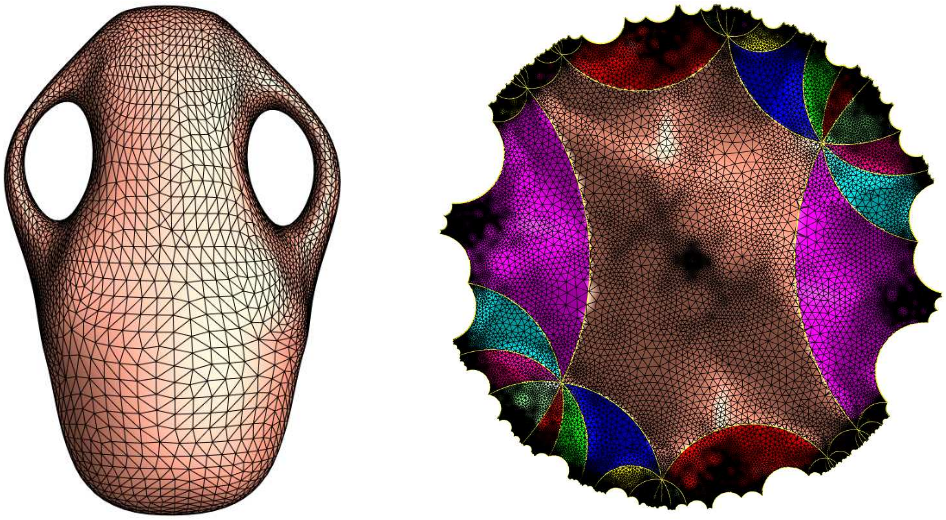

Figure 3.14: Uniformization of high genus surfaces using hyperbolic Ricci flow

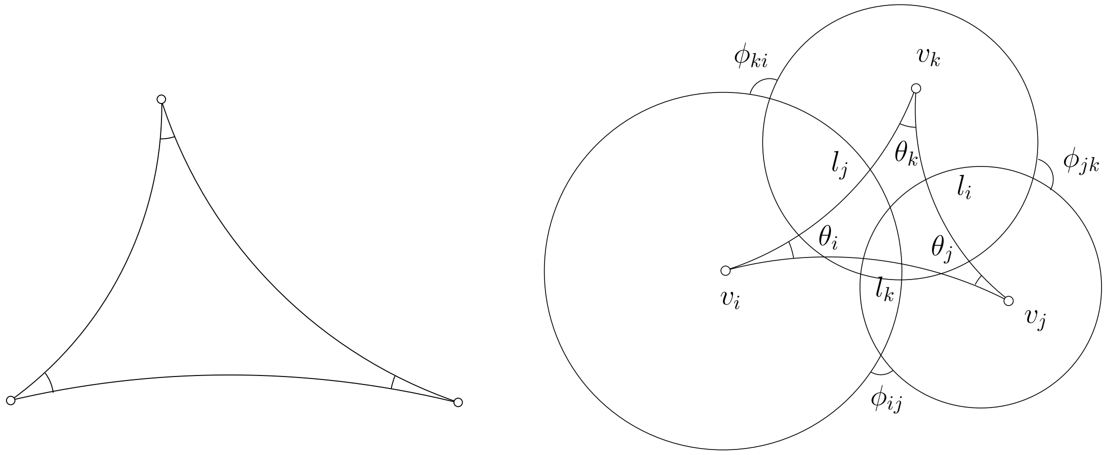

Figure 3.15: A hyperbolic triangle and hyperbolic circle packing

3.3.1 Hyperbolic Derivative Cosine Law

The hyperbolic cosine law and sine law are given by

$$\begin{aligned} \cos\theta_i &= \frac{\cosh l_j \cosh l_k - \cosh l_i}{\sinh l_j \sinh l_k} \\ \frac{\sin\theta_i}{\sinh l_i} &= \frac{\sin\theta_j}{\sinh l_j} = \frac{\sin\theta_k}{\sinh l_k}. \end{aligned}$$

The double area of the hyperbolic triangle, as shown in Fig. 3.15, is

$$A = \sinh l_j \sinh l_k \sin \theta_i.$$

Lemma 12 (Hyperbolic Derivative Cosine Law)**.**

$$\frac{\partial \theta_i}{\partial l_i} = \frac{\sinh l_i}{A}, \frac{\partial \theta_i}{\partial l_j} = -\frac{\sinh l_i}{A} \cos \theta_k.$$

Proof. From the cosine law,

$$\cos \theta_i = \frac{\cosh l_j \cosh l_k - \cosh l_i}{\sinh l_j \sinh l_k}.$$

Taking derivative on both sides with respect to l_i, we get

$$-\sin \theta_i \frac{\partial \theta_i}{\partial l_i} = \frac{-\sinh l_i}{\sinh l_j \sinh l_k},$$

therefore

$$\frac{\partial \theta_i}{\partial l_i} = \frac{\sinh l_i}{A}.$$

Similarly,

$$\begin{aligned}
\cos \theta_i &= \frac{\cosh l_j \cosh l_k - \cosh l_i}{\sinh l_j \sinh l_k} \\
\frac{\partial \theta_i}{\partial l_j} &= \frac{\sinh l_j \cosh l_k (\sinh l_j \sinh l_k) - (-\cosh l_i + \cosh l_j \cosh l_k) \sinh l_k \cosh l_j}{-\sin \theta_i (\sinh l_j \sinh l_k)^2} \\
&= \frac{(\sinh l_j^2 - \cosh l_j^2) \cosh l_k \sinh l_k + \cosh l_i \cosh l_j \sinh l_k}{-\sin \theta_i \sinh l_j^2 \sinh l_k^2} \\
&= \frac{-\cosh l_k + \cosh l_i \cosh l_j}{-A \sinh l_j} \\
&= \frac{\sinh l_i \sinh l_j \cos \theta_k}{-A \sinh l_j} \\
&= -\frac{\sinh l_i}{A} \cos \theta_k.
\end{aligned}$$

□

We write the result in the matrix format:

$$\begin{pmatrix} d\theta_i \\ d\theta_j \\ d\theta_k \end{pmatrix} = \frac{-1}{A} \begin{pmatrix} \sinh_i & 0 & 0 \\ 0 & \sinh_j & 0 \\ 0 & 0 & \sinh_k \end{pmatrix} \begin{pmatrix} -1 & \cos \theta_k & \cos \theta_j \\ \cos \theta_k & -1 & \cos \theta_i \\ \cos \theta_j & \cos \theta_i & -1 \end{pmatrix} \begin{pmatrix} dl_i \\ dl_j \\ dl_k \end{pmatrix}. \qquad (3.3.1)$$

3.3.2 Thurston's Circle Packing

Similar to the Euclidean case, we can use Thurston's circle packing for discrete conformal metric deformation. Then the relation between the edge length and the circle radii is governed by hyperbolic cosine law,

$$\cosh l_i = \cosh r_j \cosh r_k + \sinh r_j \sinh r_k I_{jk},$$

where l_i is the length of the edge $[v_i, v_j]$, I_{ij} is the cosine of the intersection angle between two circles centered at v_i and v_j.

Lemma 13. *The differential relation between the edge lengths and the circle radii is*

$$dl_i = \frac{-\cosh r_k + \cosh l_i \cosh r_j}{\sinh l_i \sinh r_j} dr_j + \frac{-\cosh r_j + \cosh l_i \cosh r_k}{\sinh l_i \sinh r_k} dr_k.$$

Proof.

$$\cosh l_i = \cosh r_j \cosh r_k + \sinh r_j \sinh r_k I_{jk}$$

$$\sinh l_i \frac{dl_i}{dr_j} = \sinh r_j \cosh r_k + I_{jk} \cosh r_j \sinh r_k$$

$$\begin{aligned} \frac{dl_i}{dr_j} &= \frac{\sinh r_j \cosh r_k + \cosh r_j \sinh r_k I_{jk}}{\sinh l_i} \\ I_{jk} &= \frac{\cosh l_i - \cosh r_j \cosh r_k}{\sinh r_j \sinh r_k} \end{aligned}$$

$$\begin{aligned} \frac{dl_i}{dr_j} &= \frac{\sinh r_j \cosh r_k + \cosh r_j \sinh r_k \frac{\cosh l_i - \cosh r_j \cosh r_k}{\sinh r_j \sinh r_k}}{\sinh l_i} \\ &= \frac{\sinh^2 r_j \cosh r_k + \cosh r_j \cosh l_i - \cosh^2 r_j \cosh r_k}{\sinh l_i \sinh r_j} \\ &= \frac{(\sinh^2 r_j - \cosh^2 r_j) \cosh r_k + \cosh r_j \cosh l_i}{\sinh l_i \sinh r_j} \\ &= \frac{\cosh r_j \cosh l_i - \cosh r_k}{\sinh l_i \sinh r_j}. \end{aligned}$$

□

We rewrite the equation in matrix format,

$$\begin{pmatrix} dl_i \\ dl_j \\ dl_k \end{pmatrix} = \begin{pmatrix} \frac{1}{\sinh l_i} & 0 & 0 \\ 0 & \frac{1}{\sinh l_j} & 0 \\ 0 & 0 & \frac{1}{\sinh l_k} \end{pmatrix} M \begin{pmatrix} \frac{1}{\sinh r_i} & 0 & 0 \\ 0 & \frac{1}{\sinh r_j} & 0 \\ 0 & 0 & \frac{1}{\sinh r_k} \end{pmatrix} \begin{pmatrix} dr_i \\ dr_j \\ dr_k \end{pmatrix}, \tag{3.3.2}$$

where

$$M=\begin{pmatrix} 0 & -\cosh r_k+\cosh l_i\cosh r_j & -\cosh r_j+\cosh l_i\cosh r_k \\ -\cosh r_k+\cosh l_j\cosh r_i & 0 & -\cosh r_i+\cosh l_j\cosh r_k \\ -\cosh r_j+\cosh l_k\cosh r_i & -\cosh r_i+\cosh l_k\cosh r_j & 0 \end{pmatrix}.$$

Let the discrete conformal factor $u_i=\log\tanh\frac{r_i}{2}$, $(a,b,c)=(\cosh l_1,\cosh l_2,\cosh l_3)$, and $(x,y,z)=(\cosh r_1,\cosh r_2,\cosh r_3)$. By hyperbolic cosine law, we get the following lemma.

Lemma 14. *The differential relations between the inner angles and discrete conformal factors are*

$$\begin{pmatrix} d\theta_1 \\ d\theta_2 \\ d\theta_3 \end{pmatrix}=N\begin{pmatrix} du_1 \\ du_2 \\ du_3 \end{pmatrix},$$

where

$$N=\begin{pmatrix} 1-a^2 & ab-c & ca-b \\ ab-c & 1-b^2 & bc-a \\ ca-b & bc-a & 1-c^2 \end{pmatrix}\begin{pmatrix} \frac{1}{a2-1} & 0 & 0 \\ 0 & \frac{1}{b^2-1} & 0 \\ 0 & 0 & \frac{1}{c^2-1} \end{pmatrix}\begin{pmatrix} 0 & ay-z & az-y \\ bx-z & 0 & bz-x \\ cx-y & cy-x & 0 \end{pmatrix}.$$

Proof. From $u_i=\log\tanh\frac{r_i}{2}$, we obtain $dr_i=\sinh r_i du_i$. Combining it with (3.3.1) and (3.3.2), we get the formula. □

Lemma 15. *The differential form $\omega=\theta_i du_i+\theta_j du_j+\theta_k du_k$ is closed.*

Proof. By direct computation, for example

$$\frac{\partial\theta_i}{\partial u_j}=\frac{\partial\theta_j}{\partial u_i}=z-\frac{ac-b}{c^2-1}x-\frac{bc-a}{c^2-1}y.$$

□

Lemma 16. *The Admissible metric space is $\mathbb{R}^3$.*

Proof. Because $l_i\le r_j+r_k\le l_j+l_k$, therefore the triangle inequality holds for all possible $\{r_i,r_j,r_k\}$. □

Because the admissible metric space is simply connected, the closed 1-form is exact. We can define discrete Ricci energy as $\int\omega$.

Lemma 17. *The discrete Ricci energy*

$$E(u_i,u_j,u_k)=\int_{(0,0,0)}^{(u_i,u_j,u_k)}\omega$$

is strictly concave.

Proof. It is sufficient to show the Hessian matrix $\left(\frac{\partial\theta_i}{\partial u_j}\right)$ is negative definite. Suppose we increase u_i. Then the hyperbolic triangle area increases as well. According to Gauss-Bonnet theorem,

$$\pi - (\theta_i + \theta_j + \theta_k) = A,$$

therefore $\theta_i + \theta_j + \theta_k$ decreases,

$$\frac{\partial(\theta_i + \theta_j + \theta_k)}{\partial u_i} < 0.$$

This means

$$\frac{\partial\theta_i}{\partial u_i} < -\frac{\partial\theta_j}{\partial u_i} - \frac{\partial\theta_k}{\partial u_i} = -\frac{\partial\theta_i}{\partial u_j} - \frac{\partial\theta_i}{\partial u_k}.$$

On the other hand, $\partial\theta_i/\partial u_j$ is positive. So the negative of the Hessian matrix is diagonal dominant, the Hessian matrix is negative definite. The energy is strictly concave. □

3.3.3 Discrete Hyperbolic Ricci Energy

Let Σ be a triangular mesh with hyperbolic background geometry, Φ is the angle intersection angles, such that for any edge $[v_i, v_j]$, $\phi_{ij} \in [0, \frac{\pi}{2}]$, $u_i = \log\tanh\frac{r_i}{2}$. We can directly show that

$$\omega = \sum_{i=1}^{n} K_i du_i$$

is a closed 1-form. The *admissible metric space* for all circle packing metrics $\mathbf{u} = (u_1, u_2, \cdots, u_n)$ of (Σ, Φ) is $\mathbb{R}^n$. The discrete Ricci energy $\int\omega$ is strictly convex. The curvature map $\kappa : (u_1, u_2, \cdots, u_n) \rightarrow (K_1, K_2, \cdots, K_n)$ is a global diffeomorphism.

Let I be a proper subset of vertices V. F_i is the collection of faces, whose vertices are in I. The link I is the set of pairs (e, v), where e is an edge, whose vertices are not in I, and vertex $v \in I$, so that (e, v) form a triangle. Given a curvature vector $(K_1, K_2, \cdots, K_n)$, if for any proper subset $I \subset V$, the following inequality (3.3.3) holds,

$$\sum_{v_i \in I} K_i > -\sum_{(e,v)\in Lk(I)} (\pi - \phi(e)) + 2\pi\chi(F_I), \tag{3.3.3}$$

then the curvature is admissible.

3.3.4 Hyperbolic Yamabe Flow

Hyperbolic Yamabe flow is defined as

$$\sinh\frac{y_i}{2} = e^{u_i}\sinh\frac{l_k}{2}e^{u_j},$$

where $y_k(t)$ is the edge length during the flow, l_k is the initial edge length, and $y_k(0) = l_k$. Take the derivative with respect to u_i on both sides,

$$\frac{1}{2}\cosh\frac{y_k}{2}\frac{\partial y_k}{\partial u_i} = e^{u_i}\sinh\frac{l_k}{2}e^{u_j} = \sinh\frac{y_k}{2}.$$

Therefore,

$$\frac{\partial y_k}{\partial u_i} = 2\tanh\frac{y_k}{2} = 2\frac{\sinh\frac{y_k}{2}}{\cosh\frac{y_k}{2}} = \frac{2\sinh\frac{y_k}{2}\cosh\frac{y_k}{2}}{\cosh^2\frac{y_k}{2}}.$$

Since $\sinh 2x = 2\sinh x\cosh x$ and $\cosh 2x = 2\cosh^2 x - 1$, we obtain

$$\frac{\partial y_k}{\partial u_i} = \frac{2\sinh y_k}{\cosh y_k + 1}.$$

Therefore,

$$\begin{pmatrix} dy_1 \\ dy_2 \\ dy_3 \end{pmatrix} = 2\begin{pmatrix} \frac{\sinh y_1}{\cosh y_1+1} & 0 & 0 \\ 0 & \frac{\sinh y_2}{\cosh y_2+1} & 0 \\ 0 & 0 & \frac{\sinh y_3}{\cosh y_3+1} \end{pmatrix}\begin{pmatrix} 0 & 1 & 1 \\ 1 & 0 & 1 \\ 1 & 1 & 0 \end{pmatrix}\begin{pmatrix} du_1 \\ du_2 \\ du_3 \end{pmatrix}.$$

We use C_i, S_j to represent $\cosh y_i$ and $\sinh y_j$, respectively, and obtain

$$\begin{pmatrix} d\theta_1 \\ d\theta_2 \\ d\theta_3 \end{pmatrix} = -\frac{2}{A}\begin{pmatrix} S_1 & 0 & 0 \\ 0 & S_2 & 0 \\ 0 & 0 & S_3 \end{pmatrix}\begin{pmatrix} -1 & \cos\theta_3 & \cos\theta_2 \\ \cos\theta_3 & -1 & \cos\theta_1 \\ \cos\theta_2 & \cos\theta_1 & -1 \end{pmatrix}\begin{pmatrix} 0 & \frac{S_1}{C_1+1} & \frac{S_1}{C_1+1} \\ \frac{S_2}{C_2+1} & 0 & \frac{S_2}{C_2+1} \\ \frac{S_3}{C_3+1} & \frac{S_3}{C_3+1} & 0 \end{pmatrix}\begin{pmatrix} du_1 \\ du_2 \\ du_3 \end{pmatrix}$$

$$= -\frac{2}{A}\begin{pmatrix} \frac{S_1S_2\cos\theta_3}{C_2+1} + \frac{S_1S_3\cos\theta_2}{C_3+1} & \frac{-S_1^2}{C_1+1} + \frac{S_1S_3\cos\theta_2}{C_3+1} & \frac{-S_1^2}{C_1+1} + \frac{S_1S_2\cos\theta_3}{C_2+1} \\ \frac{-S_2^2}{C_2+1} + \frac{S_2S_3\cos\theta_1}{C_3+1} & \frac{S_1S_2\cos\theta_3}{C_1+1} + \frac{S_2S_3\cos\theta_1}{C_3+1} & \frac{-S_2^2}{C_2+1} + \frac{S_1S_2\cos\theta_3}{C_1+1} \\ \frac{-S_3^2}{C_3+1} + \frac{S_2S_3\cos\theta_1}{C_2+1} & \frac{-S_3^2}{C_3+1} + \frac{S_1S_3\cos\theta_2}{C_1+1} & \frac{S_1S_3\cos\theta_2}{C_1+1} + \frac{S_2S_3\cos\theta_1}{C_2+1} \end{pmatrix}\begin{pmatrix} du_1 \\ du_2 \\ du_3 \end{pmatrix}.$$

With the hyperbolic cosine law,

$$\cosh y_i = \cosh y_j \cosh y_k - \sinh y_j \sinh y_k \cos\theta_i,$$

we get

$$S_j S_k \cos\theta_i l = C_j C_k - C_i.$$

and $\cosh^2 x - \sinh^2 x = 1$, the right hand side becomes

$$-\frac{2}{A}\begin{pmatrix} \frac{C_1C_2-C_3}{C_2+1} + \frac{C_1C_3-C_2}{C_3+1} & \frac{1-C_1^2}{C_1+1} + \frac{C_1C_3-C_2}{C_3+1} & \frac{1-C_1^2}{C_1+1} + \frac{C_1C_2-C_3}{C_2+1} \\ \frac{1-C_2^2}{C_2+1} + \frac{C_2C_3-C_1}{C_3+1} & \frac{C_1C_2-C_3}{C_1+1} + \frac{C_2C_3-C_1}{C_3+1} & \frac{1-C_2^2}{C_2+1} + \frac{C_1C_2-C_3}{C_1+1} \\ \frac{1-C_3^2}{C_3+1} + \frac{C_2C_3-C_1}{C_2+1} & \frac{1-C_3^2}{C_3+1} + \frac{C_1C_3-C_2}{C_1+1} & \frac{C_1C_3-C_2}{C_1+1} + \frac{C_2C_3-C_1}{C_2+1} \end{pmatrix}\begin{pmatrix} du_1 \\ du_2 \\ du_3 \end{pmatrix}.$$

We get

$$\begin{aligned} \frac{\partial\theta_1}{\partial u_2} &= -\frac{2}{A}\left(\frac{1-C_1^2}{C_1+1} + \frac{C_1C_3-C_2}{C_3+1}\right) \\ &= -\frac{2}{A}\left(1 - C_1 + \frac{C_1C_3-C_2}{C_3+1}\right) = \frac{C_1+C_2-C_3-1}{A(1+C_3)/2} \end{aligned}$$

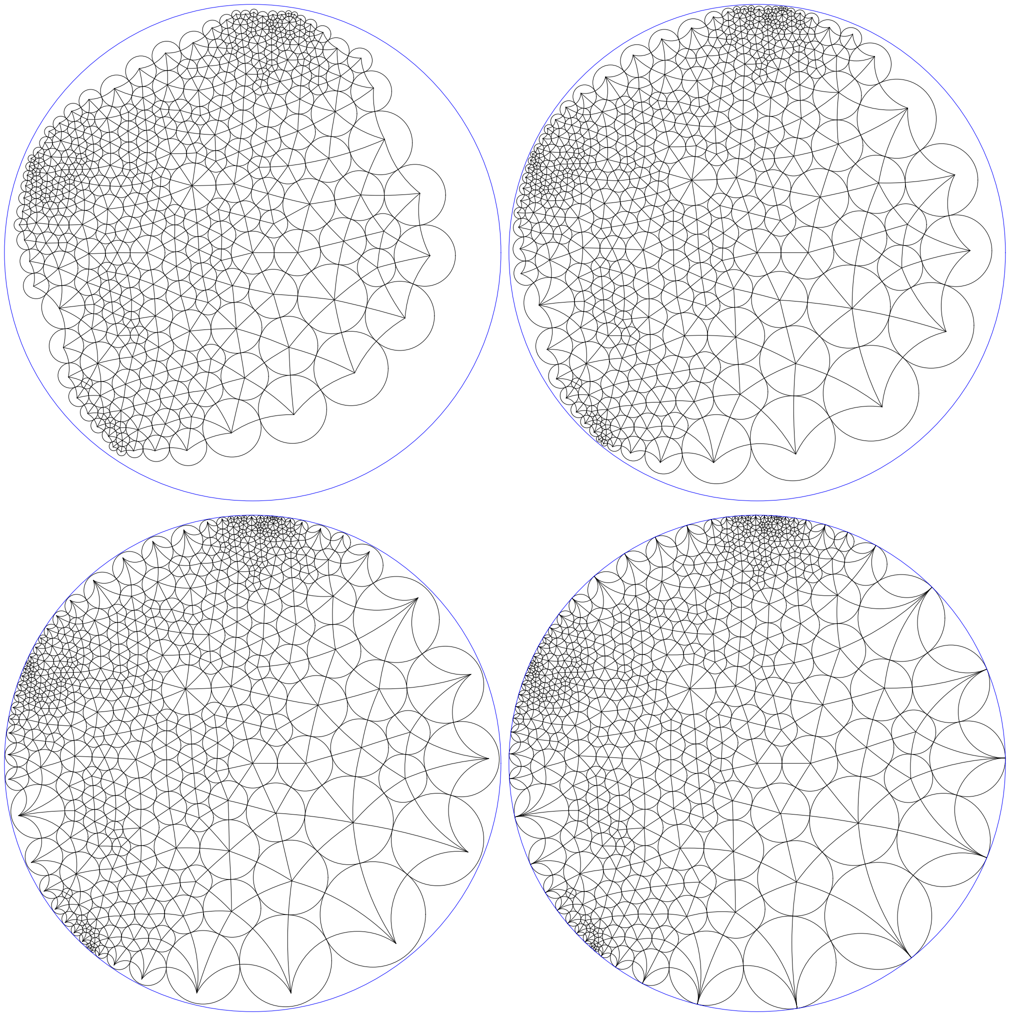

Figure 3.16: Hyperbolic Ricci flow for Riemann mapping

and

$$\begin{aligned}\frac{\partial\theta_1}{\partial u_1} &= -\frac{1}{A}\left(\frac{C_1C_2-C_3}{C_2+1}+\frac{C_1C_3-C_2}{C_3+1}\right)\\ &= -\frac{2C_1C_2C_3-C_2^2-C_3^2+C_1C_2+C_1C_3-C_2-C_3}{A(C_2+1)(C_3+1)/2}.\end{aligned}$$

By symmetry, we obtain

$$\frac{\partial\theta_i}{\partial u_j}=\frac{\partial\theta_j}{\partial u_i}=\frac{C_i+C_j-C_k-1}{A(C_k+1)/2}$$

and

$$\frac{\partial\theta_i}{\partial u_i}=-\frac{2C_iC_jC_k-C_j^2-C_k^2+C_iC_j+C_iC_k-C_j-C_k}{A(C_j+1)(C_k+1)/2}.$$

Hyperbolic Ricci flow can also be applied for computing Riemann mapping. Set the target curvature to be zeros on the interior vertices, and the boundary circle radii goes to ∞, then the Ricci flow leads to the Riemann mapping as shown in Fig. 3.16.

Chapter 4

The Unified Discrete Ricci Flow

This chapter introduces the unified theoretic framework for discrete Surface Ricci Flow, including all the common schemes: Tangential Circle Packing, Thurston's Circle Packing, Inversive Distance Circle Packing and Discrete Yamabe Flow. Furthermore, this work also introduces a novel schemes, Virtual Radius Circle Packing and the Mixed Type schemes, under the unified framework. This work gives explicit geometric interpretation to the discrete Ricci energies for all the schemes with all back ground geometries, and the corresponding Hessian matrices.

The unified frame work deepens our understanding to the the discrete surface Ricci flow theory, and has inspired us to discover the new schemes, improved the flexibility and robustness of the algorithms, greatly simplified the implementation and improved the efficiency. Experimental results show the unified surface Ricci flow algorithms can handle general surfaces with different topologies, and is robust to meshes with different qualities, and is effective for solving real problems.

In the following, we will introduce 4.1 the unified framework for different schemes of discrete surface Ricci flow, which covers 18 schemes in total; section 4.2 explains the geometric interpretation of the Hessian matrix of discrete Ricci energy for all schemes with different background geometries; section 4.3 gives a geometric interpretation of Ricci energy; Experimental results are reported in section 4.4, different schemes are systematically compared. The work concludes in section 4.5

4.1 Unified Discrete Surface Ricci Flow

This section systematically introduces the unified framework for discrete surface Ricci flow. The whole theory is explained using the variational principle on discrete surfaces based on derivative cosine law [53]. The elementary concepts and some of schemes can be found in [52] and the chapter 4 in [76].

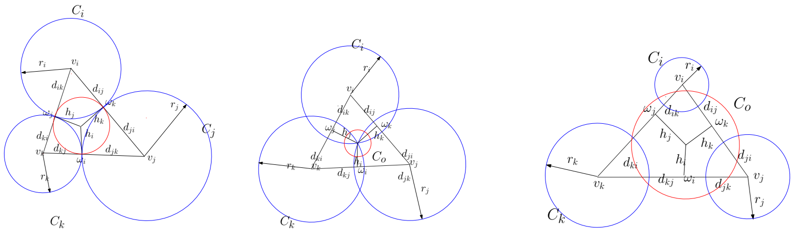

(a) tangential CP (b) Thurston's CP (c) Inversive distance CP

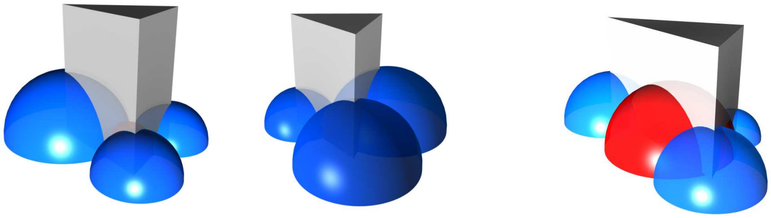

$\eta = 1, \varepsilon = 1$ $0 \leq \eta \leq 1, \varepsilon = 1$ $\eta \geq 1, \varepsilon = 1$

Figure 4.1: Tangential circle packing, Thurston's circle packing and inversive distance circle packing schemes, and the geometric interpretations to their Ricci energies.

4.1.1 Unified Circle Packing Metrics

Definition 28 (Circle Packing Metric)**.** *Suppose $\Sigma = (V,E,F)$ is a triangle mesh with spherical, Euclidean or hyperbolic background geometry. Each vertex v_i is associated with a circle with radius γ_i. The circle radius function is denoted as $\gamma : V \to \mathbb{R}_{>0}$; a function defined on the vertices $\varepsilon : V \to \{+1, 0, -1\}$ is called the* scheme coefficient; *a function defined on edges $\eta : E \to \mathbb{R}$ is called the* discrete conformal structure coefficient. *A circle packing metric is a 4-tuple $(\Sigma, \gamma, \eta, \varepsilon)$, the edge length is determined by the 4-tuple and the background geometry.*

In the smooth case, changing a Riemannian metric by a scalar function, $\mathbf{g} \to e^{2u}\mathbf{g}$, is called a conformal metric deformation. The discrete analogy to this is as follows.

Definition 29 (Discrete Conformal Equivalence)**.** *Two circle packing metrics $(\Sigma_k, \gamma_k, \eta_k, \varepsilon_k)$, $k = 1, 2$, are conformally equivalent if $\Sigma_1 = \Sigma_2$, $\eta_1 = \eta_2$, $\varepsilon_1 = \varepsilon_2$. ($\gamma_1$ may not equals to γ_2.)*

The discrete analogy to the concept of conformal factor in the smooth case is

Definition 30 (Discrete Conformal Factor)**.** *Discrete conformal factor for a circle packing metric $(\Sigma, \gamma, \eta, \varepsilon)$ is a function defined on each vertex $\mathbf{u} : V \to \mathbb{R}$,*

$$u_i = \begin{cases} \log \gamma_i & \mathbb{E}^2 \\ \log \tanh \frac{\gamma_i}{2} & \mathbb{H}^2 \\ \log \tan \frac{\gamma_i}{2} & \mathbb{S}^2 \end{cases} \tag{4.1.1}$$

Definition 31 (Circle Packing Schemes)**.** *Suppose $\Sigma = (V,E,F)$ is triangle mesh with spherical, Euclidean or hyperbolic background geometry. Given a circle packing metric $(\Sigma, \gamma, \eta, \varepsilon)$, for an*

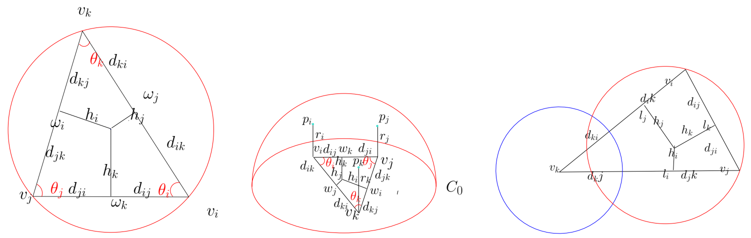

(d) Yamabe flow (e) virt.rad.cp (f) mixed type

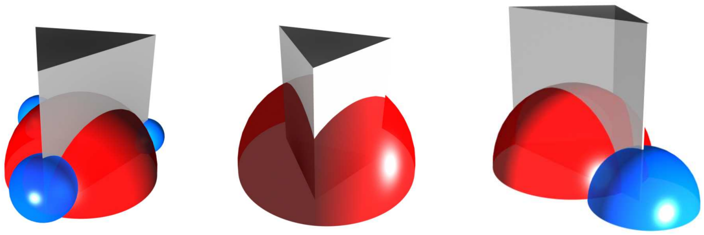

$\eta > 0, \varepsilon = 0$ $\eta > 0, \varepsilon = -1$ $\eta > 0$ $\varepsilon \in \{+1, 0, -1\}$

Figure 4.2: Yamabe flow, virtual radius circle packing and mixed type schemes, and the geometric interpretations to their Ricci energies.

edge $[v_i, v_j] \in E$*, its length* l_{ij} *is given by*

$$\begin{cases} l_{ij}^2 & = & 2\eta_{ij}e^{u_i+u_j} + \varepsilon_i e^{2u_i} + \varepsilon_j e^{2u_j} & \mathbb{E}^2 \\ \cosh l_{ij} & = & \frac{4\eta_{ij}e^{u_i+u_j}+(1+\varepsilon_i e^{2u_i})(1+\varepsilon_j e^{2u_j})}{(1-\varepsilon_i e^{2u_i})(1-\varepsilon_j e^{2u_j})} & \mathbb{H}^2 \\ \cos l_{ij} & = & \frac{-4\eta_{ij}e^{u_i+u_j}+(1-\varepsilon_i e^{2u_i})(1-\varepsilon_j e^{2u_j})}{(1+\varepsilon_i e^{2u_i})(1+\varepsilon_j e^{2u_j})} & \mathbb{S}^2 \end{cases} \tag{4.1.2}$$

The schemes are named as follows:

Scheme	ε_i	ε_j	η_{ij}
Tangential Circle Packing	*+1*	*+1*	*+1*
Thurston's Circle Packing	*+1*	*+1*	$[0,1]$
Inversive Distance Circle Packing	*+1*	*+1*	>0
Yamabe Flow	*0*	*0*	>0
Virtual Radius Circle Packing	*-1*	*-1*	>0
Mixed type	$\{-1,0,+1\}$	$\{-1,0,+1\}$	>0

Fig. 4.1 and Fig. 4.2 illustrate all the schemes with for discrete surfaces with Euclidean background geometry.

Remark 1. *From the definition, the tangential circle packing is a special case of Thurston's circle packing; Thurston's circle packing is a special case of inversive distance circle packing. In the following discussion, we unify all three types as inversive distance circle packing.*

4.1.2 Discrete Surface Ricci Flow

Definition 32 (Discrete Surface Ricci Flow)**.** *A discrete surface with $\mathbb{S}^2$, $\mathbb{E}^2$ or $\mathbb{H}^2$ background geometry, and a circle packing metric $(\Sigma, \gamma, \eta, \varepsilon)$, the discrete surface Ricci flow is*

$$\frac{du_i(t)}{dt} = \bar{K}_i - K_i(t), \tag{4.1.3}$$

where $\bar{K}_i$ is the target curvature at the vertex v_i.

The target curvature must satisfy certain constraints to ensure the existence of the solution to the flow, such as Gauss-Bonnet equation Eqn. 3.1.1, but also some additional ones described in [70], [57] and [15], for instances.

The discrete surface Ricci flow has exactly the same formula as the smooth counter part Eqn. 2.4.1. Furthermore, similar to the smooth case, discrete surface Ricci flow is also variational: the discrete Ricci flow is the negative gradient flow of the discrete Ricci energy.

Definition 33 (Discrete Ricci Energy)**.** *A discrete surface with $\mathbb{S}^2$, $\mathbb{E}^2$ or $\mathbb{H}^2$ background geometry, and a circle packing metric $(\Sigma, \gamma, \eta, \varepsilon)$. For a triangle $[v_i, v_j, v_k]$ with inner angles $(\theta_i, \theta_j, \theta_k)$, the discrete Ricci energy on the face is given by*

$$E_f(u_i, u_j, u_k) = \int^{(u_i, u_j, u_k)} \theta_i du_i + \theta_j du_j + \theta_k du_k. \tag{4.1.4}$$

The discrete Ricci energy for the whole mesh is defined as

$$E_\Sigma(u_1, u_2, \cdots, u_n) = \int^{(u_1, u_2, \cdots, u_n)} \sum_{i=1}^{n} (\bar{K}_i - K_i) du_i.. \tag{4.1.5}$$

From definition, we get the relation between the surface Ricci energy and the face Ricci energy

$$E_\Sigma = \sum_{i=1}^{n} (\bar{K}_i - 2\pi) u_i + \sum_{f \in F} E_f. \tag{4.1.6}$$

The description of the energy in terms of an integral requires the fact that the inside is a closed form so that it is defined independent of the integration path. This follows from the following symmetry lemma, which has fundamental importance. In this work, we give three proofs. The following one is algebraic, more difficult to verify, but leads to computational algorithm directly. The second one is based on the geometric interpretation to the Hessian matrix in Section 4.2. The third one is based on the geometric interpretation to the discrete Ricci energy. The later two proofs are more geometric and intuitive.

Lemma 18 (Symmetry)**.** *A discrete surface with $\mathbb{S}^2$, $\mathbb{E}^2$ or $\mathbb{H}^2$ background geometry, and a circle packing metric $(\Sigma, \gamma, \eta, \varepsilon)$, then for any pair of vertices v_i and v_j:*

$$\frac{\partial K_i}{\partial u_j} = \frac{\partial K_j}{\partial u_i}. \tag{4.1.7}$$

Proof. From the relation in Eqn. 4.1.6, it is sufficient and necessary to show the symmetry for each triangle $[v_i, v_j, v_k]$ for all schemes,

$$\frac{\partial \theta_i}{\partial u_j} = \frac{\partial \theta_j}{\partial u_i}.$$

This is proven by finding the explicit formula for the Hessain matrix of the face Ricci energy,

$$\frac{\partial(\theta_i, \theta_j, \theta_k)}{\partial(u_i, u_j, u_k)} = -\frac{1}{2A} L \Theta L^{-1} D, \tag{4.1.8}$$

where

$$A = \frac{1}{2} \sin \theta_i s(l_j) s(l_k) \tag{4.1.9}$$

the matrix L

$$L = \begin{pmatrix} s(l_i) & 0 & 0 \\ 0 & s(l_j) & 0 \\ 0 & 0 & s(l_k) \end{pmatrix} \tag{4.1.10}$$

and the matrix Θ

$$\Theta = \begin{pmatrix} -1 & \cos\theta_k & \cos\theta_j \\ \cos\theta_k & -1 & \cos\theta_i \\ \cos\theta_j & \cos\theta_i & -1 \end{pmatrix} \tag{4.1.11}$$

and

$$D = \begin{pmatrix} 0 & \tau(i,j,k) & \tau(i,k,j) \\ \tau(j,i,k) & 0 & \tau(j,k,i) \\ \tau(k,i,j) & \tau(k,j,i) & 0 \end{pmatrix} \tag{4.1.12}$$

where $s(x)$ and $\tau(i,j,k)$ are defined as

	$s(x)$	$\tau(i,j,k)$
$\mathbb{E}^2$	x	$1/2(l_i^2 + \varepsilon_j r_j^2 - \varepsilon_k r_k^2)$
$\mathbb{H}^2$	$\sinh x$	$\cosh l_i \cosh^{\varepsilon_j} r_j - \cosh^{\varepsilon_k} r_k$
$\mathbb{S}^2$	$\sin x$	$\cos l_i \cos^{\varepsilon_j} r_j - \cos^{\varepsilon_k} r_k$

By symbolic computation, it is straightforward to verify the symmetry of Eqn. 7.4.4. □

4.2 Geometric interpretation to Hessian

This section focuses on the geometric interpretation to Hessian matrix of the discrete Ricci energy on each face for $\mathbb{E}^2, \mathbb{H}^2$ and $\mathbb{S}^2$ cases. This gives the second proof of the symmetry lemma 18.

4.2.1 Euclidean Case

The interpretation in Euclidean case is due to Glickenstein [29] (Z. He [75] in the case of circle packings) and illustrated in [76]. In the current work, we build the connection to the Power Delaunay triangulation and power voronoi diagram.

We only focus on one triangle $[v_i, v_j, v_k]$, with corner angles $\theta_i, \theta_j, \theta_k$, conformal factors u_i, u_j, u_k and edge lengths l_{ij} for edge $[v_i, v_j]$, l_{jk} for $[v_j, v_k]$ and l_{ki} for $[v_k, v_i]$.

Power Delaunay Triangulation As shown in Fig. 4.1 and Fig. 4.2, the *power* of q with respect to v_i is

$$pow(v_i, q) = |v_i - q|^2 - \varepsilon\gamma_i^2.$$

The *power center* o of the triangle satisifies

$$pow(v_i, o) = pow(v_j, o) = pow(v_k, o).$$

The *power circle* C centered at o with radius γ, where $\gamma = pow(v_i, o)$.

Therefore, for tangential, Thurton's and inversive distance circle packing cases, the power circle is orthogonal to three circles at the vertices C_i, C_j and C_k; for Yamabe flow case, the power circle is the circumcircle of the triangle; for virtual radius circle packing, the power circle is the equator of the sphere, which goes through three points $\{v_i + \gamma_i\mathbf{n}, v_j + \gamma_j\mathbf{n}, v_k + \gamma_k\mathbf{n}\}$, where $\mathbf{n}$ is the normal to the plane.

Through the power center, we draw line perpendicular to three edges, the perpendicular feets are w_i, w_j and w_k respectively. The distance from the power center to the perpendicular feet are h_i, h_j and h_k respectively. Then it can be shown easily that

$$\frac{\partial\theta_i}{\partial u_j} = \frac{\partial\theta_j}{\partial u_i} = \frac{h_k}{l_k}, \frac{\partial\theta_j}{\partial u_k} = \frac{\partial\theta_k}{\partial u_j} = \frac{h_i}{l_i}, \frac{\partial\theta_k}{\partial u_i} = \frac{\partial\theta_i}{\partial u_k} = \frac{h_j}{l_j}, \tag{4.2.1}$$

furthermore,

$$\frac{\partial\theta_i}{\partial u_i} = -\frac{h_k}{l_k} - \frac{h_j}{l_j}, \frac{\partial\theta_j}{\partial u_j} = -\frac{h_k}{l_k} - \frac{h_i}{l_i}, \frac{\partial\theta_k}{\partial u_k} = -\frac{h_i}{l_i} - \frac{h_j}{l_j}. \tag{4.2.2}$$

These two formula induces the formula for the Hessian of the Ricci energy of the whole surface. One can treat the circle packing $(\Sigma, \gamma, \eta, \varepsilon)$ as a power triangulation, which has a dual power diagram $\bar{\Sigma}$. Each edge $e_{ij} \in \Sigma$ has a dual edge $\bar{e} \in \bar{\Sigma}$, then

$$\frac{\partial K_i}{\partial u_j} = \frac{\partial K_j}{\partial u_i} = \frac{|\bar{e}_{ij}|}{|e_{ij}|}, \tag{4.2.3}$$

and

$$\frac{\partial K_i}{\partial u_i} = -\sum_j \frac{\partial K_i}{\partial u_j}. \tag{4.2.4}$$

This gives a geometric proof for the symmetry lemma 18 in Euclidean case.

Suppose on the edge $[v_i, v_j]$, the distance from v_i to the perpendicular foot w_k is d_{ij}, the distance from v_j to w_k is d_{ji}, then $l_{ij} = d_{ij} + d_{ji}$, and

$$\frac{\partial l_{ij}}{\partial u_i} = d_{ij}, \frac{\partial l_{ij}}{\partial u_j} = d_{ji},$$

furthermore

$$d_{ij}^2 + d_{jk}^2 + d_{ki}^2 = d_{ik}^2 + d_{kj}^2 + d_{ji}^2.$$

This shows the power circle interpretation is equivalent to Glikenstain's formulation.

4.2.2 Hyperbolic Case

Let $\triangle_{123}$ be a hyperbolic triangle whose vertices are labeled by $1,2,3$. Let r_1,r_2,r_3 be three positive numbers associated to the vertices, and $\varepsilon_1,\varepsilon_2,\varepsilon_3 \in \{-1,0,1\}$ be indicators of the type of the vertices.

For the mixed type of discrete conformal geometry, the edge length of $\triangle_{123}$ is given by

$$\cosh l_k = 4\eta_{ij}\frac{\sinh r_i}{(1-\varepsilon_i)\cosh r_i + 1 + \varepsilon_i}\frac{\sinh r_j}{(1-\varepsilon_j)\cosh r_j + 1 + \varepsilon_j} + \cosh^{\varepsilon_i} r_i \cosh^{\varepsilon_j} r_j,$$

where $\{i,j,k\} = 1,2,3$.

Via the cosine law, the edge lengths l_1,l_2,l_3 determine the angles $\theta_1,\theta_2,\theta_3$.

When $\varepsilon_1 = \varepsilon_2 = \varepsilon_3 = 0$, this is the case of Yamabe flow. There is a circle passing through the three vertices of $\triangle_{123}$. It is still called the *power circle*.

When $\varepsilon_1 = \varepsilon_2 = \varepsilon_3 = 1$, this is the case of inversive distance circle packing. Centered at each vertex i, there is a circle with radius r_i. Then there is the *power circle* orthogonal to the three circles centered at the vertices.

When $\varepsilon_1 = \varepsilon_2 = \varepsilon_3 = -1$, this is the case of virtual radius circle packing. Let $\triangle_{123}$ be on the equator plane of the ball model of the hyperbolic space $\mathbb{H}^3$. For each vertex i, let ii' be the geodesic arc perpendicular to the equator plane with length r_i. Assume $1',2',3'$ are above the equator plane. There is a hemisphere passing through $1',2',3'$ and orthogonal to the equator plane. The *power circle* in this case is the intersection of the hemisphere and the equator plane.

For a mix type, the power circle can still be defined.

For any type, let h_i be the distance from the center of the power circle to the edge ij whose length is l_k.

Theorem 17. *Let*

$$e^{u_i} = \frac{e^{r_i}-1}{e^{r_i}+1} = \tanh\frac{r_i}{2}.$$

Then

$$\frac{\partial\theta_1}{\partial u_2} = \frac{\partial\theta_2}{\partial u_1}$$

which equal to

$$\frac{\tanh h_3}{\sinh^2 l_3}\sqrt{2\cosh^{\varepsilon_1} r_1 \cosh^{\varepsilon_2} r_2 \cosh l_3 - \cosh^{2\varepsilon_1} r_1 - \cosh^{2\varepsilon_2} r_2}.$$

This gives a geometric proof for the symmetry lemma 18 in hyperbolic case.

We only need to prove the theorem for the case of $\varepsilon_1 = \varepsilon_2 = \varepsilon_3 = 1$. General case can be proved similarly.

Proof. **Step 1**. Denote the center of the power circle by o, the radius by r. Let x,y,z be the distance from o to the vertices $1,2,3$. Then

$$\begin{aligned}\cosh x &= \cosh r \cosh r_1\\ \cosh y &= \cosh r \cosh r_2\\ \cosh z &= \cosh r \cosh r_3\end{aligned} \tag{4.2.5}$$

Let α be the angle $\angle 13o$ and β the angle $\angle 23o$. Then $\alpha+\beta=\theta_3$. Therefore

$$1+2\cos\alpha\cos\beta\cos\theta_3=\cos^2\alpha+\cos^2\beta+\cos^2\theta_3. \tag{4.2.6}$$

By the cosine law,

$$\cos\alpha=\frac{-\cosh x+\cosh z\cosh l_2}{\sinh z\sinh l_2},$$
$$\cos\beta=\frac{-\cosh y+\cosh z\cosh l_1}{\sinh z\sinh l_1},$$
$$\cos\theta_3=\frac{-\cosh l_3+\cosh l_1\cosh l_2}{\sinh l_1\sinh l_2}.$$

Substituting the three formulas into the equation (4.2.6), we obtain a relation between the 6 numbers l_1,l_2,l_3,x,y,z.

Substituting the equations (4.2.5) into this relation, we obtain a relation between l_1,l_2,l_3,r_1,r_2,r_3 and r.

Solving for r, we get $\cosh^2 r=\frac{\mathscr{N}}{\mathscr{D}}$, where

$$\mathscr{N}=1+2\cosh l_1\cosh l_2\cosh l_3-\cosh^2 l_1-\cosh^2 l_2-\cosh^2 l_3,$$

$$\begin{aligned}\mathscr{D}=&\cosh^2 r_1(1-\cosh^2 l_1)+2\cosh r_2\cosh r_3(\cosh l_2\cosh l_3-\cosh l_1)\\&+\cosh^2 r_2(1-\cosh^2 l_2)+2\cosh r_3\cosh r_1(\cosh l_3\cosh l_1-\cosh l_2)\\&+\cosh^2 r_3(1-\cosh^2 l_3)+2\cosh r_1\cosh r_2(\cosh l_1\cosh l_2-\cosh l_3).\end{aligned}$$

Step 2. Since h_3 is the height of the triangle $\triangle_{o12}$ with bottom the edge 12. By the standard formula of height of a hyperbolic triangle, we have

$$\sinh^2 h_3=\frac{1+2\cosh x\cosh y\cosh l_3-\cosh^2 x-\cosh^2 y-\cosh^2 l_3}{\sinh^2 l_3}.$$

After substituting the equations (4.2.5) into the above formula, we have

$$\tanh^2 h_3=\frac{\cosh^2 r(2\cosh r_1\cosh r_2\cosh l_3-\cosh^2 r_1-\cosh^2 r_2)-\sinh^2 l_3}{\cosh^2 r(2\cosh r_1\cosh r_2\cosh l_3-\cosh^2 r_1-\cosh^2 r_2)}.$$

After substituting the equation $\cosh^2 r=\frac{\mathscr{N}}{\mathscr{D}}$, we have

$$\tanh^2 h_3=\frac{\mathscr{N}(2\cosh r_1\cosh r_2\cosh l_3-\cosh^2 r_1-\cosh^2 r_2)-\mathscr{D}\sinh^2 l_3}{\mathscr{N}(2\cosh r_1\cosh r_2\cosh l_3-\cosh^2 r_1-\cosh^2 r_2)}.$$

After substituting the expressions of $\mathscr{N}$ and $\mathscr{D}$ in step 1, we have

$$\tanh^2 h_3=$$
$$\frac{[(\cosh l_1\cosh l_3-\cosh l_2)\cosh r_1+(\cosh l_2\cosh l_3-\cosh l_1)\cosh r_2-\sinh^2 l_3\cosh r_3]^2}{\mathscr{N}(2\cosh r_1\cosh r_2\cosh l_3-\cosh^2 r_1-\cosh^2 r_2)}.$$

Step 3. By direct calculation, we have

$$\begin{aligned}&\frac{\partial\theta_1}{\partial u_2}=\frac{\partial\theta_2}{\partial u_1}=\frac{-1}{\sin\theta_i\sinh l_j\sinh l_k}\\&(\cosh r_3-\frac{\cosh l_1\cosh l_3-\cosh l_2}{\sinh^2 l_3}\cosh r_1-\frac{\cosh l_2\cosh l_3-\cosh l_1}{\sinh^2 l_3}\cosh r_2)=\\&\frac{(\cosh l_1\cosh l_3-\cosh l_2)\cosh r_1+(\cosh l_2\cosh l_3-\cosh l_1)\cosh r_2-\sinh^2 l_3\cosh r_3}{\sqrt{\mathcal{N}}\cdot\sinh^2 l_3}.\end{aligned}$$

Comparing with the last formula of step 2, we have

$$\frac{\partial\theta_1}{\partial u_2}=\frac{\partial\theta_2}{\partial u_1}=\frac{\tanh h_3}{\sinh^2 l_3}\sqrt{2\cosh r_1\cosh r_2\cosh l_3-\cosh^2 r_1-\cosh^2 r_2}.$$

□

4.2.3 Spherical Case

According to a general principle of the relation of hyperbolic geometry and spherical geometry, to obtain a formula in spherical geometry, we only need to replace sinh and cosh in hyperbolic geometry by $\sqrt{-1}\sin$ and $\cos$.

For the mixed type of discrete conformal geometry with spherical background geometry, the edge length of $\triangle_{123}$ is given by

$$\begin{aligned}&\cosh l_{ij}=\\&-4\eta_{ij}\frac{\sin r_i}{(1-\varepsilon_i)\cos r_i+1+\varepsilon_i}\frac{\sin r_j}{(1-\varepsilon_j)\cos r_j+1+\varepsilon_j}+\cos^{\varepsilon_i}r_i\cos^{\varepsilon_j}r_j.\end{aligned}$$

Via the cosine law, the edge lengths l_1,l_2,l_3 determine the angles $\theta_1,\theta_2,\theta_3$.

We can define power circles similarly. Let h_i be the distance from the center of the power circle to the edge ij whose length is l_k.

Theorem 18. *Let*

$$e^{u_i}=\tan\frac{r_i}{2}.$$

Then

$$\frac{\partial\theta_1}{\partial u_2}=\frac{\partial\theta_2}{\partial u_1}$$

which equal to

$$\frac{\tan h_3}{\sin^2 l_3}\sqrt{-2\cos^{\varepsilon_1}r_1\cos^{\varepsilon_2}r_2\cos l_3+\cos^{2\varepsilon_1}r_1+\cos^{2\varepsilon_2}r_2}.$$

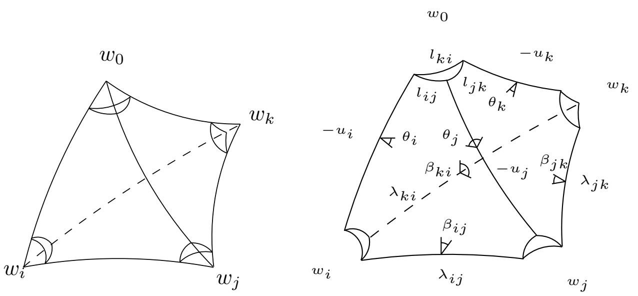

Figure 4.3: Generalized hyperbolic tetrahedron.

This gives a geometric proof for the symmetry lemma 18 in spherical case.

This theorem is also proved by using the general principle: replace sinh and cosh in hyperbolic geometry by $\sqrt{-1}$ sin and cos.

Here we can give the second proof for the symmetry lemma 18 based on the geometric interpretation to the Hessian, which is geometric and intuitive.

Proof. Formula 4.2.1 show the symmetry for all schemes with Euclidean background geometry; theorem 17 proves the symmetry for the hyperbolic cases; theorem 18 for the spherical cases. □

4.3 Geometric Interpretations to Ricci Energies

The geometric interpretation to Ricci energies of Euclidean and hyperbolic Yamabe schemes were discovered by Bobenko, Pinkall and Springborn in [9]. The interpretation to Ricci energies of Euclidean schemes (without the mixed type) are illustrated in [76]. In the current work, we generalize the geometric interpretations to all the schemes in all background geometries covered by the unified framework, as shown in Fig. B.1.

We use the upper half space model for $\mathbb{H}^3$, with Riemannian metric

$$ds^2 = \frac{dx^2 + dy^2 + dz^2}{z^2}$$

the xy-plane is the ideal boundary. Consider a triangle $[v_i, v_j, v_k]$, its Ricci energy is closely related to the volume of a generalized hyperbolic tetrahedron whose vertices can be in $\mathbb{H}^3$, truncated by a horosphere or truncated by a hyperbolic plane.

In Fig. 4.3, the generalized hyperbolic tetrahedron has 4 vertices w_0, w_i, w_j, w_k. The tetrahedron vertex w_0 is called the *top vertex*. The 4 faces of the tetrahedron are hyperbolic planes, the 6 edges are geodesics. The 6 edge lengths of the generalized tetrahedron are $-u_i, -u_j, -u_k$ and $\lambda_{ij}, \lambda_{jk}, \lambda_{ki}$. The generalized tetrahedron is uniquely determined by these 6 edge lengths.

The followings are the common principles for constructing the generalized tetrahedron for all the schemes,

1. For all $\mathbb{E}^2$ schemes, the top vertex w_0 is ideal (at infinity) and truncated by a horosphere; for all $\mathbb{H}^2$ schemes, the top vertex is hyperideal (exceeding the boundary of $\mathbb{H}^3$) and truncated by a hyperbolic plane; for all $\mathbb{S}^2$ schemes, the top vertex is in $\mathbb{H}^3$.

2. For w_i, if the corresponding vertex v_i is of inversive distance circle packing $\varepsilon_i = +1$, then it is hyperideal and truncated by a hyperbolic plane; if v_i is of Yamabe flow $\varepsilon_i = 0$, then it is ideal and truncated by a horosphere; if v_i is virtual radius circle packing $\varepsilon_1 = -1$, then it is in $\mathbb{H}^3$. Same results holds for w_j and w_k.
3. The edges on the truncated tetrahedron, connecting to the top vertex on the original tetrahedron, have lengths $-u_i$, $-u_j$ and $-u_k$ respectively.
4. For the edge lengths λ_{ij}, there is a unified formula for three geometries: Euclidean, hyperbolic, spherical,
$$\eta_{ij} = \frac{1}{2}(e^{\lambda_{ij}} + \varepsilon_i\varepsilon_j e^{-\lambda_{ij}}). \tag{4.3.1}$$

The triangle associated to the top vertex w_0 is the triangle $[v_i, v_j, v_k]$. It is obtained by truncating by a horosphere, truncating by a hyperbolic plane or intersecting with a sphere. Given $-u_i, -u_j, -u_k, \eta_{ij}, \eta_{jk}, \eta_{ki}$, using cosine law, we can calculate the edge lengths of the triangle $[v_i, v_j, v_k]$. They are exactly given by the formula Eqn. 4.1.2. That means the triangle $[v_i, v_j, v_k]$ has lengths l_{ij}, l_{jk}, l_{ki} and angles $\theta_i, \theta_j, \theta_k$.

Here we can give the third proof for the symmetry lemma based on the geometric interpretation to the Ricci energy, which is more geometric, intuitive and much easier to verify.

Proof. As shown in Fig. 4.3, for a generalized hyperbolic tetrahedron, the 4 vertices can have any types. The 3 vertical edges have lengths $-u_i, -u_j, -u_k$ with dihedral angles $\theta_i, \theta_j, \theta_k$. The bottom edges have lengths $\lambda_{ij}, \lambda_{jk}, \lambda_{ki}$ with dihedral angles $\beta_{ij}, \beta_{jk}, \beta_{ki}$.

Let V be the volume of the generalized hyperbolic tetrahedron. By Schläfli formula

$$dV = -\frac{1}{2}\left(-u_i d\theta_i - u_j d\theta_j - u_k d\theta_k + \lambda_{ij} d\beta_{ij} + \lambda_{jk} d\beta_{jk} + \lambda_{ki} d\beta_{ki}\right) \tag{4.3.2}$$

During the Ricci flow, the conformal structure coefficients $\eta_{ij}, \eta_{jk}, \eta_{ki}$ are invariant, so $\lambda_{ij}, \lambda_{jk}, \lambda_{ki}$ are fixed. Because the generalized tetrahedron is determined by the edge lengths $-u_i, -u_j, -u_k, \lambda_{ij}, \lambda_{jk}, \lambda_{ki}$, during the flow, all dihedral angles $\theta_i, \theta_j, \theta_k, \beta_{ij}, \beta_{jk}, \beta_{ki}$ are functions of u_i, u_j, u_k, the volume V is also the function of u_i, u_j, u_k.

Consider the function,

$$W(u_i, u_j, u_k) = u_i\theta_i + u_j\theta_j + u_k\theta_k - \lambda_{ij}\beta_{ij} - \lambda_{jk}\beta_{jk} - \lambda_{ki}\beta_{ki} - 2V \tag{4.3.3}$$

hence,

$$\begin{aligned} dW &= \theta_i du_i + \theta_j du_j + \theta_k du_k \\ &\quad + u_i d\theta_i + u_j d\theta_j + u_k d\theta_k - \lambda_{ij} d\beta_{ij} - \lambda_{jk} d\beta_{jk} - \lambda_{ki} d\theta_{ki} \\ &\quad -2dV \end{aligned}$$

substitute Schläfli formula Eqn. 4.3.2, we have

$$dW = \theta_i du_i + \theta_j du_j + \theta_k du_k$$

therefore

$$W = \int \theta_i du_i + \theta_j du_j + \theta_k du_k + c.$$

W in fact, is the discrete Ricci energy on face in Eqn. 4.1.4. This shows the differential 1-form

$$\theta_i du_i + \theta_j du_j + \theta_k du_k \tag{4.3.4}$$

is exact, therefore closed. Namely, the Hessian matrix

$$\frac{\partial(\theta_i, \theta_j, \theta_k)}{\partial(u_i, u_j, u_k)}$$

is symmetric. □

The formula Eqn. 4.3.3 represents the Ricci energy on a face as the volume of the generalized hyperbolic tetrahedron with other terms of conformal factors and conformal structure coefficients. This formula was introduced first by Bobenko, Pinkall and Springborn in [9] for Euclidean and hyperbolic Yamabe flow. In the current work, we generalize it to all 18 schemes. The differential in Eqn. 4.3.4 is independent of the choice of horospheres, since the Schläfli formula is independent of the choice of horospher for an ideal vertex.

4.4 Experimental Results

In this section, we report our experimental results based on unified Ricci flow. We thoroughly compare different schemes in terms of robustness, conformality, efficiency and initialization difficulty.

4.4.1 Experimental Environment

We implemented the unified Ricci flow algorithms using generic C++ language on Windows platform. The method is based on optimizing the convex energy using Newton's method. The sparse linear systems are solved using Eigen library [33]. The mesh representation is based on dynamic halfedge data structure. The current implementation covers all schemes: tangential circle packing, Thurston's circle packing, inversive distance circle packing, Yamabe flow, virtual radius circle packing and mixed type schemes, for discrete surfaces with Euclidean and hyperbolic background geometries. The algorithms can handle surfaces different topologies. The package is accessible for the whole research community.

The computational time is tested on the desktop with 2.00GHz CPU, 3.00G RAM. The geometric data sets are from the public databases, such as [1] and [2]. The human face surfaces were scanned from a high speed and high resolution, phase shifting scanner, as described in [74]. We tested our algorithm on a huge amount of various models, including different sizes and topology types. Some of them are without any refinement or geometric processing, in order to test the robustness of the algorithms. Some of them are re-meshed using the algorithm in [38].

4.4.2 Generality Testing

Fig. 1.1 and 1.2 demonstrate the generality of Ricci flow method to handle surfaces with all possible topologies. Fig. 1.1 shows the uniformization for closed surfaces, where surfaces are conformally mapped to the unit sphere, Euclidean plane or the hyperbolic disk. Fig. 1.2 illustrates the

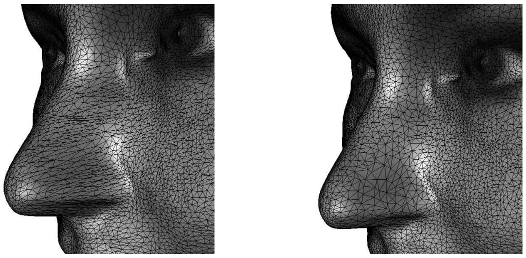

(a) low quality face (b) high quality face

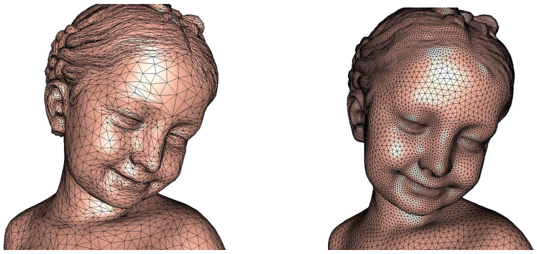

(c) low quality bimba (d)high quality bimba

Figure 4.4: Robustness testing.

uniformization for surfaces with boundaries, where compact surface with boundaries are mapped to constant curvature spaces, such that all boundaries are mapped to geodesic circles. Suggested by Glickenstein: Although there is not currently a robust theory of Ricci flow with boundary in the smooth setting, the discrete Ricci flow can compute the canonical conformal mapping with high efficacy and efficiency. These two figures cover all the topology types of compact surfaces.

The uniformization of the genus zero closed surface can be computed using Ricci flow with spherical background geometry, or Euclidean background geometry. The spherical Ricci energy is non-convex, therefore the spherical Ricci flow is not so stable as the Euclidean Ricci flow. For surface with multiple boundaries, we used Ricci flow method with Koebe's iteration [61].

4.4.3 Comparisons Among Schemes

In the following we compare different schemes of surface Ricci flow in details.

Robustness In practice, the biggest challenge for Ricci flow algorithm is the robustness. Given a target curvature $\bar{K}$, we need to ensure the following two points:

1. The target curvature is admissible, namely, the solution to the Ricci flow Eqn. 4.1.3 exists.
2. The solution is reachable. It is possible that the flow hits the boundary of the admissible curvature space before it hits the target curvature.

For Tangential circle packing, Thurston's circle packing, there are theorems describing the admissible curvature spaces [70] and [15]. For Euclidean (or hyperbolic) Yamabe flow, if the Delaunay condition is preserved during the flow by edge swapping, the admissible curvature space is given in the recent works [31] and [30].

We test robustness to the mesh qualities of different schemes. As shown in Fig. 4.4, the low quality meshes are simplified from the raw data, they have many obtuse angles and degenerated triangles; the high quality meshes are obtained using the method in [38]. We use different schemes to compute Riemann mappings. For surfaces with high mesh qualities, all schemes succeed with comparable running time. For surfaces with low mesh qualities, tangential circle packing outperforms all other schemes. The other schemes either crash in the flow process, or pass through with carefully chosen small step length, therefore, the running times are much longer.

If we allow the connectivity to be modified during the flow, to preserve the power Delaunay condition, then all schemes succeed on both surfaces. This shows the preserving the power Delaunay condition greatly improves the robustness of the Ricci flow algorithms.

Conformality Fig. 4.5 compares the qualities of different schemes: tangential circle packing, inversive distance circle packing, Yamabe flow and virtual radius circle packing. The parameterization is denoted as $\varphi : M \to \mathbb{R}^2$. We calculate each corner angle in the mesh before and after the discrete conformal mapping. Then we compute the ratio between two angle values, take the logarithm. The histogram of the logarithm of the angle ratios is a good measurement for the quality of the discrete conformal mapping. If the mapping has high conformality, then all angle ratios are close to 1, and the histogram is a delta function at 0. Otherwise, the histogram is with high standard deviation. From the histograms in Fig. 4.5, we can see the tangential circle packing produces mappings with lower conformity. The other three schemes produce mappings with similar conformality.

Convergence Rate Fig. 4.6 and table 4.1 show one experiment for comparing the convergence rates of different schemes on four different genus one surfaces. In the experiment, the curvature error threshold is set to $1e-6$ the step length in Newton's method is chosen to be $5e-1$. In the table 4.1, each item shows the running time in seconds, and iterations in the optimization. From the table, we can see the running time and iterations of different schemes are similar.

In practice, tangential circle packing is more robust to lower quality mesh qualities, the step length can be chosen to be larger, therefore, it converges faster than other schemes.

Initialization In practice, the discrete surfaces are given as triangular meshes, in the initialization stage, we need to convert the edge length function to circle packing metric $(\Sigma, \gamma, \eta, \varepsilon)$. For different schemes, this conversion has different level of difficulties.

For tangential circle packing and Yamabe flow, the initializations are easy and the resulting circle packing metrics are unique. The initialization is difficult for Thurston's circle packing, which requires the intersection angles between two vertex circles are acute, furthermore, the resulting conformal structure coefficient $\eta : E \to \mathbb{R}$ may not be unique. For inversive distance, virtual radius and mixed type schemes, the initializations are relatively easier, but the resulting circle packing metrics may not be unique.

In theory, the conformal structure coefficient η will affect the admissible curvature space [70] and [15]. In practice, we haven't found that different choices of η's make differences in terms of conformality or robustness.

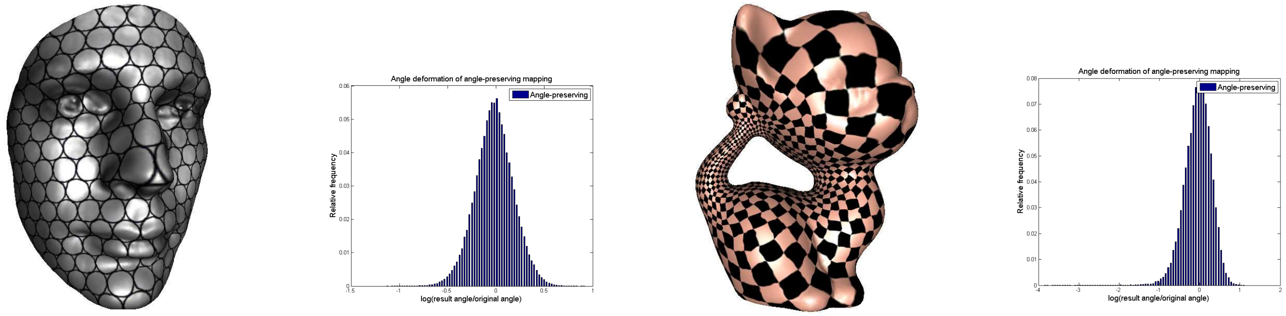

Tangential CP

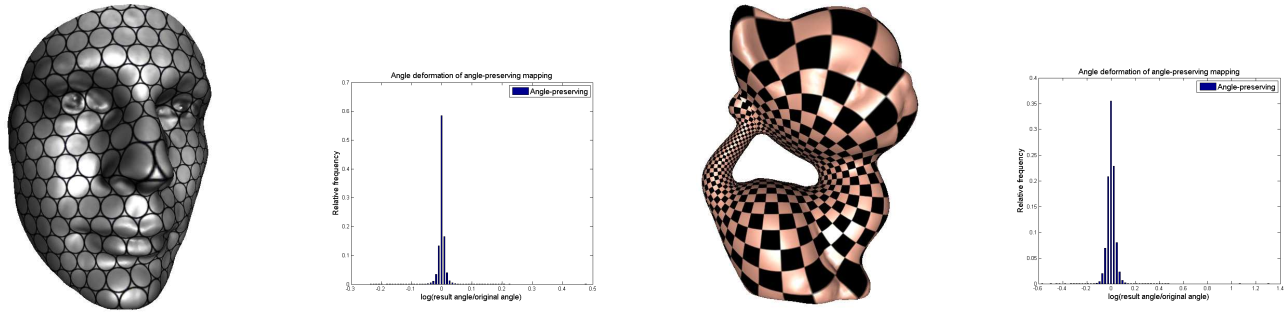

Inversive distance CP

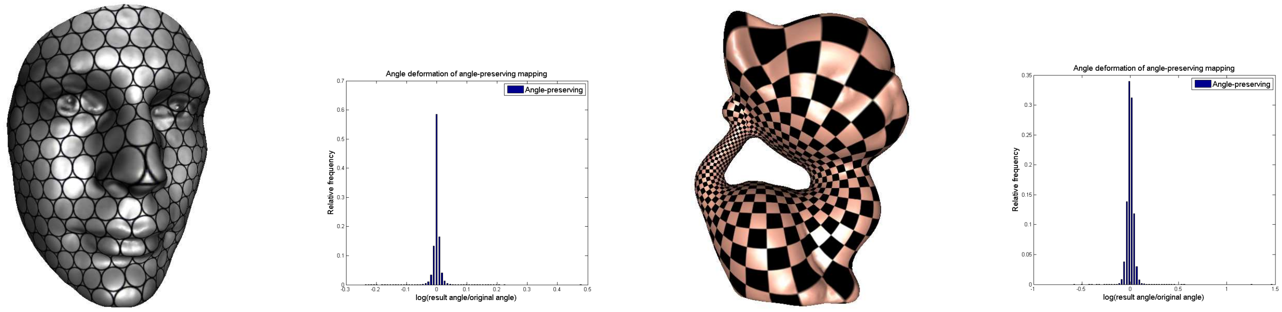

Yamabe flow

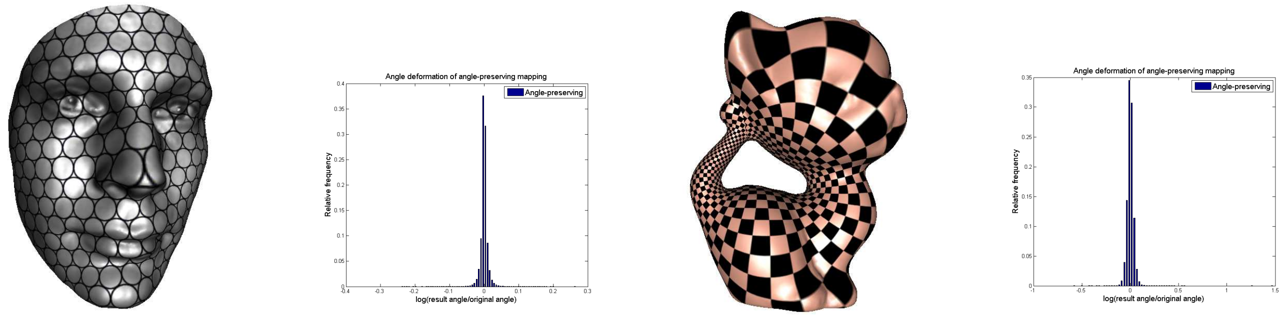

Virtual radius CP

Figure 4.5: Conformality test for different schemes. The face model is with high mesh quality, the kitten model is with lower mesh quality.

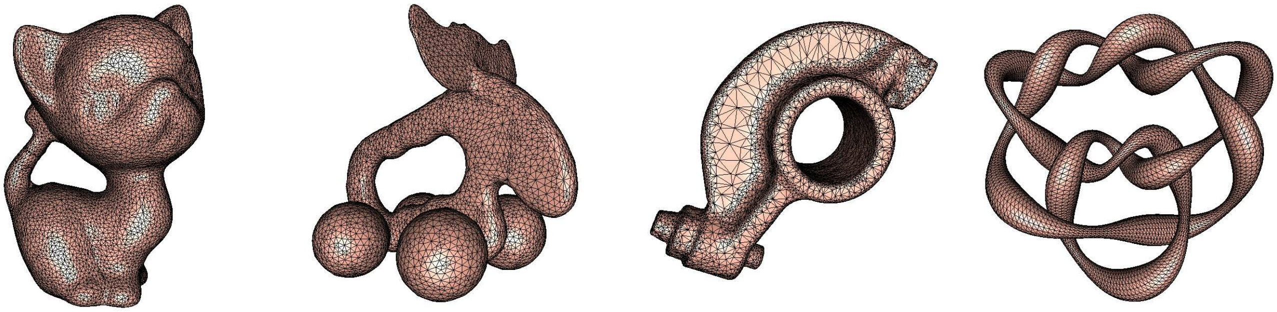

Figure 4.6: Convergence testing.

mesh	V/F/E	Tan. CP	Inv. Dist. CP	Yamabe Flow	Vir. Rad. CP
Knot	9792/19584/29376	2.324/18	2.314/17	2.223/17	2.234/17
Elk	9000/18000/27000	3.476/24	2.775/28	2.938/21	2.737/20
Rocker	10044/20088/30132	3.424/23	2.891/21	2.938/21	2.922/21
Kitten	10219/20438/30657	4.298/23	3.941/21	3.933/21	3.896/21

Table 4.1: Convergence test.

4.5 Conclusion

This Chapter establishes a unified framework for discrete surface Ricci flow, which covers most existing schemes: tangential circle packing, Thurston's circle packing, inversive distance circle packing, discrete Yamabe flow, virtual radius circle packing and mixed scheme, with Spherical, Euclidean and hyperbolic background geometry. The unified frameworks for hyperbolic and spherical schemes are introduced to the literature for the first time. For Euclidean schemes, our formulation is equivalent to Glickenstein's geometric construction.

Four newly discovered schemes are introduced, which are hyperbolic and Euclidean virtual radius circle packing and the mixed schemes.

This Chapter introduces a geometric interpretation to the Hessian of discrete Ricci energy for all schemes, which generalizes Glickenstein's formulation in Euclidean case.

This Chapter also gives explicit geometric interpretations to the discrete Ricci energy for all the schemes, which generalizes Bobenko, Pinkall and Springborn's construction [9] for Yamabe flow cases.

The unified frame work deepen our understanding to the the discrete surface Ricci flow theory, and inspired us to discover the novel schemes of virtual radius circle packing and the mixed scheme, improved the flexibility and robustness of the algorithms, greatly simplified the implementation and improved the efficiency.

Experimental results show the unified surface Ricci flow algorithms can handle surfaces with all possible topologies. We further compare different schemes in terms of conformality, robustness, convergence rate, and the difficulty level of construction.

Chapter 5

Visualization of 2-dimensional Ricci Flow

This Chapter aims at visualizing the abstract Ricci curvature flow partially using the recent work of Izmestiev [39]. The major challenges are to represent the intrinsic Riemannian metric of a surface by extrinsic embedding in the three dimensional Euclidean space and demonstrate the deformation process which preserves the conformal structure. A series of rigorous and practical algorithms are introduced to tackle the problem. First, the Ricci flow is discretized to be carried out on meshes. The preservation of the conformal structure is demonstrated using texture mapping. The curvature redistribution and flow pattern is depicted as vector fields and flow fields on the surface. The embedding of convex surfaces with prescribed Riemannian metrics is illustrated by embedding meshes with given edge lengths. Using the variational principle developed by Izemestiev, the embedding is realized by optimizing a special energy function, the unique optimum is the solution.

5.1 Visualization of Curvature Flow

During the Ricci flow, the curvatures in a given surface are redistributed driven by the metric deformation like a heat diffusion process. The curvature flow can be modeled as an electric network model.

Suppose the change of the curvature is $d\mathbf{k} = \bar{\mathbf{k}} - \mathbf{k}$, which is treated as the electric potential. The conductance of an edge e_{ij} is denoted by w_{ij}, which is defined as $w_{ij} = \frac{h_{ij}^k + h_{ji}^p}{l_{ij}}$, where l_{ij} is the edge length of e_{ij} under metric $\mathbf{u}$, h_{ij}^k, h_{ji}^p are the distances to e_{ij} of the circumcenters of the two faces adjacent to e_{ij}. Then the curvature flow along edge e_{ij} from v_i to v_j is

$$w_{ij} \nabla d\mathbf{k} = w_{ij}(dk_j - dk_i). \tag{5.1.1}$$

Curvature flow as a Heat Diffusion The curvature evolves like a heat diffusion, $\frac{d\mathbf{k}}{dt} = -\Delta(\mathbf{u})\mathbf{k}$, where $\Delta(\mathbf{u})$ is the discrete Laplace-Beltrami operator.The elements $\Delta_{ij} = w_{ij}, i \neq j$ if e_{ij} is an edge, otherwise Δ_{ij} is zero. $\Delta_{ii} = -\sum_{j \neq i} w_{ij}$.

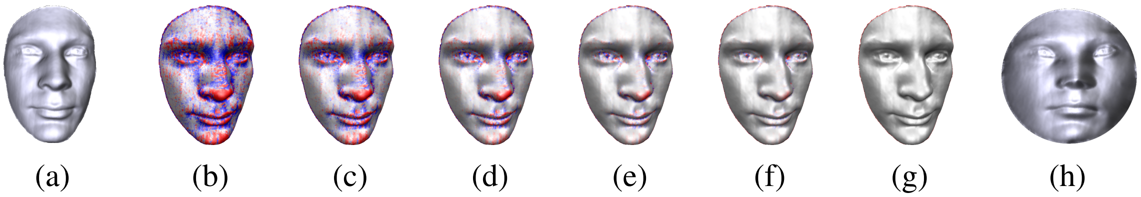
(a) (b) (c) (d) (e) (f) (g) (h)

Figure 5.1: (a): a face model, (b)-(g): the diffusion of curvatures during the Ricci flow process. The red, blue, and gray colors indicate high, low, and zero curvatures, respectively. (g): the face model with the deformed Riemannian metric from the Ricci flow, which can be flatten in to R^2.

The most simple way to visualize the behavior of the Ricci flow is the variation of the curvature values with a color spectrum during the process. Figure 5.1 illustrates the curvature evolutions in a face model with Ricci flow. We set the target curvature values for the face model such that $k_i \equiv 0$ for the interior vertices and $\sum k_i = 2\pi$ for the boundary vertices. As shown in Figure 5.1 (b)-(g), during the Ricci flow the high curvature values gradually decreased and the low curvature values gradually increased with the diffusions. Finally, the only boundary vertices have positive curvatures with the sum of 2π, and each interior vertex has the zero curvature (see Figure 5.1(g)). From the target Riemannian metric, we can embed the face model onto the unit disk as shown in Figure 5.1(h).

Curvature flow as the gradient field The more intuitive way is to visualize the streams of the curvature flows on the given mesh during the Ricci flow. From this, we can clearly see the fact that the curvature flows from one place to to another place. The network of the curvature flows can be easily computed using the formulae (5.1.1).

Figure 5.6 depicts the hypersheet with the curvature flows streaming from the sources to the sinks. Under the initial metric, the hypersheet model is a minimal surface, therefore, it has negative Gaussian curvature everywhere, the geodesic curvatures along the boundaries are positive. Under the final metric, the interiors are flat, the geodesic curvature on boundaries are negative. Therefore, as shown in Figure 5.6, every circular boundaries on the hypersheet emits their curvatures and all the interior points inhale the curvatures during the Ricci flow process.

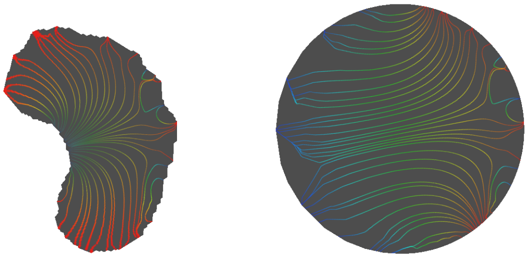

Figure 5.2: The curvature flow for the conformal deformation of the planar shape is shown in Figure 5.9. The curvature flows from red to blue.

To render the streams of the curvature flow, we utilize the texture coordinates which can be obtained with uniformization metrics. Given the $\nabla \mathbf{u}$ in each time, we compute the gradient vector in the texture domain. To visualize the flow with the gradient field, we use the image-based flow visualization [72] in the texture domain. Finally, we map the flow textures to the original mesh. Figure 5.2 and Figure 5.6 (d) illustrate the curvature flow using this method. The curvature flows from red to blue.

5.2 Visualization of Conformal Structure

The surface Ricci flow deforms a metric preserving the conformal structure. The conformal structure of a surface is an abstract concept and difficult to perceive. We visualize the conformal structure of a surface by two methods.

Canonical Embedding Within each conformal structure of the surface, the uniformization metric is the representative, which induces a unique embedding on the sphere, the Euclidean plane or the hyperbolic plane. Therefore, the conformal structure can be visualized by this kind of canonical embedding. For example, Figure 7.11 shows the brain surface is conformal to the unit sphere. On the sphere, we use the normal map from the original brain surface, therefore, the correspondence can be easily conveyed by comparing the local shading pattern. It is also evident that, the local shapes are well preserved, which is one prominent characteristics of the conformal map.

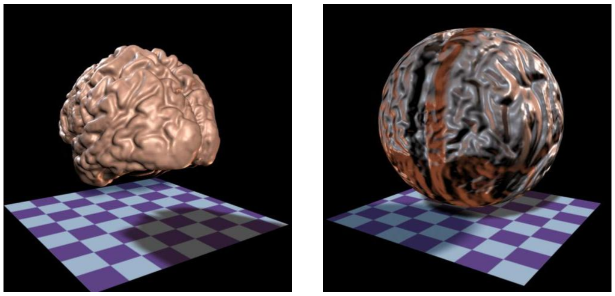

Figure 5.3: A Brain surface is conformal to a unit sphere.

For surfaces with complicated topologies, the canonical embedding conveys the complete information of the conformal structure. For example, for the hypersheet surface, it is of genus one with three boundaries. With its uniformization metric, it can be embedded onto the Euclidean plane periodically, each period is a parallelogram with three circular holes, the centers and the radius of the circles, the shape of the parallel gram are the fingerprint of the conformal structure.

Potential Fields on Surfaces The conformal structure of a surface can be depicted by the potential field on the surface. The equi-potential lines and the gradient lines are orthogonal everywhere, they form a canonical grids on the surface. Figure 5.5 illustrates the conformal structure on the bunny surface, the red curves are equipotential lines, and the blue curves are the gradient lines. Equivalently, the grids formed by the equipotential lines and the gradient lines can be replaced

(a) Conformal texture mapping (b) Non conformal texture mapping

(c) Fundamental domain (d) Skewed fundamental domain

Figure 5.4: The genus one surface (a) is periodically, conformally embedded onto the plane. Each period is a parallelogram (c). The shape of it is determined by the conformal structure. If the period is deformed (d), the induced texture mapping is not conformal (b)

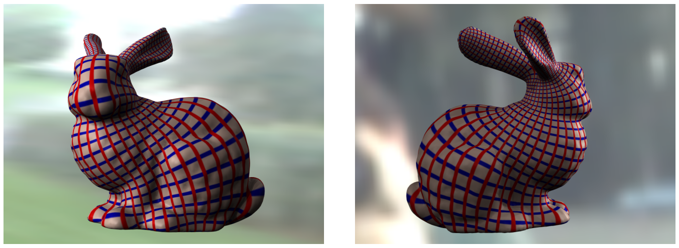

Figure 5.5: Conformal structure on the bunny surface is shown as a potential field.

by a checkerboard pattern. Figure 5.6 illustrates the conformal structure of the minimal surface model.

5.3 Visualization of Riemannian Metrics by Embedding

The result of Ricci flow is a Riemannian metric on the surface. It is very challenging to visualize a Riemannian metric. If the Gaussian curvature is positive everywhere, the metric determines an embedding in $\mathbb{R}^3$ as a convex surface unique up to rigid motion. Therefore, the metric can be visualized directly by the embedding. In discrete case, the uniqueness of the embedding is first proved by Cauchy for 2-spheres and by Alexandrov for disks.

A convex cap is the graph of a piecewise linear function over a convex polygonal region in the plane so that the value of the function is zero in the boundary.

Theorem 19 (Alexandrov)**.** *Let M be a topological disk with a convex Euclidean polyhedral met-*

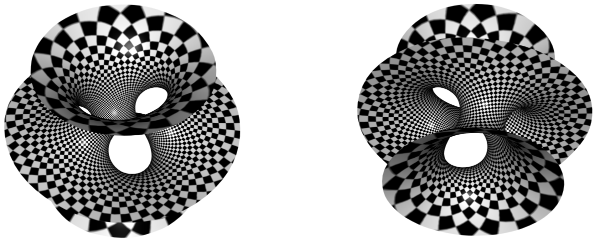

(a) Front view (b) Back view

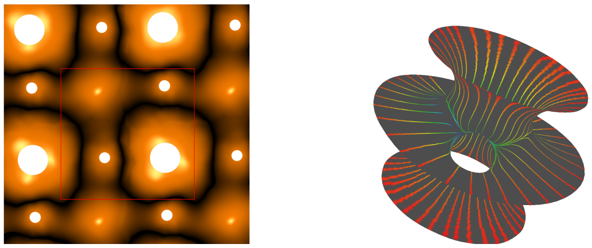

(c) Fundamental Domain (d) Curvature Flow

Figure 5.6: Conformal structure on the hyper-sheet surface is shown as a potential field in (a) and (b). The surface is embedded onto the plane using uniformization metric, the three boundaries are mapped to circles (c). Curvature flow is shown in (d), the curvature flows from the red to the blue.

ric, there exists a convex cap $C \subset \mathbf{R}^3$ with the upper boundary isometric to M. Besides, C is unique up to a rigid motion.

In his seminal theoretic work [39], Izemestiev proposed a variational method to determine the embedding. Our algorithms are based on his theoretic discovery.

Suppose M is a topological disk, represented as a mesh, then each vertex v_i is embedded in $\mathbb{R}^3$, the height function is h. The boundary vertices are on the xy plane, therefore heights are zeros for all boundary vertices. There exists a unique height function, which isometrically embeds M as a convex cap.

For each triangle of the mesh, the three edge lengths and the heights determine a prism, therefore all the dihedral angles along the edges can be determined. Algorithm 1 gives the details of computing the dihedral angles. The edge lengths, heights and the dihedral angles on all the prisms determine a energy, further on, this energy is defined by the height function. The energy is strictly concave. The height function, which reaches the global maximum of the energy, corresponds to the unique embedding.

Definition 34 (Izemestiev)**.** *Let C be a convex cap represented by (T,h). The total scalar curvature of C is defined as*

$$S(C) = \sum_{\Sigma/\partial D} h_i k_i + \sum_{intD} l_{ij}(\pi - \theta_{ij}) + \sum_{\partial D} l_{ij}(\frac{\pi}{2} - \eta_{ij})$$

where $k_i = 2\pi - \omega_i$ is the curvature at the i-th height of the cap C, l_{ij} is the length of the edge $e_{ij} \in T$, θ_{ij} is the total dihedral angle at an interior edge e_{ij}, and η_{ij} is the dihedral angle at a boundary edge e_{ij}, see Figure 5.7.

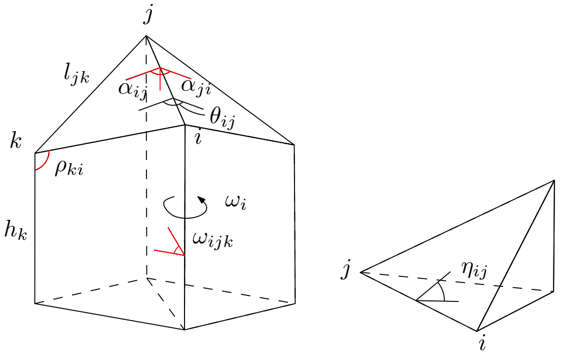

Figure 5.7: Total scalar function of a convex cap.

$\theta_{ij} = \alpha_{ij} + \alpha_{ji}$, $\omega_i = \sum_{f_{ijk} \in T} \omega_{ijk}$. Furthermore, the gradient of h equals

$$\frac{\partial S}{\partial h_i} = k_i, \nabla S = (k_1, k_2, \cdots, k_n)^T. \tag{5.3.1}$$

Theorem 20 (Izemestiev)**.** *The total scalar curvature S is strictly concave. The height function h corresponding to the global maximum induces the unique embedding.*

Suppose a topological disk D is given, with a discrete metric l, such that all curvatures are positive. We want to compute an embedding of (D, l) in $\mathbb{R}^3$. Equivalently, we want to find a height function h of D to realize the mesh. h can be obtained by maximizing the total scalar curvature S.

First, we consider the case of one triangle T_{ijk}, suppose the edge lengths l_{ij} and vertex heights h_i are given, the following simple algorithms realize it as a prism in $\mathbb{R}^3$ and compute all the dihedral angles,

Algorithm 1: Prism Embedding

```
For each edge $e_{ij}$, $\bar{l}_{ij} = \sqrt{l_{ij}^2 - (h_i - h_j)^2}$
$\theta_i \Leftarrow \cos^{-1} \frac{\bar{l}_{ij}^2 + \bar{l}_{ki}^2 - \bar{l}_{jk}^2}{2\bar{l}_{ij}\bar{l}_{ki}}$.
$v_i \Leftarrow (0, 0, h_i)$
$v_j \Leftarrow (\bar{l}_{ij}, 0, h_j)$
$v_k \Leftarrow (\bar{l}_{ki} \cos\theta_i, \bar{l}_{ki} \sin\theta_i, h_k)$
Compute the normal on all faces
Compute the dihedral angle on each edge.
```

Next, we consider the whole mesh, and compute the embedding with the given metric,

In practice, it is critical to choose the appropriate initial height functions. If all the curvature of interior vertices are zeros, the convex cap embedding is degenerated to planar case. We first embed one triangle onto the plane using the edge lengths, then embed all the faces sharing one edge with it. Then we keep growing the embed area until all the faces are flattened onto the plane.

Algorithm 2: Convex Cap Embedding

```
Initialize the height function $h$, $h|_{\partial D} = 0$.
Compute the dihedral angles $\omega_{ijk}$, $\alpha_{ij}$ and $\eta_{ij}$ by Algorithm 1.
Compute the height curvature $k_i$, edge curvature $\theta_{ij}$
while $max|k_i| \geq \varepsilon$ do
  $\nabla S \Leftarrow (k_1, k_2, \cdots, k_n)^T$,
  Update the height function $h+ = \delta \nabla S$
  Compute the dihedral angles $\omega_{ijk}$, $\alpha_{ij}$ and $\eta_{ij}$ by Algorithm 1.
  Compute the height curvature $k_i$, edge curvature $\theta_{ij}$
end while
$\bar{l}_{ij} \Leftarrow \sqrt{l_{ij}^2 - (h_i - h_j)^2}$
Embed $(D, \bar{l})$ on the plane, each vertex $v_i$ has coordinates $(x_i, y_i)$.
The final embedding is given by $v_i \Leftarrow (x_i, y_i, h_i)$.
```

In our application, we aim at visualizing the whole process of conformal deformation the Riemannian metric, therefore, we need to compute a sequence in order to improve the efficiency, we reuse the current embedding result as the initial guess for the next embedding. The Algorithm 3 describes the construction of a conformal deformation process in details. Suppose the input is a simply connected mesh, with a single boundary, also the target curvature $\mathbf{k}_1$ is given, such that all curvatures are positive.

Algorithm 3: Conformal Deformation

```
Define $\mathbf{k}_0$. such that $k_0(v) = 0, \forall v \notin \partial M$, $k_0(v) = \frac{2\pi}{m}, v \in \partial M$, $m$ is the number of boundary vertices.
Compute metric $l(0)$ from $\mathbf{k}_0$ using Ricci flow.
Compute the planar embedding of $(M, l(0))$, $h \equiv 0$.
$t = 0$
while $t < 1$ do
  $\mathbf{k}(t) = (1-t) \times \mathbf{k}_0 + t \times \mathbf{k}_1$.
  Compute metric $l(t)$ using Ricci flow.
  Embed $(M, l(t))$ using current height function as the initial guess.
  $t \Leftarrow t + \delta$
end while
```

Figure 5.9 demonstrates a conformal deformation of a planar surface. The curvature flow from boundary to the boundary across the surface. Because the interior vertices are always flat, there is no source or sink in the interior part. Namely, the curvature flow is divergence free.

Figure 5.10 demonstrates a conformal deformation of a convex cap surface. The conformality is represented by checkerboard texture mapping.

5.4 Visualization of the Proof of Poincaré-Koebe's uniformization theorem

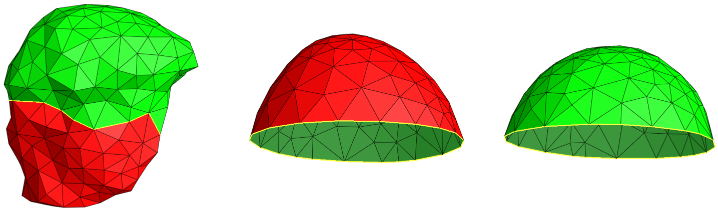

Figure 5.8: Illustration of the proof of Poincaré-Koebe theorem. The original surface is partitioned to two parts. Ricci flow is run on each component, such that all curvatures are non-negative. Each component is embedded to a convex cap, which is topologically equivalent to a hemisphere.

We visualize the proof of the uniformization theorem, as a 2-dimensional counterpart of the recent resolution of the Poincaré conjecture using Ricci flow. Namely, we want to visualize the proof of the following proposition using Ricci flow: *any closed simply closed surface is homeomorphic to a sphere(see Fig. 3).*

Suppose M is a closed, simply connected mesh,

1. Partition M to M_1 and M_2, such that $\gamma = M_1 \bigcap M_2$ is a simple closed curve on M, both M_1 and M_2 are simply connected with a single boundary.

2. Set the target curvature of M_i as $\mathbf{k}_i$, such that
$$\mathbf{k}_i(v) = 0, \forall v \in \partial M_i,$$
and
$$\mathbf{k}_i(v) = \frac{2\pi}{m_i}, m_i = |\partial M_i|, \forall v \notin \partial M_i,$$

3. Use Ricci flow to compute the desired metric l_i, which induces $\mathbf{k}_i$.

4. Embed (M_i, l_i) using the convex cap embedding algorithm.

5. The embedded M_i is homeomorphic to the semi-sphere using Gauss map.

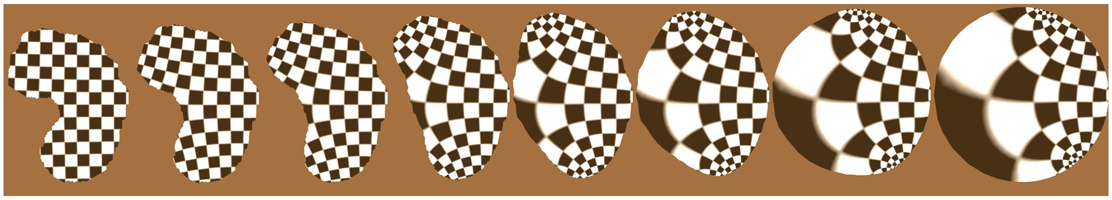

Figure 5.9: Conformal Deformation of a planar shape. The curvature flows from boundary points to boundary points. The deformation preserves the conformal structure.

Figure 5.10: Conformal Deformation of a convex cap surface.

Chapter 6

Application I: Use Ricci Flow to compute the Conformal map of High-Genus open surface

---

We apply *Surface Ricci flow* and *Koebe's method* for computing the canonical conformal mappings in Figure 1.2. Surface Ricci flow deforms the Riemannian metric of the surface according to its Gaussian curvature, such that the curvature evolves according to a heat diffusion process. Surface Ricci flow is applied for designing a Riemannian metric according to a user defined Gaussian curvature on interior points and geodesic curvature along the boundaries.

6.1 Koebe's Method

refers to the following process. Suppose the surface S is of topological type (g,b), $g>1, b>1$,

$$\partial S = \gamma_1 + \gamma_2 + \cdots + \gamma_b,$$

with a Riemannian metric $\mathbf{g}$. We fill the last $b-1$ boundary components $\{\gamma_k, k>1\}$ with $b-1$ topological disks. We compute the canonical conformal mapping, $\phi_1 : S \to \mathbb{H}^2$, which maps the left "hole" γ_1 to a circle on the hyperbolic disk $\mathbb{H}^2$. Then we fill the hole in $\mathbb{H}^2$ with a canonical hyperbolic disk. The mapping ϕ pulls back the hyperbolic metric of $\mathbb{H}^2$ to S. Then we open another hole γ_2, compute another canonical mapping ϕ_2 with the pull back metric induced by ϕ_1. Then we fill γ_2 in $\mathbb{H}^2$, open the third hole γ_3, and compute ϕ_3. We repeat this procedure of filling a hole, opening another hole, computing canonical conformal mapping on the hyperbolic disk. The holes become rounder and rounder, and all the holes converge to the circles eventually.

The key difficulty for the whole procedure is to determine the total geodesic curvature for each boundary component $\{\gamma_k\}$. This involves iterative searching method.

6.1.1 Histroy

Koebe's iteration method has been mainly developed for computing circular domains for planar multiply connected domains, detailed proofs for the convergence and the convergence rate can be found in Henrici's work [36]. Koebe's iteration method is generalized to genus zero surface with multiple boundary components in [77]. The method is applied for shape analysis in computer vision in [51]. The contours in an image segment the image plane to several connected components, each of them can be uniformized as a circle domain. Each contour is the intersection of two segments. This induces a diffeomorphism from the circle to itself. The diffeomorphisms on the circle, and the conformal module of the circle domains together can reconstruct the original contours by conformal welding method [68]. This method models the shape space of all planar contours.

6.1.2 Koebe's Iteration Algorithm

Koebe's iteration conformally deforms a surface with the constant curvature metric, such that the boundary components get rounder and rounder, and eventaully are transformed to circles.

Suppose a surface S is of topological type (g,b), $g > 0, b > 1$ with constant curvature metric. The boundary components of S are

$$\partial S = \Gamma^1 \cup \Gamma^2 \cdots \Gamma^b.$$

We assume that all the boundaries are totally disjoint closed Jordan curves.

At the beginning, we fill each hole Γ^i by a topological disk D^i with arbitrary Riemannian metric to get a closed metric surface $\bar{S}$. Then we use Ricci flow to compute the canonical metric of $\bar{S}$.

In each iteration step, we pick a boundary component of S, e.g. Γ^i. On $\bar{S}$ with the canonical metric, we remove the interior of Γ^i, denoted as D^i. Then we conformally deform $\bar{S} - D^i$ to a circle domain, and Γ^i becomes a circle. Then we fill Γ^i by the circular disk under the canonical metric to get the updated $\bar{S}$.

By repeating the iteration, the holes become rounder and rounder, and all the holes converge to the circles under the canonical metric eventually. The uniformization results in Figure 1.2 (e) and (f) are obtained using this method.

6.1.3 Main Theorem

The main theoretic result of this work is that, our Koebe's iteration method leads to the uniformization of metric surfaces with finite topological type.

Theorem 21 (Main Theorem)**.** *Suppose S is a metric surface with finite topological type. The Riemann surface obtained from the k-th Koebe's iteration S_k will converge to a unique circle domain on a Riemann surface, when $k \to \infty$.*

The detailed proof for the main theorem can be found in the Appendix . The algorithms are explained in details in the Section 6.2, the experimental results are reported in Section 6.3.

6.2 Computational Algorithm

The computational algorithms for the uniformization of surfaces with boundaries are based on discrete surface Ricci flow and Koebe's iteration method. General Koebe's method for genus zero surface with boundaries has been thoroughly explained in [77]. In the current work, we focus on high genus surfaces with boundaries.

6.2.1 Genus One Case

Given a genus one surface with topological type $(1,b), b > 0$, with boundary components $\{\Gamma^1, \Gamma^2, \cdots, \Gamma^b\}$. The target curvature for interior points should be zero everywhere. In smooth case the geodesic curvature for boundary points should be constant,

$$k_g(p) = c_k, \forall p \in \Gamma^i, 1 \leq i \leq b. \tag{6.2.1}$$

Furthermore, the total curvature of geodesic curvature along Γ^i should be -2π,

$$\int_{\Gamma^i} k_g(p)dp = -2\pi, 1 \leq i \leq b. \tag{6.2.2}$$

In the discrete case, the total geodesic curvature condition Eqn.6.2.2 is formulated as

$$\sum_{v_i \in \Gamma^i} \bar{K}(v_i) = -2\pi, 1 \leq i \leq b.$$

The constant geodesic curvature condition Eqn.6.2.1 is more complicated. Assume the vertices on Γ^i are sorted counter-clock-wisely $\{v_1, v_2, \cdots, v_n\}$, then

$$\bar{K}(v_i) = -\pi \frac{l_{i-1,i} + l_{i,i+1}}{\sum_{i=1}^{n} l_{i,i+1}} \tag{6.2.3}$$

where $l_{i,i+1}$ is the edge length of $[v_i, v_{i+1}]$ under the target metric, not the initial metric. In practice, we iteratively update the target curvature:

1. Compute the target curvature $\bar{K}(v_i)$. If v_i is an interior vertex, set $\bar{K}(v_i)$ be to 0. If v_i is on the boundary, use formula Eqn.6.2.3, where the edge lengths are computed using current conformal factor $\{u(v_i)\}$'s.

2. Compute the new conformal factor $\{u(v_i)\}$'s by the target curvature $\bar{K}(v_i)$ using Euclidean discrete surface Ricci flow.

3. Repeat step 1 and 2, until the change of the target curvature and conformal factor between two consecutive iterations are less than a given threshold. (In our experiments, we choose 10^{-5}).

Figure 1.2(e) shows one example of using this algorithm. The input surface is the Costa's minimal surface, which is of topological type $(1,3)$, namely, genus 1 with 3 boundaries. By running this algorithm, we compute a flat metric, such that all the boundary components are Euclidean circles. Then isometrically map a finite portion of its universal covering space onto the plane. A fundamental domain is shown as the rectangle in the bottom image of (b).

6.2.2 High Genus Case

The computational algorithm for high genus surface with multiple boundary components is much more complicated. Let S be a surface of topological type (g,b), $g>1, b>0$, then its Euler number $\chi(S)=2-2g-b$ must be negative. By Gauss-Bonnet theory, the canonical Riemannian metric should be hyperbolic. Similar to genus one case, condition Eqn.6.2.1, under the target hyperbolic metric, the geodesic curvature for boundary points should be constant. But the total geodesic curvature condition Eqn.6.2.2 should be replaced by the following *zero holonomy* condition.

Zero Holonomy Condition

Suppose S is with a hyperbolic metric $\mathbf{g}$. C is the universal covering space of S, $\pi : C \to S$ is the projection map. Then the pull back metric $\pi^*\mathbf{g}$ is the hyperbolic metric on C. C can be isometrically immersed in the hyperbolic space $\mathbb{H}^2$. All the deck transformations $\phi : C \to C$, such that $\pi \circ \phi = \phi$, are hyperbolic rigid motions. All deck transformations form a group, denoted as $Deck(S)$, which is a subgroup of the hyperbolic rigid motion group, which is the Möbius transformation group, $Mob(\mathbb{H}^2)$. The deck transformation group is isomorphic to the fundamental group of S, $\pi_1(S)$. Given a closed loop γ on S, its homotopy class is $[\gamma] \in \pi_1(S)$, the deck transformation corresponding to $[\gamma]$ induces a hyperbolic rigid motion, denoted as $\phi_{[\gamma]}$, which is called the *holonomy* of $[\gamma]$.

Suppose S is with the hyperbolic metric, S is a circle domain of a closed surface $\bar{S}$, if and only if the following zero holonomy condition holds:

$$\phi_{[\Gamma^i]} = id, \forall \Gamma^i \in \partial S. \tag{6.2.4}$$

Under the canonical hyperbolic metric, assume the boundary component Γ^i circles around an area Σ^i, then according to Gauss-Bonnet theorem

$$-\Sigma^i - \int_{\Gamma^i} k_g(p)dp = 2\pi. \tag{6.2.5}$$

The is equivalent to the zero homology condition above. In practice, Σ^i's are unknowns. The key point is to figure out the exact value of Σ^i's.

Surface with a Single Boundary

The following is the algorithm for computing the uniformization for a metric surfaces with topological type $(g,1)$, where $g>1$. Figure 6.1 shows one example for a genus two surface with a single boundary component $\{\Gamma^1\}$.

1. Compute a set of canonical fundamental group generators $\{a_1,b_1,a_2,b_2,\cdots,a_g,b_g\}$ using the method in [43], as shown in Figure 6.1 (b).

2. Compute the shortest path from the boundary Γ to the fundamental group generators, called as the *cut path*. Slice the surface along the fundamental group generators and the cut path, the result surface is a topological disk, denoted as $\hat{S}$. as shown in Figure 6.2 (a).

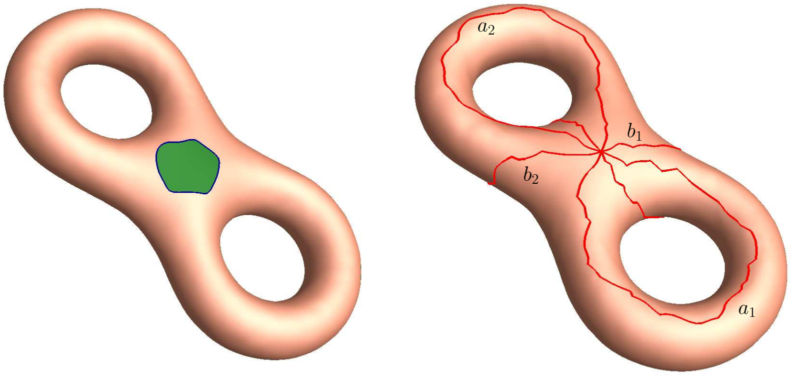

(a) Input surface (b) Fundamental group basis

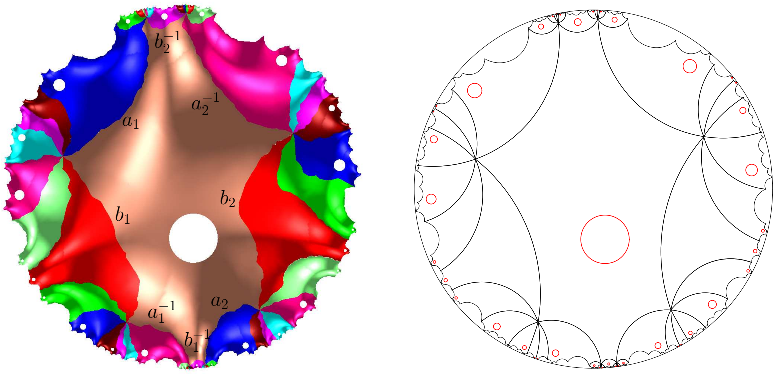

(c) Uniformization metric (d) Schematic representation

Figure 6.1: Uniformization for a genus two surface with a single boundary component.

3. Set $\Sigma^{+} = \pi$, $\Sigma^{-} = 0$.

4. If $\Sigma^{+} - \Sigma^{-} < \varepsilon$, where ε is a user defined threshold, return; else set $\Sigma^{1} = \frac{1}{2}(\Sigma^{+} + \Sigma^{-})$.

5. The total geodesic curvature for Γ^{1} is given by

$$\sum_{v_i \in \Gamma^1} \bar{K}(v_i) = -2\pi - \Sigma^{1},$$

   $\bar{K}(v_i)$ is proportional to the total length of adjacent edges. The target curvatures for interior vertices are zeros. Run discrete hyperbolic Ricci flow, with the above target curvatures, to get the hyperbolic metric $\mathbf{g}$.

6. Isometrically immerse $(\hat{S}, \mathbf{g})$ in $\mathbb{H}^2$. The details for the hyperbolic embedding algorithm can be found in [43]. As shown in Figure 6.2 (b) and (c).

7. If the immersion of $\hat{S}$ has an overlapping,as shown in (b) and (d),then set $\Sigma^{-} = \Sigma^{1}$; else if the immersion of $\hat{S}$ has a gap,as shown in (c) and (e), then set $\Sigma^{+} = \Sigma^{1}$.

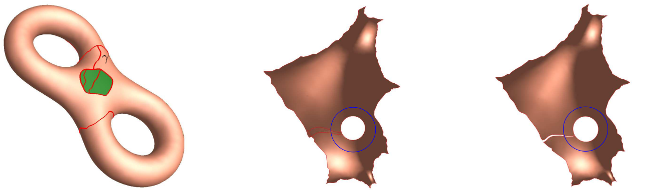
(a) Cut path (b) Overlapping (c) Gapping

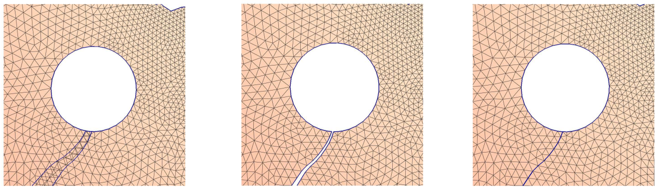
(d) 2nd iteration (e) 5th iteration (f) 8th iteration

Figure 6.2: Binary search for zero holonomy condition.

8. Repeat step 4 through 7.

Basically, the algorithm uses binary search to find the appropriate area parameter Σ^1, which satisfies the zero holonomy condition. Figure 6.2 (d), (e) and (f) show the searching process.

Once we obtain the hyperbolic metric with zero holonomy, we embed $\hat{S}$ onto $\mathbb{H}^2$. We denote the embedding as $\phi : \hat{S} \to \mathbb{H}^2$. Then we compute the deck transformation group generators $\{\alpha_1, \beta_1, \alpha_2, \beta_2, \cdots, \alpha_g, \beta_g\}$, such that α_i maps $\phi(b_i^{-1})$ to $\phi(b_i)$, the β_i maps $\phi(a_i)$ to $\phi(a_i^{-1})$. Then we use $\{\alpha_i, \beta_i\}$'s and their compositions to transform the fundamental domain $\phi(\hat{S})$ to tessellate the whole hyperbolic plane $\mathbb{H}^2$, as shown in Figure 6.1(c). Different copies of the transformed fundamental domain are encolored differently. We use hyperbolic geodesics to replace the boundaries of the fundamental domains in (c), and get the schematic representation of the tessellation, as shown in (d).

Surfaces with Multiple Boundary Components

For surfaces with multiple boundary components, we apply Koebe's iterative method as shown in Figure 6.3. Frames (a) and (b) show the input surface S with three boundary components $\{\Gamma^1, \Gamma^2, \Gamma^3\}$. The following is the algorithm pipeline,

1. Fill all the holes with topological disks $\{D^i\}$, such that $\partial D^i = \Gamma^i$, each D^i is with an arbitrary Riemannian metric, as sown in (c) and (d).

2. Set the target curvature to be zero for all vertices. Run discrete hyperbolic Ricci flow to compute the hyperbolic metric.

3. Choose one boundary component Γ^i, remove the interior D^i, and use the algorithm for surface with single boundary to compute the canonical hyperbolic metric, map it to the circle domain on the hyperbolic plane $\mathbb{H}^2$.

Table 6.1: Computational Time.

Surface	#Hole	#Vertex	#Face	#Iteration	#Time(s)
(a)	2	5001	10006	6	419
(b)	2	5910	111824	4	438
(c)	2	5673	11350	6	453
(d)	3	2505	5018	6	349
(e)	3	3999	8006	6	465

4. Fill in the interior of Γ^i, which is a hyperbolic circle, by a hyperbolic disk.

5. Repeat step 3 and 4, until all the boundary components are close enough to circles.

The details of the last step are explained as the following. Let Γ^i be a boundary component, the vertices are sorted as $\{v_1, v_2, \cdots, v_n\}$. We isometrically embed the neighborhood of Γ^i on the hyperbolic plane $\mathbb{H}^2$. We use Poincaré model for $\mathbb{H}^2$, where hyperbolic circles coincide with Euclidean circles. Each group of three vertices v_i, v_j, v_k determines a circle. The circle can be computed using the following formula. Let $\{z_i, z_j, z_k\}$ be the complex coordinates of them, then the center of the circumcircle is given by

$$c = \frac{|z_i|^2(z_j - z_k) + |z_j|^2(z_k - z_i) + |z_k|^2(z_i - z_j)}{z_i(\bar{z}_k - \bar{z}_j) + z_j(\bar{z}_i - \bar{z}_k) + z_k(\bar{z}_j - \bar{z}_i)},$$

the radius is $|z_i - c|$. We choose the indices $\{i, j, k\}$ to be $j = [i + \frac{n}{3}]$ and $k = [j + \frac{n}{3}]$, where $[x]$ means the greatest integer not exceeding x. Then we measure the maximal distance among the centers of $\frac{n}{3}$ circles, and the maximal difference among their radii. If both of them are less than a given threshold, then the algorithm terminates. In practice the threshold is chosen to be around 10^{-5}.

Figure 6.3 shows the process of Koebe's iteration algorithm. The result circle domain is shown in the 2nd last frame, the schematic representation is shown in the last frame.

6.3 Experiments

We implemented the discrete surface Ricci flow with Koebe's iteration using generic C++ language on Windows platform. The sparse linear system are solved using Matlab C++ library. The mesh is represented as the halfedge data structure. The computational time is tested on a desktop with 2.33 GHZ Dual CPU, 3.98 G RAM. The computational time and iteration numbers for surfaces in Figure 6.4 are reported in table 6.1, where one iteration makes one boundary component to be a circle. The threshold for the roundness of the holes is chosen to be 10^{-5}, the curvature error threshold is chosen to be 10^{-9}.

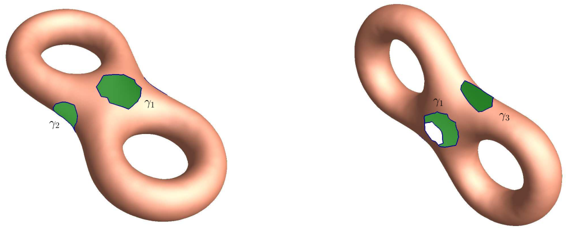

(a) Front view (b) Side view

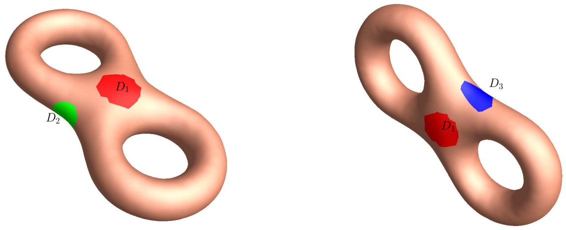

(c) Front view (d) Side view

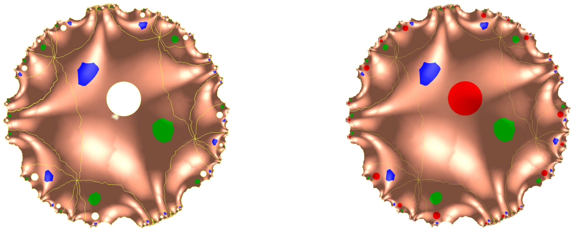

(e) Map γ_1 to circle (f) Fill γ_1

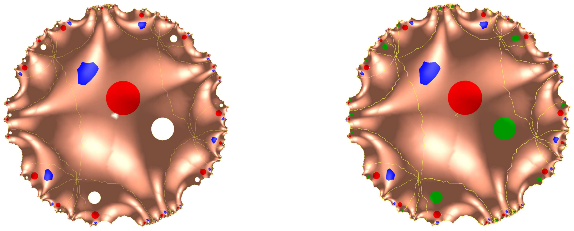

(g) Map γ_2 to circle (h) Fill γ_2

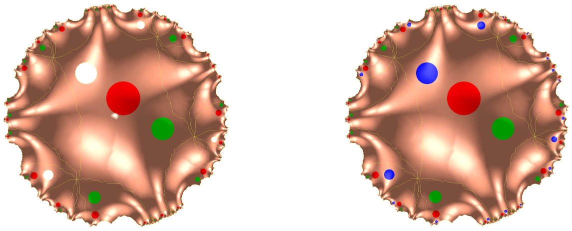

(i) Map γ_3 to circle (j) Fill γ_3

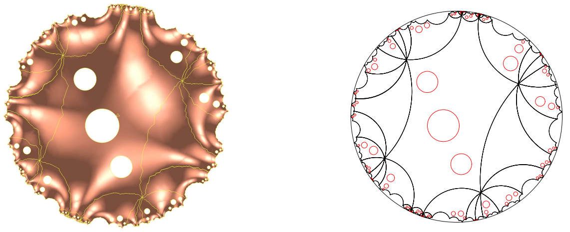

(k) Final result (l) Schematic Representation

Figure 6.3: Koebe's iterative method for a $(2,3)$ surface.

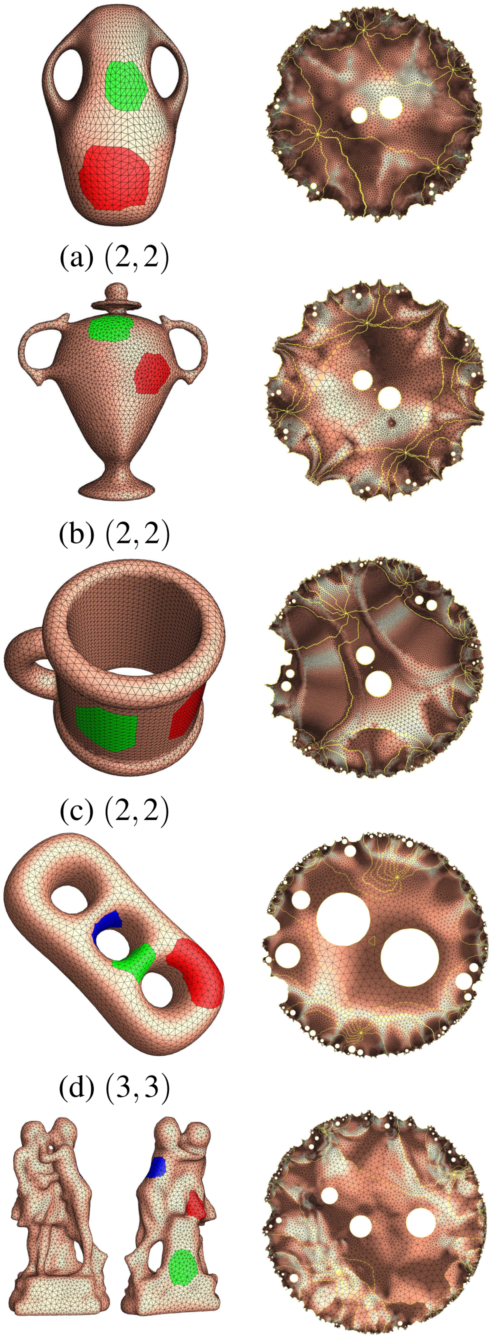

(a) $(2,2)$

(b) $(2,2)$

(c) $(2,2)$

(d) $(3,3)$

(e) $(3,3)$

Figure 6.4: Uniformization for high genus surfaces with boundaries (g,b).

6.3.1 Surface Matching

Based on the Chapter 6,Ricci Flow can compute the conformal mapping of open surfaces,

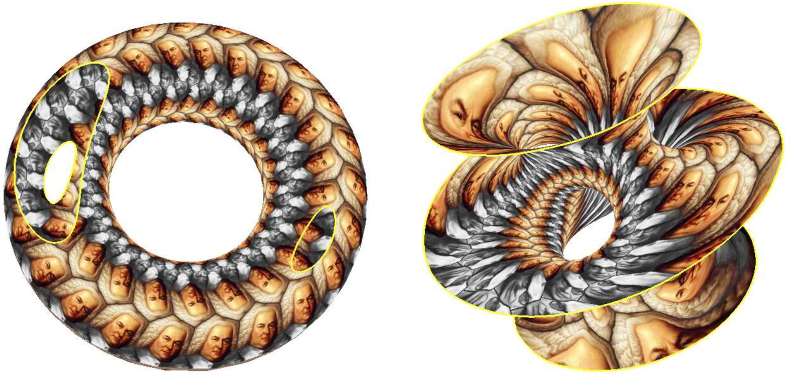

Figure 6.5: Surface matching between two genus one surfaces with three boundary components.

which is useful for surface matching and registration. Given two surfaces S_1 and S_2, we compute the canonical conformal mappings $\phi_1 : S_1 \to D$ and $\phi_2 : S_2 \to D$, where D is the canonical common domain, the boundaries are mapped to circles. Then we can build a diffeomorphism from the canonical domain to itself $\eta : D \to D$, then the mapping between the surface is given by $\phi_2^{-1} \circ \eta \circ \phi_1 : S_1 \to S_2$. Figure 6.5 shows one example of genus one surface with three boundaries. We show their mapping be transferring the texture from one surface to the other.

6.3.2 Shape Signature

Ricci Flow can be applied for shape indexing purpose. If there is a conformal diffeomorphism between two surfaces, then the two surfaces are *conformal equivalent*. Two surfaces are conformal equivalent if and only if they share the same *conformal module*. Surfaces can be classified by conformal equivalence relation, and conformal module can be used as their signatures.

For genus one surfaces with multiple boundary components, the fundamental domain is a parallelogram. We translate, rotate and scale the parallelogram, such that the longer edge is $1.0+0.0i$, the shorter edge is $a+bi$, then a,b and the centers and the radii of the inner circles consist the conformal module, which form the shape signature.

Chapter 7

Application II: Shape Signature based on Ricci Flow and Optimal Mass Transportation

A novel shape signature based on surface Ricci flow and optimal mass transportation is introduced for the purpose of surface comparison. First, the surface is conformally mapped onto plane by Ricci flow, which induces a measure on the planar domain. Second, the unique optimal mass transport map is computed which transport the new measure to the canonical measure on the plane. The map is obtained by a convex optimization process. This optimal transport map encodes all the information of the Riemannian metric on the surface. The shape signature consists of the optimal transport map, together with the mean curvature, which can fully recover the original surface.

The discrete theories of surface Ricci flow, and optimal mass transportation are explained thoroughly. The algorithms are given in details. The signature is tested on human facial surfaces with different expressions accquired by structured light 3D scanner based on phase-shifting method. The experimental results demonstrate the efficiency and efficacy of the method.

7.1 Introduction

With the rapid development of 3D acquisition technology, especially the invention of real time 3D scanning methods based on phase shifting principle [73], real time 3D geometric data is ubiquitous today. Matching, comparing, and analyzing vast amount of 3D data have become the research focus in many engineering fields. Surface comparison lays down the foundation for many geometric tasks, and play a crucial role in computer vision, computer graphics, medical imaging, geometric modeling and many other fields.

In this Chapter, we propose a novel method for shape representation and shape matching based on surface Ricci flow and optimal mass transportation theory.

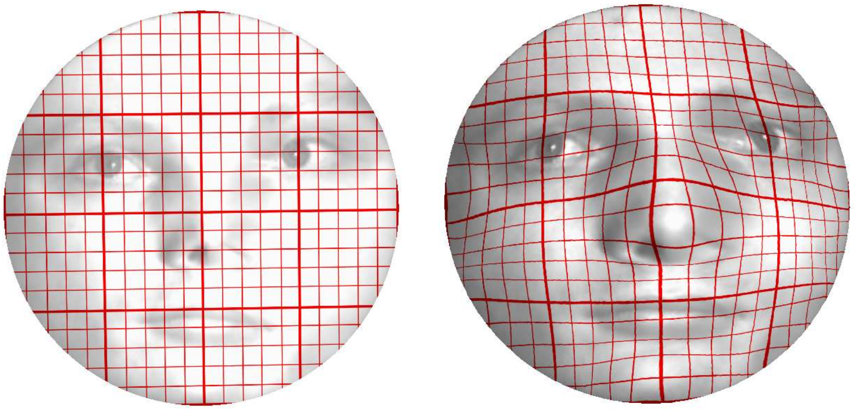

Figure 7.1: An optimal mass transportation mapping, $\eta : (\mathbb{D}, e^{2\lambda}dxdy) \to (\mathbb{D}, dxdy)$.

7.1.1 Optimal Mass Transport

Monge raised the classical "optimal mass transport problem" that concerns determining the optimal way, with minimal transportation cost, to move a pile of soil from one place to another. Formally, spaces X and Y are with measures μ and ν respectively, the transportation cost for moving from $x \in X$ to $y \in Y$ is $c(x,y)$. Given a map $T : X \to Y$, the total transportation cost is defined as

$$E(T) := \int_X c(x, T(x))\mu(x)dx.$$

A mapping is measure-preserving, if the pull back measure induced by T equals to the original measure

$$T^*\nu = \mu,$$

namely, for any measurable set $B \subset Y$,

$$\nu(B) = \mu(T^{-1}(B)).$$

Definition 35 (Optimal Transport Map)**.** *A measure-preserving map $T : X \to Y$ is called an optimal transport map, if it minimizes the total transportation cost*

$$T = \arg\min_T E(T). \tag{7.1.1}$$

Kantorovich [44] has proved the existence and uniqueness of the optimal transport plan. In late 1980's, Brenier [10] developed a different approach for a special optimal transport problem, where the cost function $c(x,y)$ is the quadratic distance $c(x,y) = \|x-y\|^2$. Brenier's theory proves that there is a convex function $u : X \to \mathbb{R}$, where the unique optimal transport map is given by its gradient map, $x \to \nabla u(x)$.

The Riemann mapping ϕ induces a measure on the disk $e^{2\lambda}dxdy$. We assume the total measure(and the total area of the original surface) is π, then there exists a unique optimal transport map $\eta : (\mathbb{D}, e^{2\lambda}dxdy) \to (\mathbb{D}, dxdy)$,that minimizes the transportation cost. Fig. 7.1 shows one example of such kind of optimal mass transportation mapping.

7.1.2 Shape Signature

The Riemann mapping $\phi : S \to \mathbb{D}$ maps the 3D surface S to the 2D disk $\mathbb{D}$, the Riemannian metric $\mathbf{g}$ is converted to the conformal factor function on the disk $\mathbf{g} = e^{2\lambda}(dx^2 + dy^2)$. Furthermore, we can compute the mean curvature H on the surface S, then push it forward to the disk. According to the theorem in differential geometry, the pair of functions (λ, H) on the disk and the boundary of the surface uniquely determines the surface.

Because the mapping η is measure-preserving, then the Jacobian of η equals to the conformal factor $e^{2\lambda}$. Therefore, the optimal mass transportation mapping η encode all the information of the Riemannian metric of the original surface $(S, \mathbf{g})$, namely

$$\mathbf{g} = det(J_\eta) dz d\bar{z},$$

where J_η is the Jacobian matrix of the mapping η.

We can treat the mapping η as a complex valued function defined on the disk. Then we can define the shape signature:

Definition 36 (Shape Signature)**.** *Suppose $(S, \mathbf{g}, p_0, p_1)$ is a marked topological disk, $\phi : S \to \mathbb{D}$ is the normalized Riemann mapping, $e^{2\lambda}$ is the conformal factor induced by ϕ. $\eta : (\mathbb{D}, e^{2\lambda}dxdy) \to (\mathbb{D}, dxdy)$ is the optimal transportation map. The mean curvature of the surface is H. The the pair $(\eta \circ \phi^{-1}, H \circ \phi^{-1})$ defined on the disk is the shape signature of the marked disk $(S, \mathbf{g}, p_0, p_1)$.*

The current work is based on the following theorem, the proof will be given in Sec 7.3,

Theorem 22 (Main)**.** *Given two marked topological disks $(S_1, \mathbf{g}_1, p_0, p_1)$ and $(S_2, \mathbf{g}_2, q_0, q_1)$, their signatures are (η_1, H_1) and (η_2, H_2).*

1. *Two surfaces are isometric, if and only if $\eta_1 \equiv \eta_2$.*
2. *Two surfaces differ by a rigid motion $\psi : \mathbb{R}^3 \to \mathbb{R}^3$, if and only if $\eta_1 \equiv \eta_2$, $H_1 \equiv H_2$, and the inverse of the normalized Riemann mappings restricted on the disk boundary $\phi_k^{-1}|_{\partial\mathbb{D}} : \partial\mathbb{D} \to \mathbb{R}^3, k = 1, 2$, differ by ψ,*

$$\phi_2^{-1}|_{\partial\mathbb{D}} = \psi \circ \phi_1^{-1}|_{\partial\mathbb{D}}.$$

Therefore, in order to compare two shapes, it is sufficient for us to compare their signatures on the disk. For this purpose, we define the shape distance between two marked topological disks as

Definition 37 (Shape Distance)**.** *Given two marked topological disks $(S_k, \mathbf{g}_k, p_0^k, p_1^k)$, $k = 1, 2$, with signatures (η_k, H_k), the shape distance between them is*

$$d(S_1, S_2) := \alpha \int_{\mathbb{D}} |\eta_1(z) - \eta_2(z)|^2 dxdy + (1-\alpha) \int_{\mathbb{D}} |H_1(z) - H_2(z)|^2 dxdy \tag{7.1.2}$$

where $0 \le \alpha \le 1$. We call the first term as η-distance, the second term H-distance.

Comparing functions defined on the planar disk is much easier than comparing the 3D surfaces directly. This novel surface comparison method converts 3D geometric problems to 2D functional ones, which is more efficient in practice.

7.2 Previous Works

7.2.1 Shape Signatures

Previous Methods There is a vast literature of shape signature. Here we only review the most relevant ones. The first category is *local shape signature*, which computes the shape distribution in a local neighborhood of the point of interest, such as [16],[3],[8]. In this category, two widely used point signatures are spin images [3] and shape context [8], which are invariant under rigid transformations. Hilaga et al. [37] and Gal et al. [27] extend the shape context to the non-rigid setting, by using geodesic distances.

The second category is *multi-scale local surface signature*. Li and Guskov [48] define this type of signatures by first obtaining a series of increasingly smoothed versions of a given shape and then constructing point signatures for features found at each smoothed version of the surface. Another approach to obtain a multi-scale signature is by convolving a function of a certain geometric property, such as the indicator of the interior of the domain with a series of kernel functions like a Gaussian of increasing width. Integral invariant signatures proposed by Manay et al. [56] for domains in 2D, that have been used for global shape matching in [28] and analyzed extensively by Pottmann et al. [63], fall into this category.

The widely used Heat Kernel Signature [42] is a multi-scale signature, which uses the heat diffusion to reflect the Riemannian metric of the manifold. The scale of the signature is controlled by the diffusion time, the longer the time is, the large range of geometry it reflects. Furthermore, comparing to geodesic based methods, heat kernel signature is robust to topological noises.

The third category is *global signature*. The Global Point Signature (GPS) proposed by Rustamov [55] falls into this category. For a fixed point x, GPS(x) is a vector whose components are scaled eigenfunctions of the Laplace-Beltrami operator evaluated at x. GPS is invariant under isometric deformations of the shape, yet does not use geodesic distances explicitly. Ovsjanikovcet al. [62] develop an algorithm to detect global intrinsic symmetries based on GPS by observing that the intrinsic symmetries of a shape become extrinsic or Euclidean in the signature space. Due to the global nature of GPS, it can not be used to detect partial symmetries or to perform partial matching. Heat Kernel signature is capable of multi-scale comparison between neighborhoods of points on the same shape, or even across different shapes.

Comparison Comparing the existing shape signatures, our proposed method has the following merits:

1. *No information loss.* Most signatures lose some geometric information of the original shape, therefore the original surfaces can not be fully recovered solely from the signatures. In contrast, our method encodes all the geometric information, in theory, the original surface can be fully determined.
2. *Both intrinsic and extrinsic.* Some existing signatures only reflects the Riemannina metric information, such as the heat kernel signature, which doesn't reflect any information of the embedding. Some other signatures, like spin image, heavily depends on the embedding. Our method has two parts, the optimal transport map η signature is intrinsic, and invariant under the isometric deformation; the mean curvature depends on the embedding, invariant under the rigid motion.

3. *Global and Local* For local shape signatures, no global geometric characteristics can be captured, such as spin image; for global shape signatures, the local geometric information is lost, as as GPS. Our signatures reflect all the local geometric information, but also influenced by the global geometric structure.
4. *Dimension Reduction.* Most shape signatures are still defined on the original 3D surface, such as the heat kernel signature (HKS). In contrast, ours are defined on 2D disk, which greatly simply the downstream geometric tasks, such as comparison and analysis.
5. *Multi-Scale.* Our signatures are represented as functions on a disk, which can be converted to multi-scale representations, such as using wavelet, for Fourier analysis. This gives natural multi-scale signatures of the original shape.

On the other hand, our method can not handle incomplete data, partial occlusion and the mean curvature is sensitive to local geometric noises; the η signature is sensitive to topological noises. Therefore, in practice, the input geometric data need to be preprocessed.

7.2.2 Optimal mass transport

There are different types of numerical approaches for solving the optimal mass transportation map problem: 1. continuous approach, where both the measures on the source and target are continuous. It requires solving Monge-Ampere equation. Explicit solutions are only known for some very specific shapes and measures; 2. semi-continuous approach, where the target measure is the sum of Dirac functions. The solution can be obtained by BrenierâĂŹs method, like Merigot's work [58], and the current work; and a discrete approach such as [59], where both measures are sums of Diracs and can be solved by linear programming. The semi-continuous approach has $O(n)$ unknowns, yet the discrete approach has $O(n^2)$ unknowns.

Some approaches based on Monge-Kantorovich theory have been proposed. Zhu et al. [79] applied optimal mass transport to flatten blood vessel in an area-preserving way for medical visualization. Haker et al. [34] proposed to use optimal mass transport for image registration and warping. The method is parameter free and has the unique global optimum. Dominitz and Tannenbaum [22] proposed to use optimal mass transport for texture mapping. The method first begins with an angle-preserving mapping and then correct it using the mass transport procedure derived via a certain gradient flow. Rehman et al. [71] presented a method for 3D image registration based on the optimal mass transport problem. Meanwhile, they stress the fact that the optimization of OMT is computationally expensive and emphasize it is important to find efficient numerical methods to solve this issue, and it is also crucial to extend the results to 3D surfaces.

Lipman et al. [49] introduced a novel metric for shape comparison based on conformal uniformization and optimal mass transport. The metric is invariant under Möbius transformation. Lipman and Daubechies used the Monge-Kontorovich approach for computing the optimal mass transport map, which can be easily replaced by Briener's approach in Merigot's work and our current work. Lipman and Daubechies' method is rigorous and powerful for practical applications. Later in the work [50] Lipman et al. provided a convergence analysis of the discrete approximation to the arising mass transportation problems. Mémoli [60] presented a modification and expansion of the original Gromov-Hausdorff notion of distance between metric spaces which considers probability measures defined on measurable subsets of metric spaces. The computational techniques in this paper are applicable are not restricted on the nature of the objects. Hua et al's work [25, 26, 41], presenting scale-invariant features based on geometric mapping and area-preserving mapping,

There are also works based on Monge-Brenier theory. Merigot [58] introduced a multi-scale approach to optimal transport, which is based on the theoretic result of Aurenhammer et al. [23]. The proof in Aurenhammer et al.'s work is different from that in Gu. et al's work [32]. Aurenhammer et al.'s work only proves the existence of the solution, yet Gu et al.'s work gives the proof for both existence and uniqueness. Their energy forms are different. Merigot's work only computes the gradient of the energy, and uses the L-BFGS method; whereas our work has an explicit formula for the Hessian matrix of the energy, and uses Newton's method directly. Merigot's method uses a multi-scale technique, which greatly improves the efficiency. de Goes et al. [20] have provided a optimal-transport driven approach for 2D shape reconstruction and simplification. Then they have presented a formulation of capacity-constrained Voronoi tessellation as an optimal transport problem for image processing [19]. This method produces high-quality blue noise point sets with improved spectral and spatial properties. All the works mentioned above for matching and registration are for 2D domains. In contrast, our work focuses on applying Alexandrov map (equivalent to Monge-Brenier based optimal mass transport method) for 3D surface.

7.3 Theoretic Background

7.3.1 Optimal Mass Transportation

Optimal mass transportation map is a special area-preserving mapping.

Definition 38 (Area-preserving Mapping)**.** *Suppose* $\phi : (S_1, \mathbf{g}_1) \to (S_2, \mathbf{g}_2)$ *is a diffeomorphism, the pull back metric induced by* ϕ *on* S_1 *is* $\phi^*\mathbf{g}_2$*, if*

$$det(\mathbf{g}_1) = det(\phi^*\mathbf{g}_2), \tag{7.3.1}$$

then ϕ *is an area-preserving mapping.*

Convex Geometry Convex geometry studies convex polyhedra in Euclidean space $\mathbb{R}^n$. The Minkowski theorem states that a convex polyhedron can be fully determined by its face normals and face areas.

Theorem 23 (Minkowski [66])**.** *Given k unit vectors* $\mathbf{n}_1, \cdots, \mathbf{n}_k$ *not contained in a half-space in* $\mathbb{R}^n$ *and* $A_1, \cdots, A_k \geq 0$*, such that*

$$\sum_{i=1}^{k} A_i \mathbf{n}_i = 0,$$

then there exists a convex polytope P with faces $F_1, \cdots, F_k$*, such that the normal to* F_i *is* $\mathbf{n}_i$ *and the area of* F_i *is* A_i*. P is unique up to translations.*

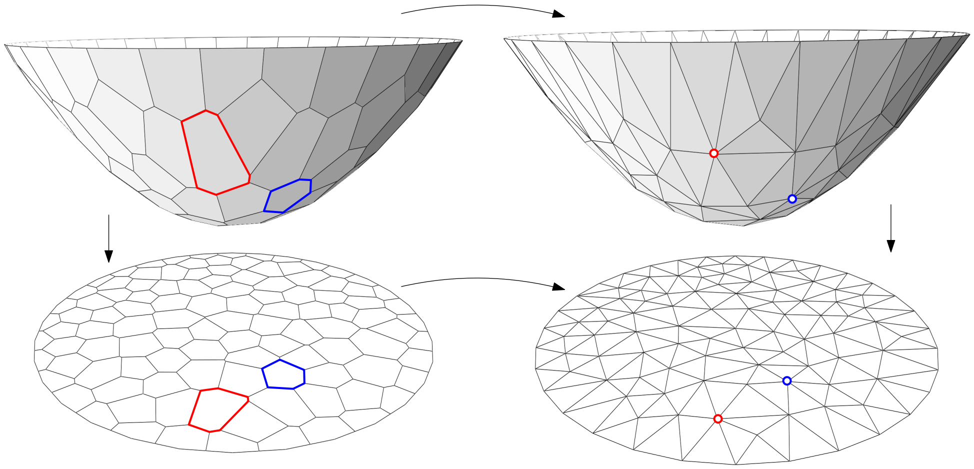

Figure 7.2: A PL convex function induces a cell decomposition of Ω. Each cell is mapped to a point.

Alexandrov generalized Minkowski's result to non-compact convex polyhedra. As shown in Fig.7.2, given k planes $\pi_i : \langle x, p_i\rangle + h_i$, one can construct a piecewise linear convex function

$$u(x) = \max_i \{\langle x, p_i\rangle + h_i | i = 1, \cdots, k\}, \tag{7.3.2}$$

whose graph is an infinite convex polyhedron. The PL convex function produces a convex cell decomposition $\{W_i\}$ of $\mathbb{R}^n$:

$$W_i = \{x | \langle x, p_i\rangle + h_i \geq \langle x, p_j\rangle + h_j, \forall j\} = \{x | \nabla u(x) = p_i\}. \tag{7.3.3}$$

Alexandrov shows that the convex polyhedron is determined by the face normal, or equivalently the gradient $\{p_i\}$ and the projected area $\{A_i\}$.

Theorem 24 (Alexandrov [4])**.** *Given a compact convex domain Ω in $\mathbb{R}^n$, if $p_1, \cdots, p_k$ are distinct in $\mathbb{R}^n$, $A_1, \cdots, A_k > 0$ such that*

$$\sum_{i=1}^{k} A_i = vol(\Omega),$$

then there exists a piecewise linear function $u(x) = \max_i \{\langle x, p_i\rangle + h_i\}$ unique up to translations, such that

$$Vol(W_i \cap \Omega) = A_i,$$

where W_i is defined in Eqn. 7.3.3.

Definition 39 (Alexandrov map)**.** *We call the gradient map $\nabla u : x \to \nabla u(x)$ the Alexandrov map, or briefly A-Map.*

According to Monge-Brenier theory [10], the Alexandrov map is the unique Optimal Mass Transport map that minimizes the following mass transport energy

$$\int_{\Omega} \|x - f(x)\|^2 dx,$$

among all mass preserving maps $f : \Omega \to \{p_1, \cdots, p_k\}$, such that

$$Vol(f^{-1}(p_i)) = A_i.$$

The computation of the Alexandrov map is equivalent to computing the so-called *power diagram* in computational geometry.

Power Diagram The power diagram is a generalization of Voronoi diagrams. Suppose each point p_i has a weight h_i, which may be positive or negative, the *power distance* from a point $\mathbf{x} \in \mathbb{R}^2$ to $\mathbf{p}$ is defined as

$$\text{Pow}(x, p_i) = \frac{1}{2}\|x - p_i\|^2 - \frac{1}{2}h_i.$$

When h_i is positive, the intuitive meaning of the power distance is one half of the squared distance from x to the tangent point of x to the circle centered at p_i with radius $\sqrt{h_i}$. The *power diagram* is the Voronoi diagram when we use power distance instead of the standard L_2 distance metric. It is again a partition of the Euclidean plane into polygonal cells, although some sites may have empty power cells $\{W_i\}$.

$$\begin{aligned} W_i &= \{x | Pow(x, p_i) \leq Pow(x, p_j), \forall j\} \\ &= \{x | \langle x, p_i \rangle + 1/2(h_i - |p_i|^2) \geq \langle x, p_j \rangle + 1/2(h_j - |p_j|^2), \forall j\} \end{aligned}$$

Comparing this equation to Eqn.7.3.3, it is obvious that computing a power diagram is equivalent to compute the Alexandrov map.

Traditionally, constructing a power diagram is converted to computing the convex function in Eqn.7.3.2, which can be solved using convex hull algorithms in time $O(n \log n)$, such as the divide-and-conquer algorithm [64] or the randomized incremental algorithm [17].

The *power Delaunay triangulation* on the point set $\{p_1, \cdots, p_k\}$ is the dual to the power diagram. Two power cells W_i and W_j are adjacent in the diagram, if and only if there is an edge connecting p_i and p_j in the dual triangulation.

Optimal Mass Transportation Map by Variational Principle The computation of Alexandrov map is based on the following theorem.

Theorem 25 (Generalized Alexandrov)**.** *Given a convex domain $\Omega \subset \mathbb{R}^n$, with measure density $\rho : \Omega \to \mathbb{R}$, and a discrete point set $P = \{p_1, \cdots, p_k\}$ with discrete measures $\mu = \{\mu_1, \cdots, \mu_k\}$, such that*

$$\int_{\Omega} \rho(x) dx = \sum_{i=1}^{k} \mu_i,$$

then there exists a $\mathbf{h} = \{h_1, \cdots, h_k\}$ *unique upto translations, such that the convex function* $u(x) = \max_i\{\langle x, p_i\rangle + h_i\}$, *induces a cell decomposition of* $\mathbb{R}^n$, $\mathbb{R}^n = \bigcup_{i=1}^k W_i(\mathbf{h})$, *and the area of each cell*

$$w_i(\mathbf{h}) = \int_{W_i(\mathbf{h})\cap\Omega} \rho(x)dx$$

equals to μ_i. $\mathbf{h}$ *is the unique global minimizer of the convex function*

$$E_\mu(\mathbf{h}) = \sum_{i=1}^k \mu_i h_i - \int_{\mathbf{0}}^{\mathbf{h}} \omega, \tag{7.3.4}$$

where the differential form $\omega = \sum_{i=1}^k w_i(\mathbf{h})dh_i$.

The computation on 2D is based on power diagram and power triangulation. Suppose, two voroni cells $W_i(\mathbf{h}), W_j(\mathbf{h})$ are adjacent and they share a common edge e_{ij}. The edge e_{ij} has a dual Delaunay edge $\bar{e}_{ij}$. The norm with respect to ρ is defined as

$$|e|_\rho = \int_e \rho(x)dx, \tag{7.3.5}$$

and $|e|$ is just the traditional Euclidean length. By direct computation, we can show

$$\frac{\partial w_i}{\partial h_j} = \frac{\partial w_j}{\partial h_i} = \frac{|e_{ij}|_\rho}{|\bar{e}_{ij}|}.$$

Therefore the differential 1-form $\omega = \sum_{i=1}^k w_i dh_i$ is a closed 1-form, $d\omega = 0$. By Brunn-Minkowski inequality [4], the admissible space

$$\mathscr{H} := \{\mathbf{h} | \forall i, w_i(\mathbf{h}) > 0, \sum_i h_i = 0\}$$

is non-empty and convex. Therefore, $E(\mathbf{h}) = \int^{\mathbf{h}} \omega$ is well defined. The gradient of E is $(w_1, \cdots, w_k)$, the Hessian matrix of E is as follows. The off diagonal element is given by

$$\frac{\partial^2 E}{\partial h_i \partial h_j} = \frac{\partial w_i}{\partial h_j} = \frac{|e_{ij}|_\rho}{|\bar{e}_{ij}|}. \tag{7.3.6}$$

Because $\sum_i w_i(\mathbf{h}) = const$, therefore the diagonal element is given by

$$\frac{\partial w_i}{\partial h_i} = -\sum_{j\neq i} \frac{\partial w_i}{\partial h_j}, \tag{7.3.7}$$

the negative Hessian matrix is diagonal dominant, so E is concave on $\mathscr{H}$. Therefore E_μ in Eqn. 7.3.4 is positive definite, the desired solution is the unique global minimum.

An Alexandrov map can be obtained by optimizing the convex energy $E_\mu(\mathbf{h})$using Newton's method, where each iteration is to construct a power diagram dynamically. Algorithmically, each iteration in the optimization process is to construct a power diagram, which is classical in computational geometry and can be solved using mature, robust and efficient software packages, such as [11].

7.3.2 Shape Distance

The following lemma shows that the Riemann mapping ϕ and the optimal transportation map η encodes all the Riemannian metric information of the original surface.

Lemma 19. *Suppose a Riemannian surface* $(S,\mathbf{g})$ *with total area* π*, which is a topological disk, the Riemann mapping is* $\phi : (S,\mathbf{g}) \to (\mathbb{D}, dzd\bar{z})$*, the conformal factor induced by* ϕ *is* $\lambda : S \to \mathbb{R}$*, the optimal transportation map is* $\eta : (\mathbb{D}, e^{2\lambda\circ\phi^{-1}(z)}dzd\bar{z}) \to (\mathbb{D}, dzd\bar{z})$*, then the Riemannian metric of the original surface is given by*

$$\mathbf{g}\circ\phi^{-1}(z) = det(J_\eta)dzd\bar{z}.$$

Proof. Because $\phi : (S,\mathbf{g}) \to (\mathbb{D}, dzd\bar{z})$ is conformal, according to Eqn. 1.1.1

$$\mathbf{g}\circ\phi^{-1}(z) = e^{2\lambda\circ\phi^{-1}(z)}dzd\bar{z},$$

Because $\eta : (\mathbb{D}, e^{2\lambda}dzd\bar{z}) \to (\mathbb{D}, dzd\bar{z})$ is an optimal transportation map, therefore it is area-preserving. According to Eqn. 7.3.1,

$$e^{2\lambda} = det(J_\eta).$$

Combine the above two equations, we get the formula in the lemma. □

The following theorem is classical in surface differential geometry.

Theorem 26. *Suppose* $(S,\mathbf{g})$ *is a closed Riemannian surface embedded in in* $\mathbb{R}^3$ *with isothermal coordinates, then* S *is determined unique upto a rigid motion by the conformal factor* λ *and mean curvature function* H *defined on isothermal coordinates. If* S *has boundaries, then* S *is determined by* (λ, H) *and Dirichlet boundary condition.*

We now give the proof for the main theorem 22,

Proof. Suppose two marked topological disks $(S_1,\mathbf{g}_1,p_0,p_1)$ and $(S_2,\mathbf{g}_2,q_0,q_1)$ are given.

We prove the first claim:
'$\Longrightarrow$' if there exists an isometry $f : S_1 \to S_2$, such that $f(p_k) = q_k$, $k = 0,1$, consider the normalized Riemann mappings $\phi_1 : S_1 \to \mathbb{D}$, $\phi_1(p_0) = 0$ and $\phi_1(p_1) = 1$, $\phi_2 : S_2 \to \mathbb{D}$, $\phi_2(q_0) = 0$ and $\phi_2(q_1) = 1$, the composition

$$\phi_2 \circ f \circ \phi_1^{-1} : \mathbb{D} \to \mathbb{D}$$

is conformal, therefore a Möbius transformation, which fixes 0 and 1, hence it is the identity, namely

$$f = \phi_2^{-1} \circ \phi_1,$$

Suppose $\mathbf{g}_1 = e^{2\lambda_1}\phi_1^* dzd\bar{z}$, and $\mathbf{g}_2 = e^{2\lambda_2}\phi_1^* dzd\bar{z}$, therefore

$$f^*\mathbf{g}_2 = e^{2(\lambda_2-\lambda_1)}\mathbf{g}_1,$$

because f is an isometry, therefore $\lambda_1 \equiv \lambda_2$. Therefore the measures on the disk induced by ϕ_1 and ϕ_2 are equal. According to the uniqueness of the optimal transportation map, we obtain $\eta_1 \equiv \eta_2$.
'$\Longleftarrow$' Reversely, if $\eta_1 \equiv \eta_2$, according to lemma 19, $\lambda_1 \equiv \lambda_2$. Define the composition $f : S_1 \to S_2$, $f := \phi_2^{-1} \circ \phi_1$, because ϕ_1 and ϕ_2 are conformal, so f is conformal, $f^*\mathbf{g}_2 = e^{2(\lambda_1 - \lambda_2)}\mathbf{g}_1$, so f is an isometry.
We prove the second claim:
From the first claim, $\eta_1 \equiv \eta_2$ is equivalent to $\lambda_1 \equiv \lambda_2$, then according to theorem 26, the claim holds. □

The shape distance descriptors include both conformal factor and the mean curvature. The conformal factor is intrinsic, and invariant under isometric deformation. The mean curvature is extrinsic. The smiling expression change is close to be isometric, therefore, the conformal factor descriptor is similar. But the embedding is changed by the expression deformation, therefore, the mean curvature descriptors are different.

7.4 Computational Algorithm

7.4.1 Conformal Mapping

In discrete setting, the captured surfaces are represented as discrete polyhedral surfaces. Suppose S is a topological surface, V is a set of points on S, (S,V) is called a *marked surface*. T is a triangulation of S, whose vertices are in V, then (S,T) is called a *triangular mesh*. In the following discussion, we use E and F to represent the edge and face sets. A piecewise linear Riemannian metric (PL metric) on (S,V) is a flat cone metric, whose cone points are in V, represented by edge lengths.

Definition 40 (Discrete Yamabe Flow with Surgery)**.** *Given a surface (S,V) with a discrete metric d, given a target curvature function $\bar{K} : V \to \mathbb{R}$, $\bar{K}(v_i) \in (-\infty, 2\pi)$, and the total target curvature satsifies Gauss-Bonnet formula, the discrete Yamabe flow is defined as*

$$\frac{du(v_i)}{dt} = \bar{K}(v_i) - K(v_i), \tag{7.4.1}$$

under the constraint $\sum_{v_i \in V} u(v_i) = 0$. During the flow, the triangulation on (S,V) is updated to be Delaunay with respect to $d(t)$, for all time t.

The existence of the solution to the Yamabe flow is guaranteed by the following theorem.

Theorem 27. *Suppose (S,V) is a closed connected surface and d is any discrete metric on (S,V). Then for any $\bar{K} : V \to (-\infty, 2\pi)$ satisfying Gauss-Bonnet formula, there exists a discrete metric $\bar{d}$, unique up to scaling on (S,V), so that $\bar{d}$ is discrete conformal to d and the discrete curvature of $\bar{d}$ is $\bar{K}$. Furthermore, the $\bar{d}$ can be obtained by discrete Yamabe flow with surgery.*

```
Algorithm 4: Discrete Surface Yamabe Flow
  Input: The inputs include:
    1. A triangular mesh $\Sigma$, embedded in $\mathbb{E}^3$;
    2. A target curvature $\bar{K}$, $\sum \bar{K}_i = 2\pi\chi(\Sigma)$ and $\bar{K}_i \in (-\infty, 2\pi)$.
  Output: A discrete metric conformal to the original one, which realizes the target curvature $\bar{K}$.
  Initialize the discrete conformal factor $u$ as 0 and conformal structure coefficient $\eta$, such that
    $\eta(e)$ equals to the initial edge length of $e$.
  while $\max_i |\bar{K}_i - K_i| > threshold$ do
    Compute the edge length from $\gamma$ and $\eta$
    Update the triangulation to be Delaunay using diagonal edge swap for each pair of adjacent
      faces
    Compute the corner angle $\theta_i^{jk}$ from the edge length using cosine law
    Compute the vertex curvature $K$
    Compute the Hessian matrix $H$
    Solve linear system $H\delta u = \bar{K} - K$
    Update conformal factor $u \leftarrow u - \delta u$
  end while
  Output the result circle packing metric.
```

Furthermore, it has been show that Yamabe flow is the negative gradient flow of the following Yamabe energy,

$$f(u_1, u_2, \cdots, u_n) = \int^{(u_1, u_2, \cdots, u_n)} \sum_{v_i \in V} (\bar{K}(v_i) - K(v_i)) du_i. \tag{7.4.2}$$

The gradient of Yambe energy is $\nabla f(u_1, \cdots, u_n) = (\bar{K}_1 - K_1, \bar{K}_2 - K_2, \cdots, \bar{K}_n - K_n)^T$. The Yamabe energy is strictly concave in the subspace $\sum_{v_i \in V} u_i = 0$. The Hessian matrix can be formulated explicitly. The cotangent edge weight is defined as

$$w_{ij} := \left\{ \begin{array}{rlr} \cot\theta_k^{ij} + \cot\theta_l^{ji} & [v_i, v_j] \notin \partial(S, T) & [v_i, v_j] = [v_i, v_j, v_k] \cap [v_j, v_i, v_l] \\ \cot\theta_k^{ij} & [v_i, v_j] \in \partial(S, T) & [v_i, v_j] \in \partial[v_i, v_j, v_k] \end{array} \right. \tag{7.4.3}$$

The Hessain matrix $H = (h_{ij})$, where

$$h_{ij} = \left\{ \begin{array}{lll} -w_{ij} & v_i \sim v_j & i \neq j \\ 0 & v_i \not\sim v_j & i \neq j \\ \sum_k w_{ik} & & i = j \end{array} \right. \tag{7.4.4}$$

In order to compute the conformal metric with prescribed curvature, we can optimize the Yamabe energy using Newton's method.

7.4.2 Optimal Transportation Map

Alexandrov Map

Assume Ω is a finite planar domain with measure density ρ. According to Theorem 25, the A-Map can be obtained by minimizing the convex energy in Eqn. 7.3.4. In practice, we can use Newton's method for the optimization. The gradient of the energy is given by

$$\nabla E(\mathbf{h}) = (\frac{\partial E}{\partial h_1}, \frac{\partial E}{\partial h_2}, \cdots, \frac{\partial E}{\partial h_n})^T = \mu - \mathbf{w}(\mathbf{h}). \tag{7.4.5}$$

The Hessian matrix has an explicit geometric meaning, and is given by Eqn.7.3.6 and Eqn.7.3.7.

Initialization Suppose we are given the domain Ω and density ρ, the point set with measure (P,μ). By translating and scaling, P could be inside Ω, $P \subset \Omega$. At the beginning, we set each power weight h_i to be 0, and compute the power diagram $D(P,\mu)$ and the Delaunay triangulation $T(P,\mathbf{h})$. In this scenario, $D(P,\mathbf{h})$ is a conventional Voronoi diagram.

Step Length Selection Suppose at the k-th step in the optimization, the power weight vector is $\mathbf{h}^k$, and all Voronoi cells $W_i(\mathbf{h}_k)$ are non-empty. Then the Hessian matrix in Eqn.7.3.6 is positive definite on the space $\{\mathbf{h} | \sum_{i=1}^n h_i^k = 0\}$. We solve the linear system using the Conjugate gradient to get H^{-1}. At the $k+1$-step, we initialize the step length parameter λ as 1, and update the power weight vector

$$\mathbf{h}^{k+1} = \mathbf{h}^k - \lambda H^{-1} \nabla E(\mathbf{h}^k). \tag{7.4.6}$$

Then we compute the power diagram $D(P,\mathbf{h}^{k+1})$. If any Voronoi cell $W_i(\mathbf{h}^{k+1})$ disappears, then the Hessian matrix will be degenerated. In this case, we shrink the step length parameter λ to be half, $\lambda \leftarrow 1/2\lambda$. Then we reset $\mathbf{h}^k$ using the formula in Eqn. 7.4.6 and test again, until all Voronoi cells in $D(P,\mathbf{h}^{k+1})$ are non-empty.

Algorithm 5 gives the implementation details.

7.5 Experimental Results

Data Preparation All the facial surfaces are acquired using structured light 3D scanner based on phase shifting [73], which can capture 3D dynamic surfaces with high resolution 480 × 640 at high frame rate 30 FPS. We also tested our algorithm in various shapes. Figure 7.8, 7.9, 7.10 are from public 3D repositories [2]. And the brain surface in Figure 7.11 are acquired as part of the Alzheimer's Disease Neuroimaging Inituative (ADNI) [40], and segmented using FreeSurfer [24]. The surfaces are represented as triangular meshes. The surfaces have been preprocessed to fill holes caused by occlusions, and low pass filtering to remove random noises. For the human face models, which is genus zero with one open boundary, the boundaries are original, without any modification on the raw scanned data. For models in figure 7.8, 7.9, 7.10 and 7.11, which are originally genus zero surface with no boundary, we cut a small hole on the surface to make it have

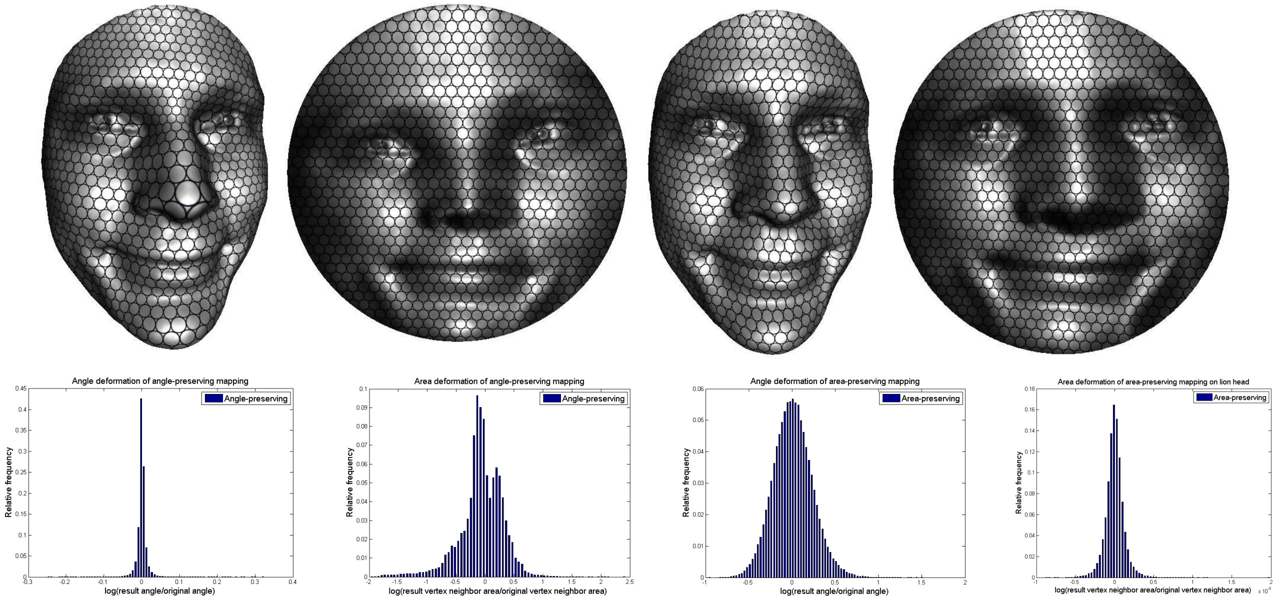

Figure 7.3: Riemann mapping and area-preserving of Alex' face surface with a smile.

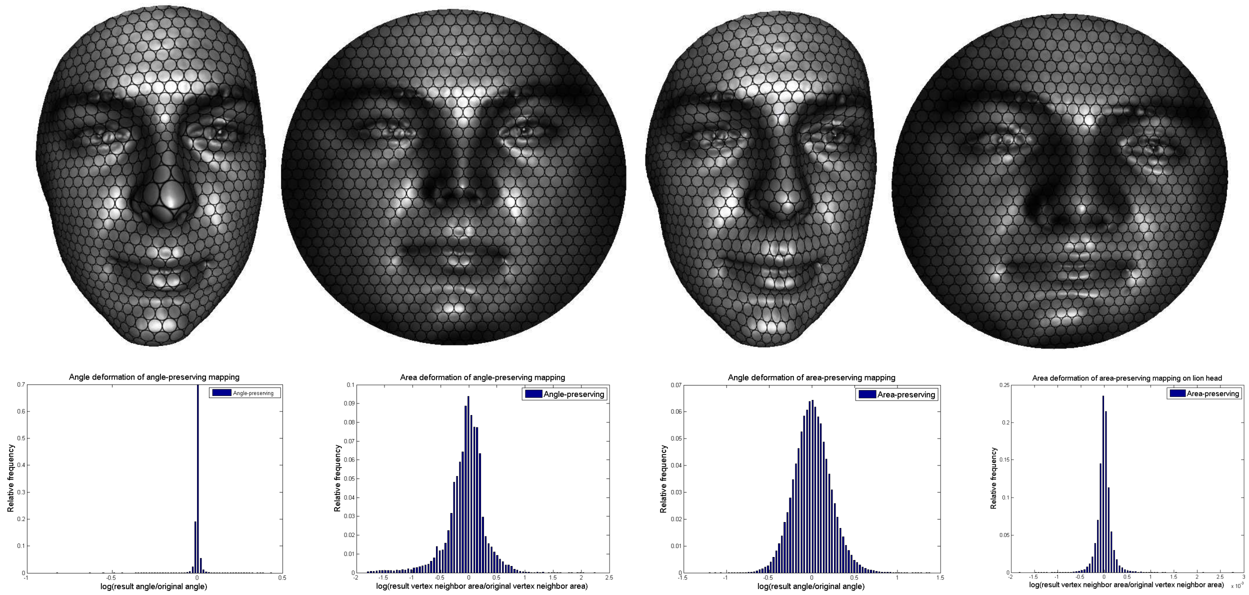

Figure 7.4: Riemann mapping and area-preserving of David's face surface.

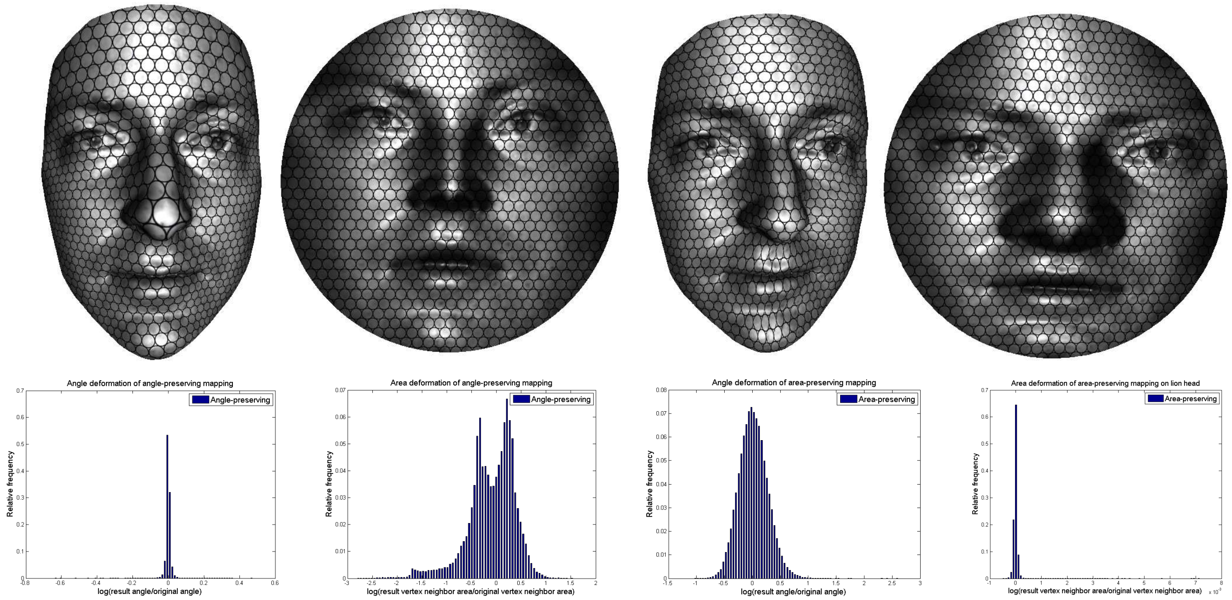

Figure 7.5: Riemann mapping and area-preserving of Luke’s face surface.

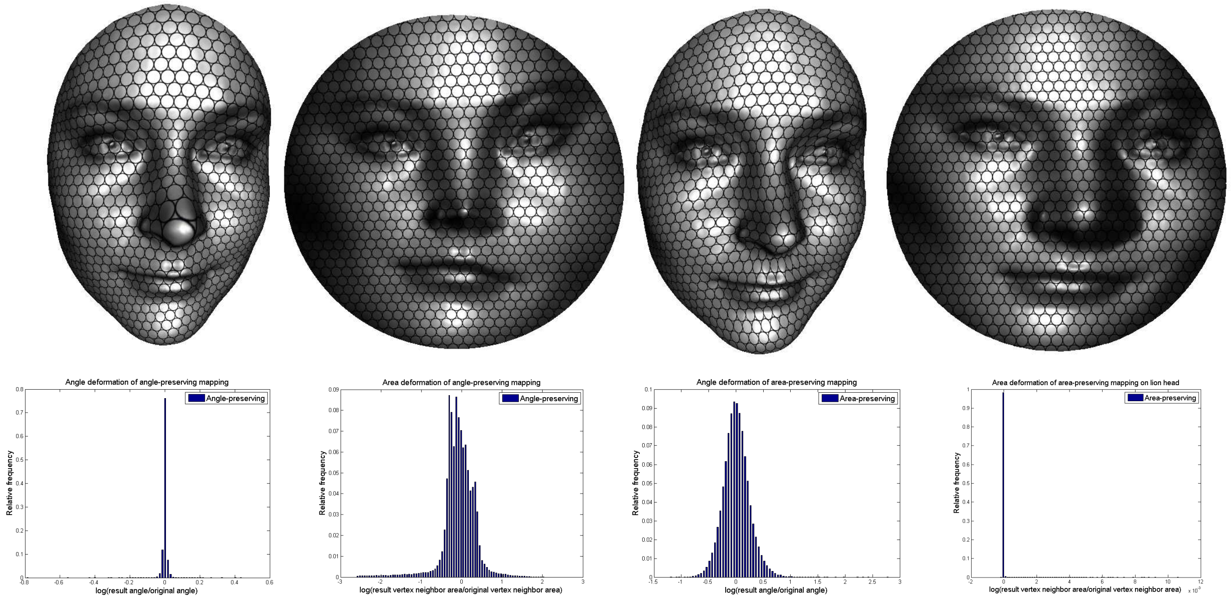

Figure 7.6: Riemann mapping and area-preserving of Sophie’s face surface without any expression.

Algorithm 5: Alexandrov Map (A-Map)

```
Input: A convex parameter-space $\Omega$; a planar point set with measure $(P,\mu)$, $\mu_i > 0$,
    $\sum_{i=1}^{n} \mu_i = Area(\Omega)$;
Output: The power weight vector $\mathbf{h}$, where $h_i$ associated with $p_i$ determines the optimal
    transport map.

    Scale and translate $P$, such that $P \subset \Omega$.
    Initialize power weight vector $\mathbf{h} \leftarrow (0,0,\cdots,0)$.
    Compute the power diagram $D(\mathbf{h})$ and power Delaunay triangulation $T(\mathbf{h})$.
    Calculate the cell areas $\mathbf{w}(\mathbf{h})$.
    while Convergence is not reached do
        Compute gradient $\nabla E(\mathbf{h})$ using Eqn.7.4.5.
        Calculate the lengths of edges in the diagram and triangulation to form the Hessian matrix
        using Eqn.7.3.6.
        Initialize $\lambda \leftarrow 1$
        Update $\mathbf{h} \leftarrow \mathbf{h} - \lambda H^{-1} \nabla E(\mathbf{h})$.
        Compute $D(\mathbf{h})$, $T(\mathbf{h})$ and $\mathbf{w}(\mathbf{h})$.
        while $\exists w_i(\mathbf{h}) == 0$ do
            $\mathbf{h} \leftarrow \mathbf{h} + \lambda H^{-1} \nabla E(\mathbf{h})$.
            $\lambda \leftarrow 1/2\lambda$
            $\mathbf{h} \leftarrow \mathbf{h} - \lambda H^{-1} \nabla E(\mathbf{h})$.
            Compute $D(\mathbf{h})$, $T(\mathbf{h})$ and $\mathbf{w}(\mathbf{h})$.
        end while
    end while
    return $\mathbf{h}$.
```

one open boundary. In order to improve the numerical stability, the surfaces have been remeshed by Delaunay refinement on the conformal parameter domain.

Implementation The algorithms have been implemented using generic C++ on windows plat form. The linear systems are solved using Eigen numerical package [33]. All the experiments are conducted on a PC with 3.60GHz CPU, 4.00 GB memory. We collect 3D human facial surfaces with different expressions, and use 6 facial surfaces for the registration testing. The computational times for the Riemann mappings and optimal transportation maps are summarized in Tab 7.1.

Analysis The angle-preserving mappings and area-preserving mappings for different surfaces are illustrated in Fig. 7.3, 7.4, 7.5, 7.6, 7.7, 7.8, 7.9, 7.10 and 7.11 respectively. The histograms of angle ratios and area ratios are also shown in these figures. From the histograms, we can verify the conformality of the discrete conformal mappings and the area-preservation property of the discrete optimal transportation maps. The optimal transport mapping from the Riemann mapping image to the canonical planar disk are shown in Fig. 7.12, 7.13, 7.14, 7.6, 7.16. The shape signatures are

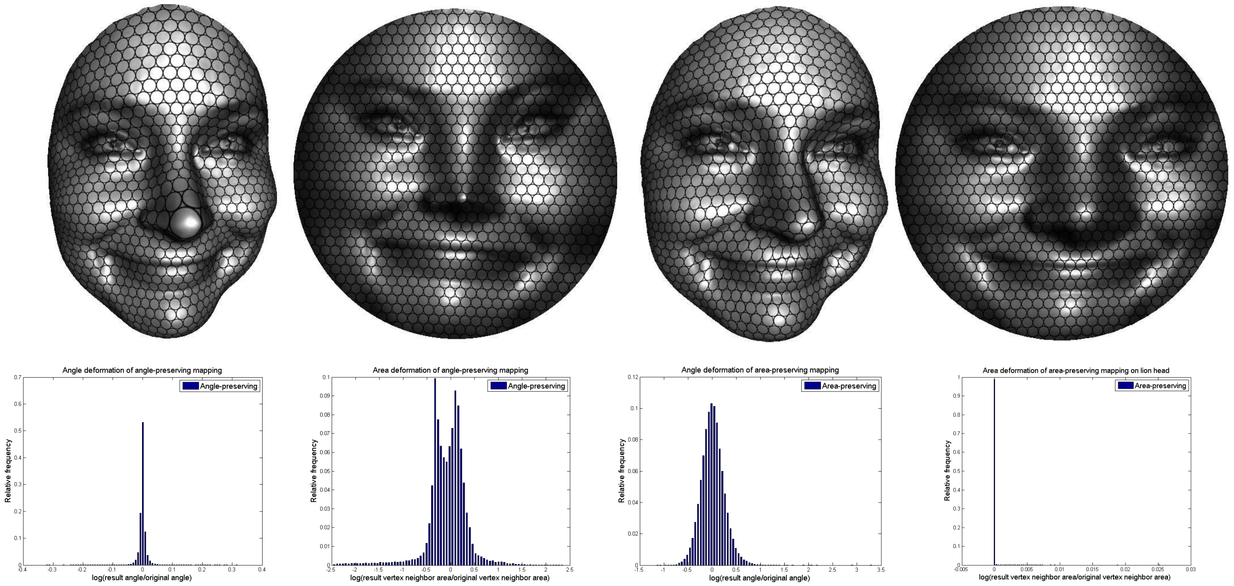

Figure 7.7: Riemann mapping and area-preserving of Sophie's face surface with a smile.

also illustrated in these figures. The mapping $\eta : \mathbb{D} \to \mathbb{D}$ are color encoded and shown in frame (c), the real and imaginary components of η are encoded in the red and green channels. The mean curvature H is also color encoded and show in frame (d). In practice, the two signatures can be combined to one color image.

The shape distances among all the surfaces are listed in Tab 7.2. The η distances are shown above the diagonal, the H distances are below the diagonal. The η distance solely depends on the Riemannian metric. The H distance also depends on the embedding. From the table, we can see, in terms of both η and H distances, the closest pairs of shapes are the surfaces of the same face with different expressions. This validates the efficacy of the proposed shape distance.

7.6 Conclusions

This chapter proposes a novel surface signature and shape distance based on Riemann mapping and optimal transportation map. The surface is conformally mapped onto the unit planar disk by the Riemann mapping ϕ, then ϕ induces a measure on the disk $e^{2\lambda}dxdy$. Then the unique optimal transport mapping η is computed, which transports the new measure to the canonical measure. Then the optimal transport mapping η combined with the mean curvature of the surface H form the signature of the surface. (η, H) with the boundary condition can determine the surface unique up to a rigid motion in $\mathbb{R}^3$. The L^2 distance between the signatures gives the shape distance. The Riemann mapping is computed using discrete surface Ricci flow; the optimal transport map is carried out by convex optimization. The method has been tested on human facial surfaces with different expressions accquired by phase shifting 3D scanner. The experimental results demonstrate

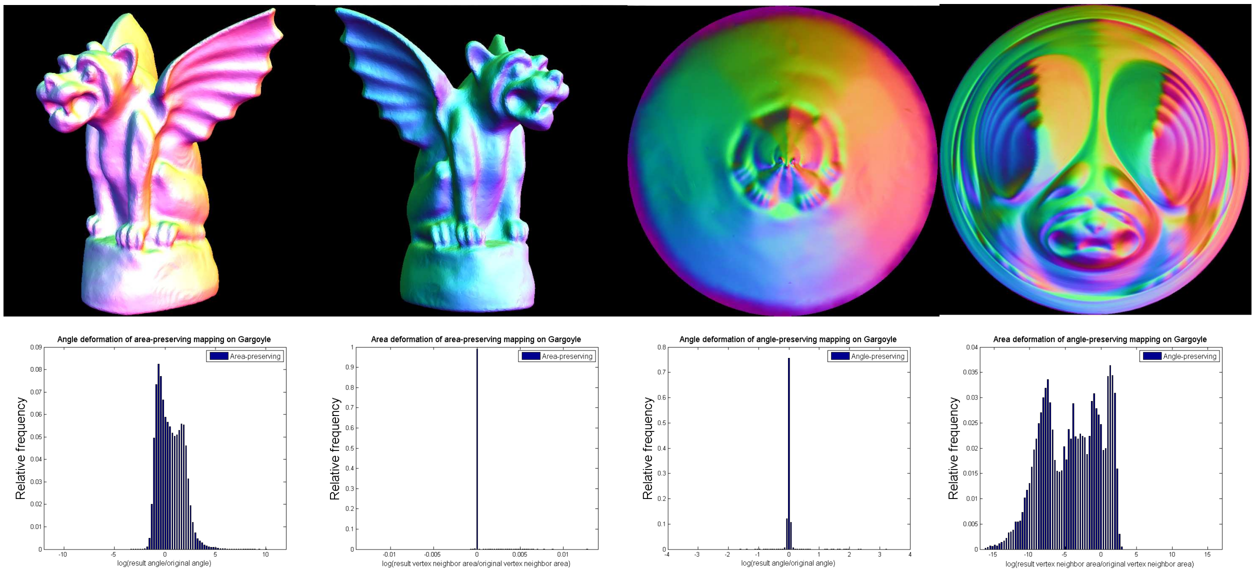

Figure 7.8: Riemann mapping and area-preserving of the Gargoyle model.

the efficiency and efficacy of our proposed method.

From differential geometry theory, the original surface can be fully reconstructed from λ, H and the boundary condition. We will report the computational algorithms for this in future submissions. We will also test our method on large scale geometric database for the purposes of facial recognition and expression recognition, and generalize the method for surface registration and tracking.

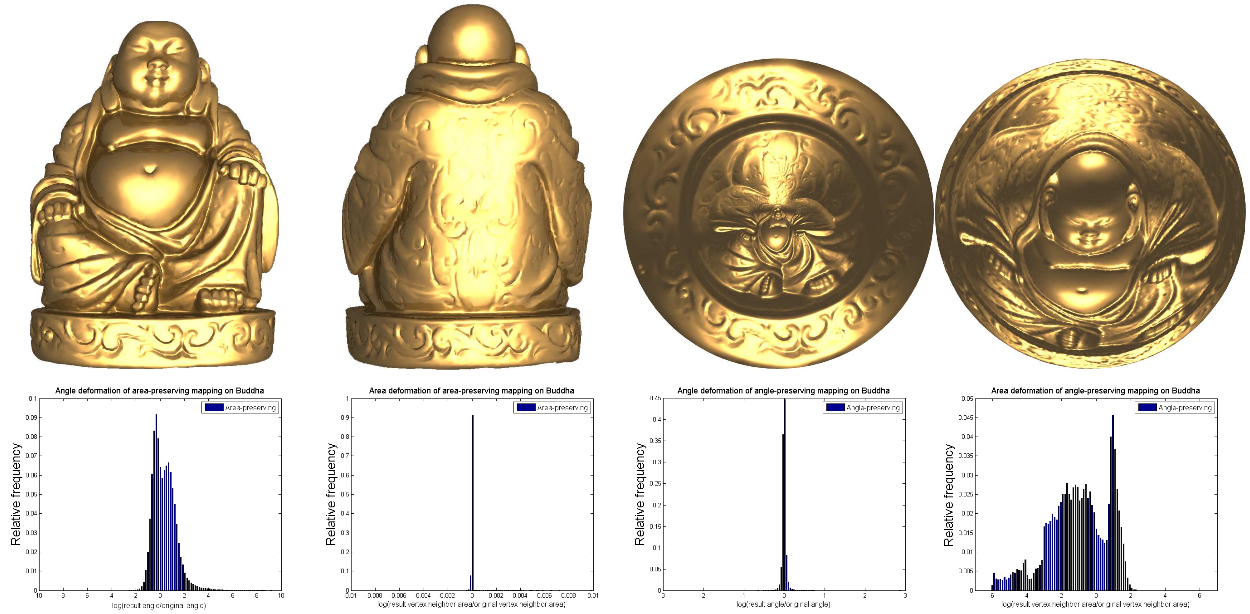

Figure 7.9: Riemann mapping and area-preserving of the Buddha model

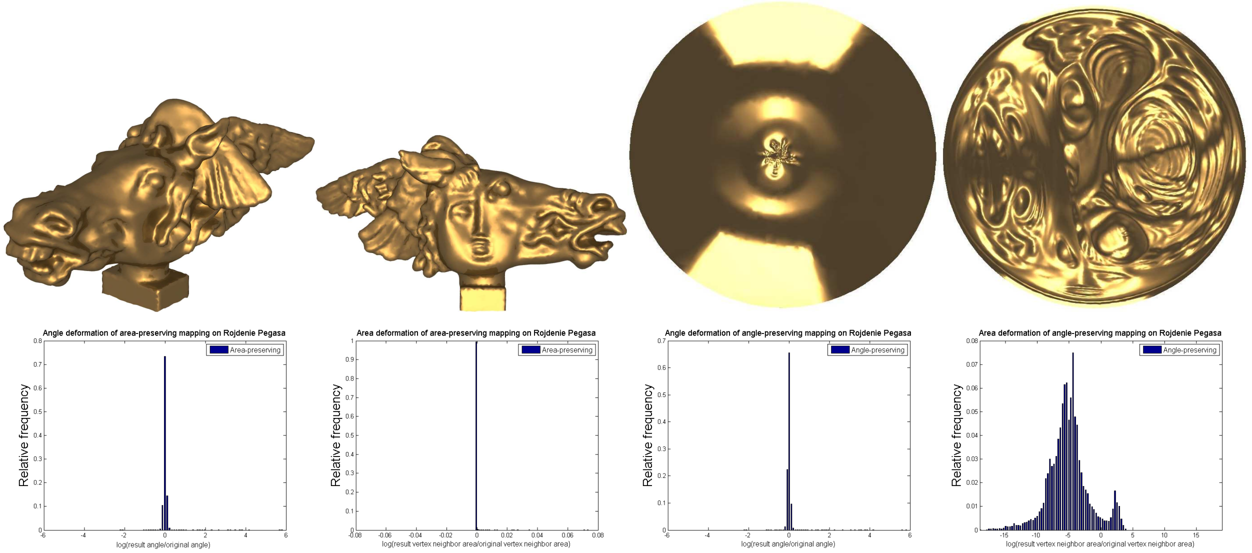

Figure 7.10: Riemann mapping and area-preserving of the Pegasa model

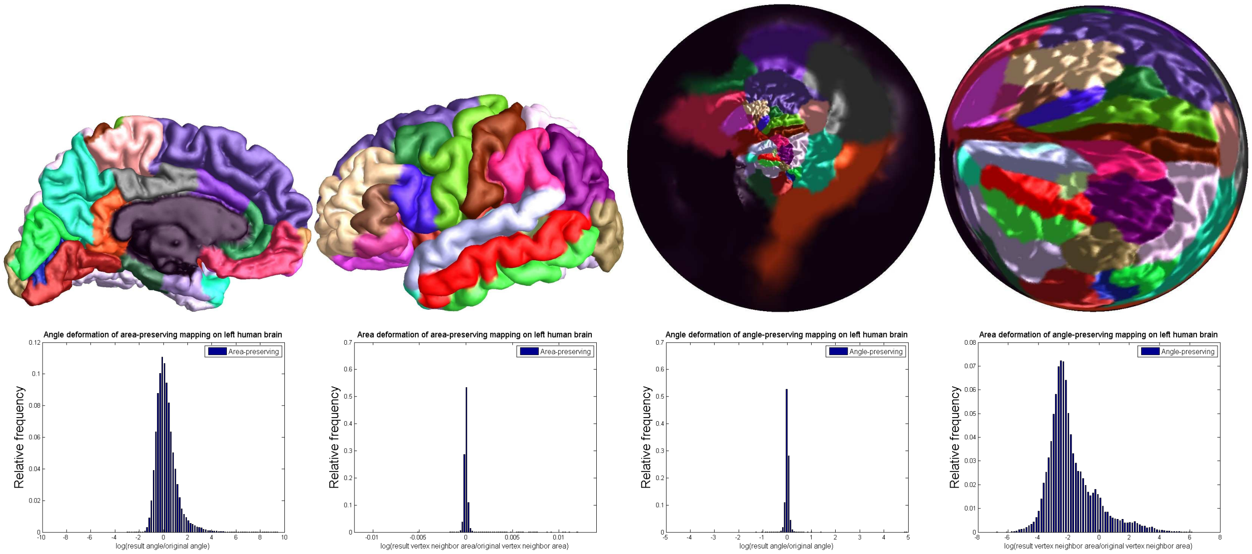

Figure 7.11: Riemann mapping and area-preserving of the left human brain model.

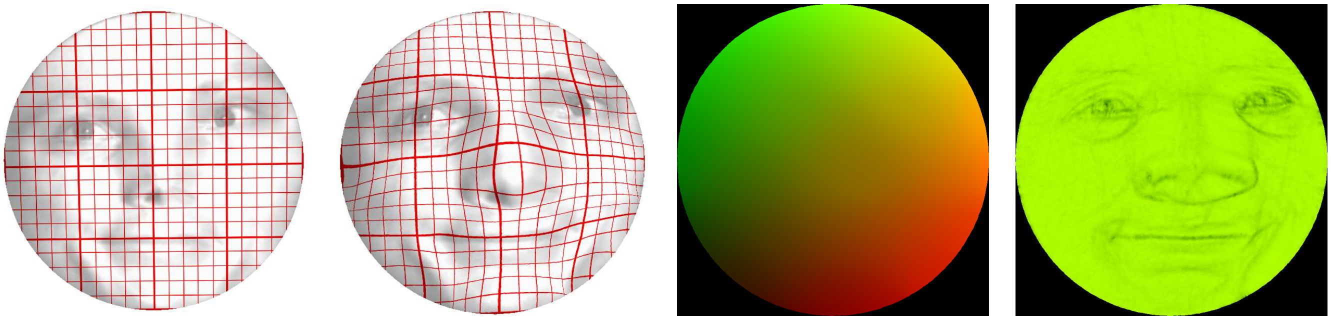

(a) Riemann mapping image

(b) Optimal Transport map image

(c) η signature

(d) H signature

Figure 7.12: Optimal transport mapping for Alex' face surface with a smile from (a) to (b), and the signature (η, H) .

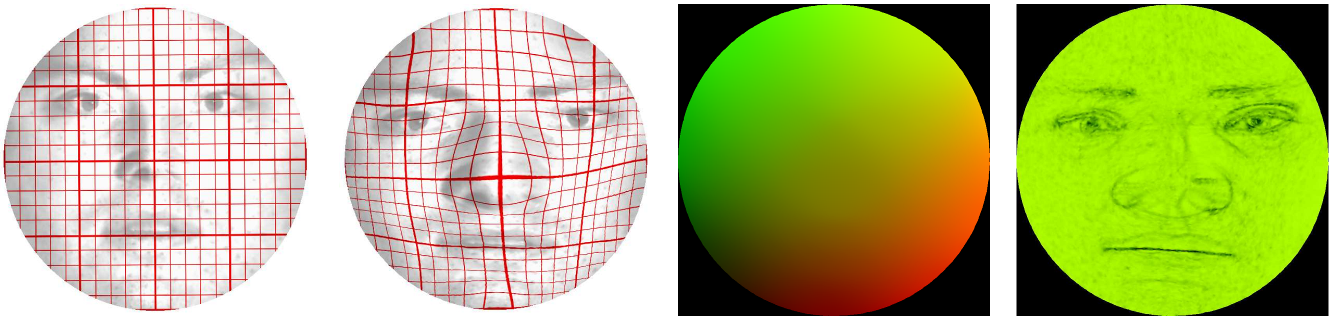

(a) Riemann mapping image

(b) Optimal Transport map image

(c) η signature

(d) H signature

Figure 7.13: Optimal transport mapping for Luke's face surface from (a) to (b), and the signature (η, H) .

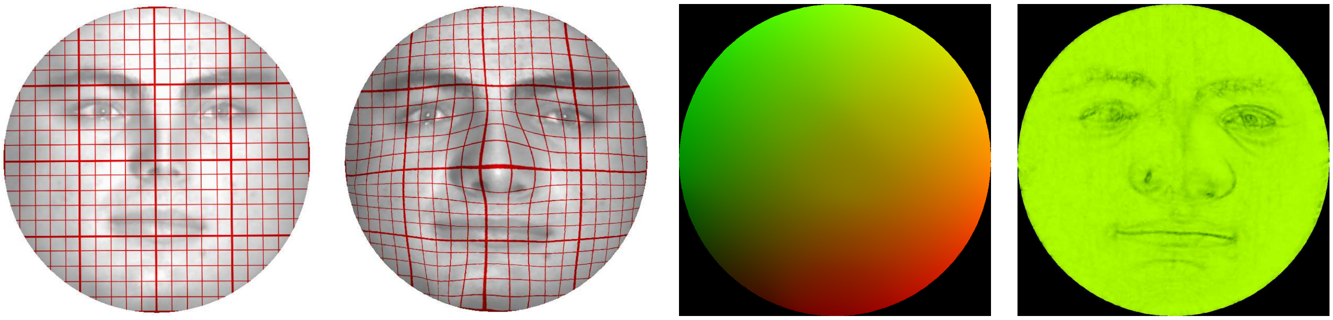

(a) Riemann mapping image

(b) Optimal Transport map image

(c) η signature

(d) H signature

Figure 7.14: Optimal transport mapping for David's face surface from (a) to (b), and the signature (η, H) .

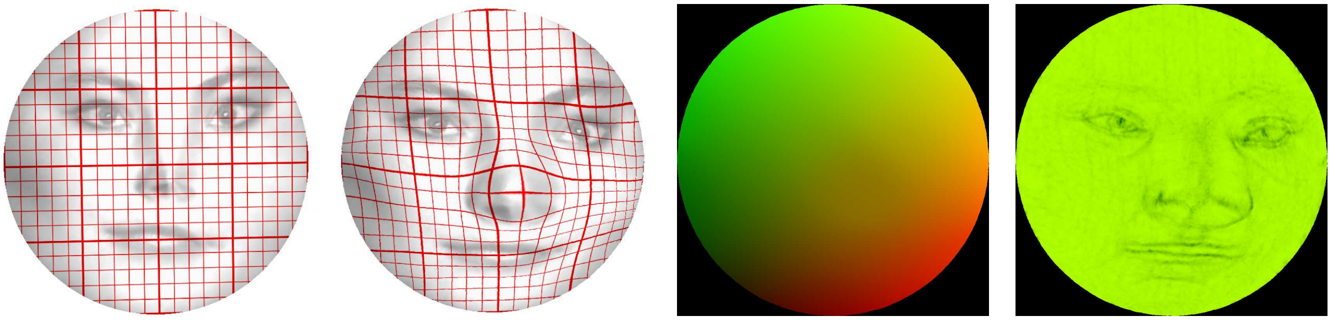

(a) Riemann mapping image

(b) Optimal Transport map image

(c) η signature

(d) H signature

Figure 7.15: Optimal transport mapping for Sophie's face surface without any expression from (a) to (b), and the signature (η, H) .

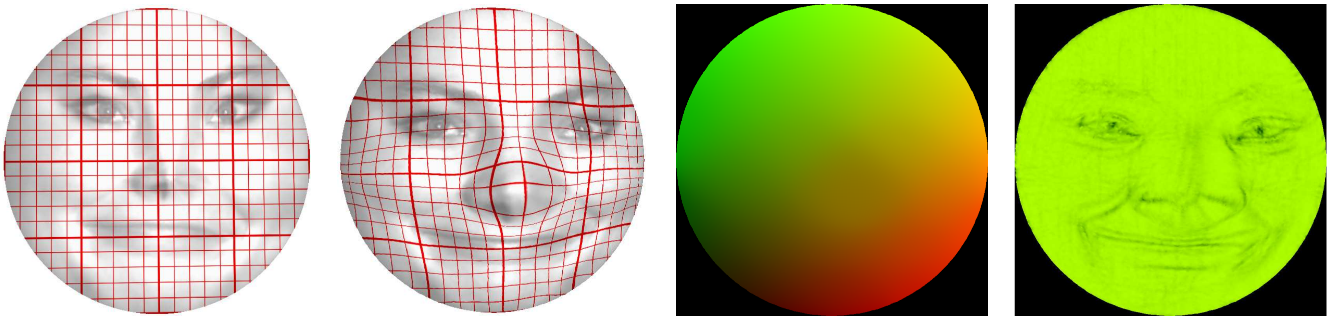

(a) Riemann mapping image

(b) Optimal Transport map image

(c) η signature

(d) H signature

Figure 7.16: Optimal transport mapping for Sophie's face surface with a smile from (a) to (b), and the signature (η, H) .

Table 7.1: Computation Time.

Name	# Faces	# Vertices	Riemann Mapping (Sec)	Opt.Tran.Map (sec)
Alex Calm	42184	21326	63.03	24.2
Alex Smile	42238	21364	65.9	25.0
Sophie Calm	41587	21043	73.2	24.8
David	42423	21458	74.5	24.8
Luke	42281	21371	68.5	24.1
Sophie Smile	42518	21495	79.8	24.5
Buddha	101522	50365	122.3	55.2
Gargoyle	105419	50455	136.8	59.4
Pegasa	120548	61361	141.9	65.2
Brain	101879	50898	125.4	60.7

Table 7.2: Shape Distances (Above the diagonal: η distance; below the diagonal H distance.)

	Alex Calm	Alex Smile	David	Luke	Sophie Calm	Sophie Smile
Alex Calm	0	0.0048959	0.020940	0.040434	0.031219	0.028863
Alex Smile	0.013269	0	0.017960	0.038700	0.030650	0.026525
David	0.024743	0.023980	0	0.011080	0.010979	0.0079039
Luke	0.044247	0.045730	0.038215	0	0.0094910	0.0089562
Sophie Calm	0.025095	0.027394	0.027763	0.043286	0	0.0076297
Sophie Smile	0.023973	0.023640	0.027429	0.042514	0.019495	0

Chapter 8

Application III: Interactive Visibility Retargeting in VR

In Virtual Reality, immersive systems such as the CAVE provide an important tool for the collaborative exploration of large 3D data. Unlike head-mounted displays, these systems are often only partially immersive due to space, access or cost constraints. The resulting loss of visual information becomes a major obstacle for critical tasks that need to utilize the users' entire field of vision. We have used Ricci Flow method as conformal visualization technique.that establishes a conformal mapping between the full 360 degree field of view and the display geometry of a given visualization system. The mapping is provably angle-preserving and has the desirable property of preserving shapes locally, which is important for identifying shape-based features in the visual data. We apply the conformal visualization to both forward and backward rendering pipelines in a variety of retargeting scenarios, including CAVEs and angled arrangements of flat panel displays. In contrast to image-based retargeting approaches, our technique constructs accurate stereoscopic images that are free of resampling artifacts. Our user study shows that on the visual polyp detection task in Immersive Virtual Colonoscopy, conformal visualization leads to improved sensitivity at comparable examination times against the traditional rendering approach. We also develop a novel user interface based on the interactive recreation of the conformal mapping and the real-time regeneration of the view direction correspondence.

We have developed a visualization approach that utilizes conformal mapping to modify scene geometries or viewing rays at runtime, depending on the rendering modality. As a result, the full virtual environment can be displayed on a partially-immersive visualization platform, for example a 5-sided CAVE, without the artifacts typically associated with image-based retargeting approaches. In mathematics, the conformal map is an angle preserving function that describes a mapping between two Riemannian surfaces [69]. Intuitively, it allows us to map the geometry of the fully-immersive 6-sided CAVE to an arbitrary configuration of display surfaces that is topologically equivalent to a disk, such as a 5-sided CAVE or a non-planar arrangement of flat panel displays. This mapping is then used to transform the viewing directions during rendering with ray tracing, for example. The main advantage of using a conformal map to define the transformation is the guarantee that shapes will be preserved locally even though distances will not be. This is particularly beneficial for the exploration of medical data, such as in Virtual Colonoscopy (VC) where potentially cancerous polyps are detected by the radiologist based on their shape.

8.1 Discrete Ricci Flow Algorithm for CAVE

Suppose Σ is a triangle mesh embedded in $\mathbb{R}^3$. We associate each vertex v_i with a circle (v_i, γ_i) where γ_i equals the minimal length of any edge in the immediate neighborhood of v_i. Then we compute the intersection angle Θ_{ij} such that the circle packing metric is as close to the induced Euclidean metric as possible.

We compute the curvature at each vertex v_i and adjust the conformal factor u_i in proportion to the difference between the target curvature $\bar{K}_i$ and the current curvature K_i. Then, we update the metric, recompute the curvature, and repeat this procedure until the difference between the target curvature and the current curvature is less than the given threshold. Alg. 6 summarizes the computational steps and more details can be found in the work of Jin et al. [43].

Algorithm 6: Discrete Ricci Flow

```
Input: Triangular mesh $\Sigma$, target curvature for each vertex $\bar{K}_i$, error threshold $\varepsilon$.
Output: Discrete metric (edge lengths) satisfying the target curvature.
$\mathbf{u} = [u_i], \mathbf{v} = [v_i]$ for $\mathbf{u}, \mathbf{v} \leftarrow 0$
while true do
    Compute edge length $l_{ij}$ for edge $[v_i, v_j]$:
    $l_{ij} = e^{u_i} + e^{u_j} + 2\cos\phi_{ij} e^{u_i + u_j}$
    Compute the corner angle $\theta_i^{jk}$ in triangle $[v_i, v_j, v_k]$:
    $\theta_i^{jk} = \cos^{-1} \frac{l_{ij}^2 + l_{ki}^2 - l_{jk}^2}{2 l_{ij} l_{ki}}$
    Compute the curvature $K_i$ at $v_i$:
    $K_i = \begin{cases} 2\pi - \sum_{f_{ijk} \in F} \theta_i^{jk}, & v_i \notin \partial\Sigma \\ \pi - \sum_{f_{ijk} \in F} \theta_i^{jk}, & v_i \in \partial\Sigma \end{cases} \quad \mathbf{K} = [K_i]$
    if max $|\bar{K}_i - K_i| < \varepsilon$ then
        return the discrete metric $l_{ij}$
    end if
    Update $\mathbf{u}$:
    Compute the Hessian Matrix $H$, $H_{ij} = \frac{\partial K_i}{\partial u_j}$
    $\mathbf{u} \leftarrow \mathbf{u} - H^{-1}(\bar{\mathbf{K}} - \mathbf{K})$
end while
```

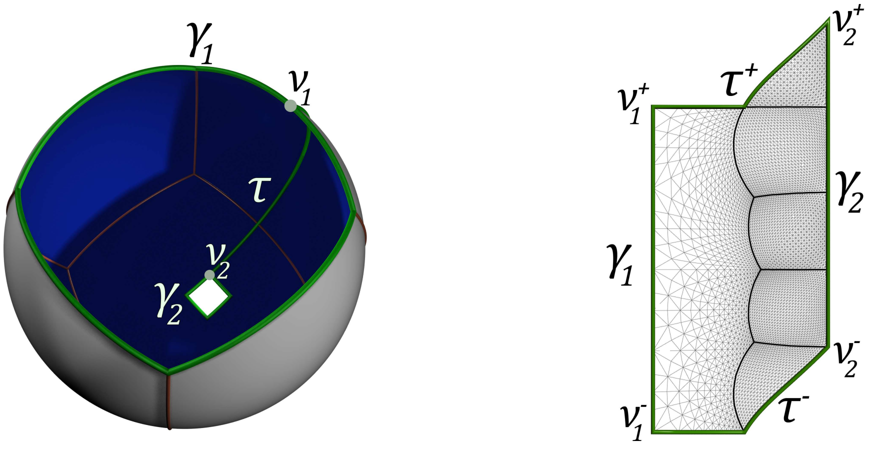

a.Cutting the geometry **b**.Gemetry flattening

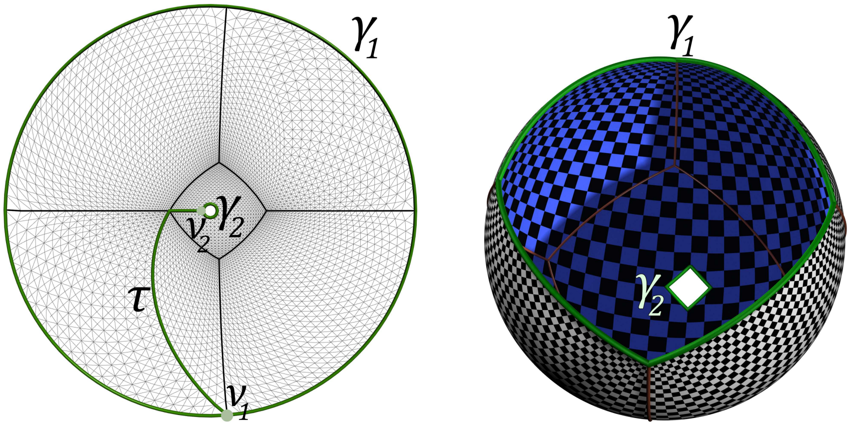

c. Planar strip mapped to annulus **d**.Conformal mapping result

Figure 8.1: Riemman Mapping Algorithm.

8.2 Riemann Mapping: CAVE

Figure 8.1 illustrates the algorithm for computing the Riemann mapping. We remove a face from the mesh Σ to convert it to a topological cylinder (Figure 8.1a), resulting in the creation of a new boundary γ_2. The target curvature for both the interior and the boundary vertices is set to zero. The Ricci flow described in Alg. 6 produces a flat cylinder that is periodically embedded in the complex plane (Figure 8.1b). Each period of the embedding is a rectangle and the original boundaries γ_1 along the cut face and γ_2 are aligned with the imaginary axis in the complex plane. The cylinder is then mapped to the unit disk with the hole in the center of the image by the exponential map e^z (Figure 8.1c). Figure 8.1d illustrates the mapping by texture mapping a checkerboard pattern back on the cut mesh. As a final step, the removed face is inserted back into the mesh, yielding the conformal mapping on the original mesh.

8.3 Practical Application of Discrete Ricci Flow Algorithm

The previous sections introduce the theoretical foundation of the Discrete Ricci flow algorithm, which is the base algorithm in our conformal visualization technique. Using the 5-sided CAVE as an example, we consider all the possible view directions mapped onto a unit sphere for a reference position at the center of the environment. This sphere is cut at the position that corresponds to the center of the missing surface (Fig. 8.2C) and towards the four corners. The top edges of the CAVE are also mapped to the sphere (Fig. 8.2A) and they define the visibility boundary $\partial\Sigma$ for the central CAVE position. We apply the Discrete Ricci flow to compute the conformal maps for both spheres, which are then aligned to provide a 1-to-1 mapping between the two surfaces (see Fig. 8.2B and Fig. 8.2D). Using this mapping, the full set of viewing directions defined over the 6-sided CAVE is then projected onto the geometry corresponding to the 5-sided CAVE. We then encode the viewing directions into a cube map which can be sampled efficiently during rendering. Although our rendering framework can utilize conformal maps produced with any computational algorithms, the automation, robustness and efficiency of the Ricci flow provide an advantage for quickly generating the mappings between the different display topologies.

8.3.1 Implementation Details

Our conformal visualization utilizes an efficient pipeline for generating the conformal mapping at interactive speeds. The input is a user-specified rendering target, such as an *n*-sided CAVE or an arrangement of displays, as well as a set of parameters that control the accuracy of the generated maps.

8.3.2 Mesh Templates

Our mesh processing toolkit utilizes a half-edge data structure to explicitly represent the mesh connectivity information. We start by generating the templates for the source and target visibility meshes. Although the conformal mapping is performed over the visibility spheres, the geometries at this stage are simple cubes in order to facilitate a more intuitive definition of the visibility boundaries and the cuts. Fig. 8.3 and 8.5 illustrate the templates for the 5-sided and the 4-sided CAVE respectively. In both cases, the templates are parameterized with a reference point whose projection on the walls (shown as green spheres) define the intersection points of the cut.

A similar template can be defined for the 3-sided CAVE as well (Fig. 8.4(a)). However, because of the increased length of the cut, mapping to an arrangement of displays is not practical as the conformal visualization would introduce significant distortion artifacts. For a target mesh similar to Fig. 8.4(c), we map only a hemisphere of the original viewing directions (Fig. 8.4(b)).

8.3.3 Mesh Processing

The source and target meshes are processed independently and in parallel to obtain the conformal mapping. The first step is to triangulate and refine the template to the desired granularity so that the computations can be performed with sufficient accuracy. We achieve this by an edge split operation

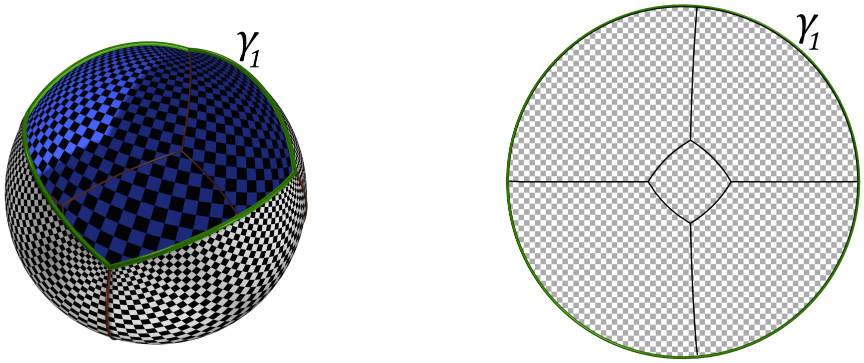

a.5-sided CAVE mapped to the sphere **b**.Conformal mapping of a

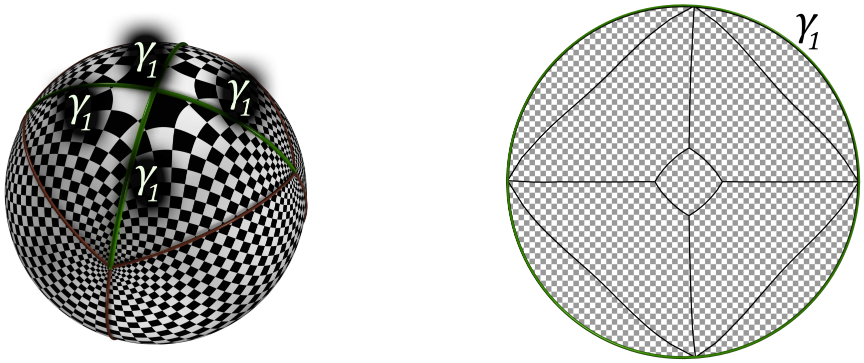

c. 6-sided CAVE mapped to the sphere **d**.6-sided CAVE mapped to the sphere

Figure 8.2: Algorithm for conformal mapping between a 5-sided CAVE and a 6-sided CAVE

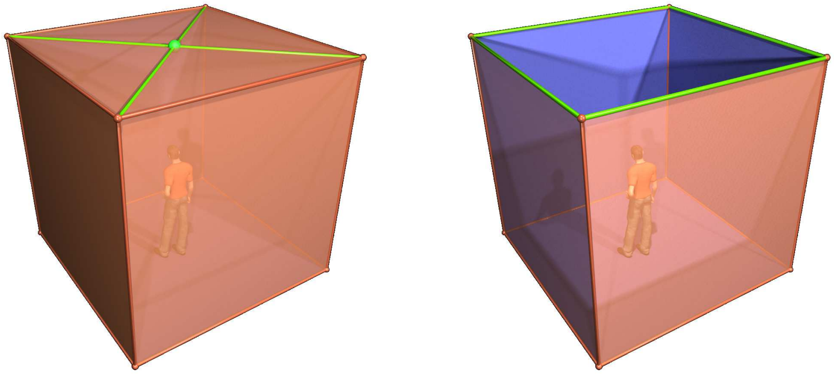

a.Cut source mesh **b**.Target mesh

Figure 8.3: Template meshes for a 5-sided CAVE

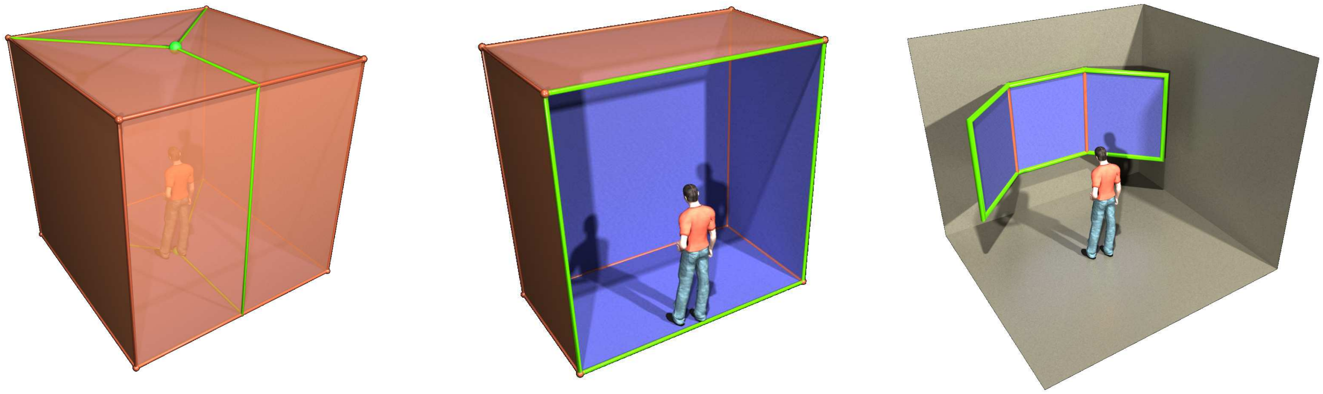

a.Cut source **b**.Partial visibility source **c**.Target mesh

Figure 8.4: Template meshes for a 3 screen target. The cut in (a) is suitable for the 3-sided CAVE. For an arrangement of flat-panel displays (c), the cut in (b) reduces the distortion effects.

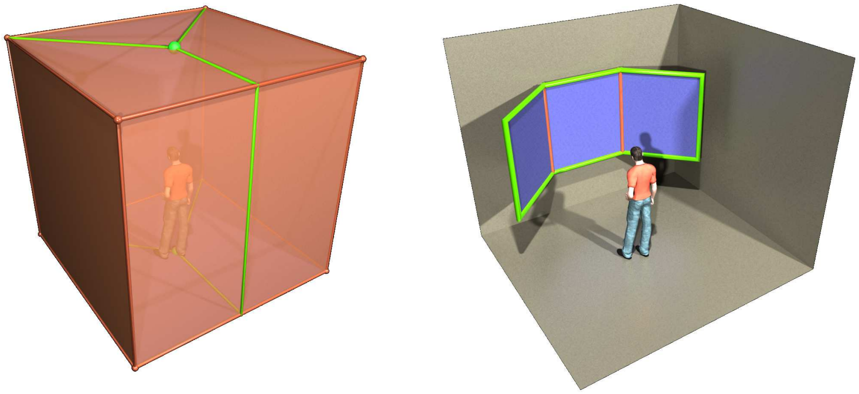

a.Cut source mesh **b**.Target mesh

Figure 8.5: Template meshes for a 4-sided CAVE.

where a new vertex is iteratively introduced at the mid-point of each edge, doubling the number of triangles. The process is performed until the edge length falls below a user-specified threshold. In our experiments, edge sizes corresponding to $20cm$ in the real-world allow for sufficiently accurate conformal maps to be generated at interactive speeds, while granularity below $5cm$ yields only marginal improvements. In addition to the performance constraints, the edge threshold also depends on the resolution of target displays.

At this point, each mesh is finely tessellated and contains a single closed boundary. Next, we remove a triangle so that the resulting mesh can be mapped to the complex plane (see Sec. 8.2). We select the triangle that is at the center of the mesh, or farthest from the original boundary. The same triangle is removed from both the source and target meshes. We also store a 3-vertex correspondence between the meshes, which will be used to align the planar projections of the conformal maps. These vertices are selected from among the common vertices on the original closed boundaries. We then map the cube geometry to a sphere by the *direction map*

$$p \to \frac{p-c}{|p-c|},$$

where p is a point on the cube and c is the center of the cube.

The following step computes the shortest path τ along the edges of the mesh between the original boundary γ_1 and the newly created boundary γ_2 at the center of the mesh. Since the embedding in the complex plane is periodic, the exact shape of τ is not important; however, for consistency, we enforce that the same cut is made on both the source and the target meshes.

Next, the discrete Ricci flow algorithm presented in Sec. 8.1 is used to compute the conformal mapping to the unit disc. This mapping is stored as UV coordinates at the vertices of the two meshes. Fig. 8.2 illustrates the results of this step. The Möbius transformation is then used to align the two conformal maps based on the vertex correspondence stored earlier. We use special Möbius transformations to map the point triplets to $1, i$ and -1 on the unit circle, which aligns the corresponding markers. Suppose $\{p, q, r\}$ are three markers on the unit circle and

$$\eta_1(z) = \frac{z-p}{z-q}\frac{r-q}{r-p}$$

maps them to $\{0, \infty, -1\}$. Let

$$\eta_2(z) = \frac{1+i}{2}\frac{z-1}{z-i},$$

then $\eta_2^{-1} \circ \eta_1$ is the desired Möbius transformation, which maps $\{p, q, r\}$ to $\{1, i, -1\}$. Fig. 8.2(b) and Fig. 8.2(d) show the result after the alignment.

8.4 Results

8.4.1 Visualizing the Conformal Transformation

We first demonstrate the visual properties of our technique on a unit sphere with a checkerboard texture. In Fig. 8.6, the virtual camera is positioned at the center of the sphere so that the two

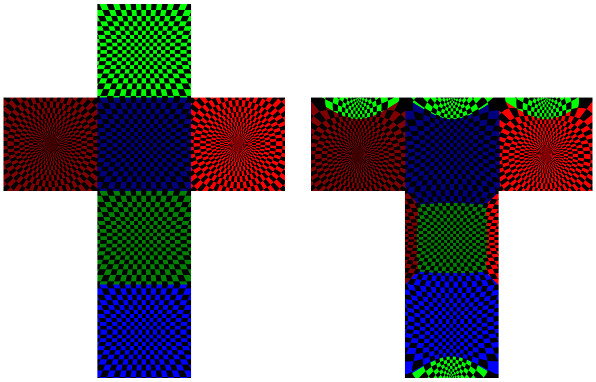

a.6-sided CAVE **b**.5-sided CAVE

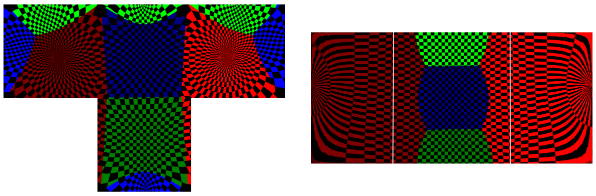

c. 4-sided CAVE **d**.3-sided CAVE

Figure 8.6: Raytracing of a checkerboard sphere with conformal visualization on different display targets. The layout for (a)-(c) is in the standard vertical cross format and the color coding is defined for the original walls in the 6-sided CAVE configuration (blue for front/back, red for left/right, green for top/bottom). For(d) we show the output of all 3 displays side by side.

poles of the texture are shown on the left and the right displays. Fig. 8.6(b) shows the results of our conformal visualization and demonstrates how the visual information originally shown on the top screen is instead rendered on the left, front, right and back screens. In Fig. 8.6(c) we apply the T_{ray} transformation computed for the 4-sided CAVE mesh target (see Fig. 8.5(b)). The result is that compared to the 5-sided case, the visual information from the back screen is pushed toward the bottom and the side screens.

We also visualize the conformal transformation for the scenario presented in Fig. 8.4 where the 180 degree field of view is mapped to an arrangement of workstation monitors. The monitor setup is modeled after the Samsung MD230X6 array of 3×2 high resolution thin bezel monitors. This represents a challenge for the conformal mapping since with an aspect ratio of $2.66 : 1$, the boundaries of the source and target mesh are significantly different. Nevertheless, our approach produces an angle-preserving conformal transformation that enhances the field of view of the user.

User interactions with the virtual scenes often involve navigation in 3D space. We demonstrate this aspect of our visualization technique with a checkerboard tunnel. Fig. 8.7(a) illustrates the

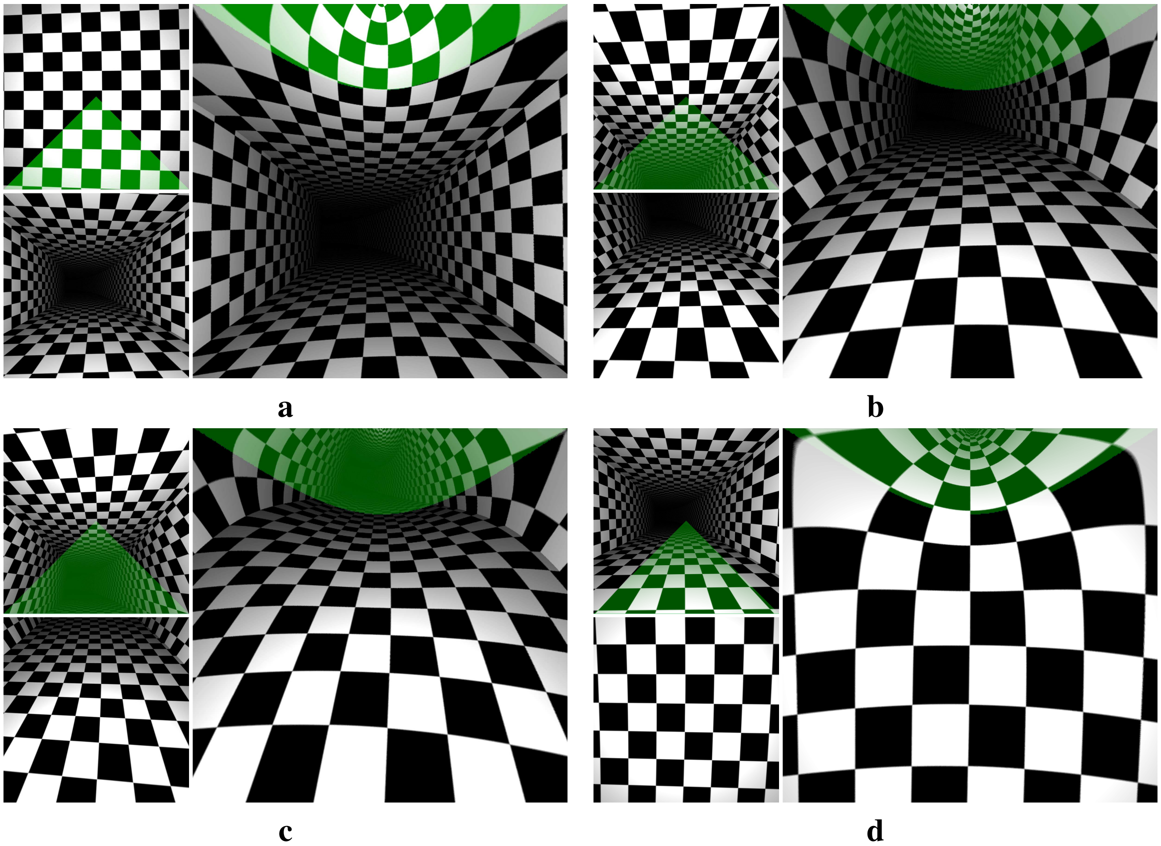

a **b**

c **d**

Figure 8.7: Navigation in the checkerboard tunnel with conformal visualization where the camera pans down in (a)-(d). Each triplet of images shows the original front view (lower-left), original top view (upper-left) and front view with conformal visualization (right).

camera panning down during the navigation with the 5-sided CAVE rendering target.

The performance of the conformal visualization scales almost linearly with the number of triangles in the scene after the tessellation. Depending on the scene complexity, its initial tessellation, the edge length threshold and the position of the user in the scene, we have observed reductions in the framerate of up to 50%.

8.4.2 Conformal visualization results

We also render the scene with the mesh template described in Fig. 8.4(c). Compared to the pinhole camera rendering in Fig. 8.8(a), the conformal visualization in Fig. 8.8(b) increases the field of view while preserving the local shapes of the objects in the scene. Our current mesh template utilizes only a hemisphere of the user's original field of view, however, that can be increased by augmenting the tiled array with additional screens on the top and the bottom. The resulting boundary of the screen geometry would then more closely resemble the original visibility boundary, which in turn would provide more uniform conformal visualization results.

a.No retargeting **b.**With conformal visualization

Figure 8.8: Conformal visualization results for a large tiled display. (a) The standard pinhole camera model with wide FOV leads to significant distortions near the periphery of the image. (b) In contrast, conformal visualization allows for 180 degree horizontal and vertical FOV while locally preserving the shapes in the data.

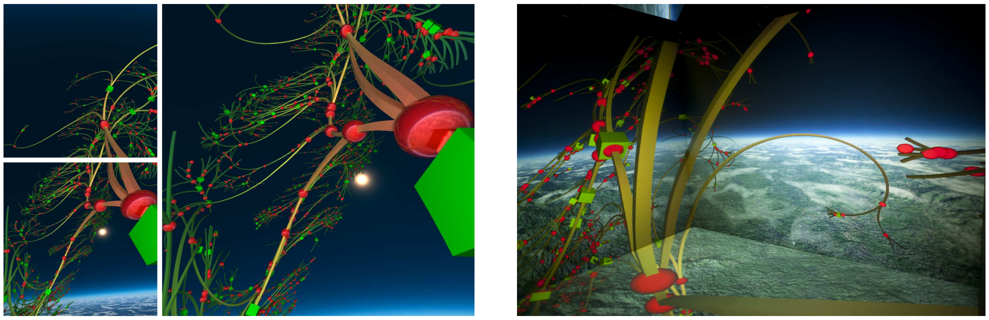

a.Navigation of densely connected data **b.**No retargeting

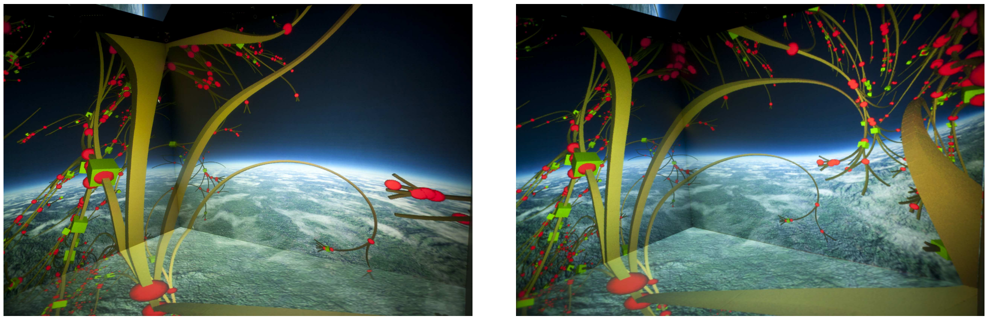

c.Retargeting to 5-sided CAVE **d.**Retargeting to 4-sided CAVE

Figure 8.9: Conformal visualization results.

Finally, one notable feature of the graph dataset presented in Fig. 8.9 and Fig. 8.8 is that it contains a large number of dense node clusters, which are difficult to explore using the traditional navigation paradigms.

Bibliography

[1] The digital michelangelo project. https://graphics.stanford.edu/projects/mich/, 1997.

[2] Repository of aim at shape project. http://shapes.aimatshape.net/, 1997.

[3] J. A. *Spin Images: A Representation for 3D Surface Matching*. PhD thesis, Carnegie Mellon University, Pittsburgh, PA, AUG 1997.

[4] A. Aleksandrov, N. Dairbekov, S. S. Kutateladze, and A. Sossinksky. *Convex polyhedra*, volume Springer Monographs in Mathematics. Springer, 2005.

[5] E. M. Andreev. Complex polyhedra in Lobachevsky spaces. *(Russian) Mat. Sb. (N.S.)*, 81(123):445–478, 1970.

[6] E. M. Andreev. Convex polyhedra of finite volume in Lobachevsky space. *(Russian) Mat. Sb. (N.S.)*, 83(125):256–260, 1970.

[7] M. Armstrong. *Basic Topology*. Undergraduate texts in mathematics. Springer, July 1983.

[8] P. J. BELONGIE S., MALIK J. Shape context: A new descriptor for shape matching and object recognition. *NIPS*, pages 831–837, 2000.

[9] A. Bobenko, U. Pinkall, and B. Springborn. Discrete conformal maps and ideal hyperbolic polyhedra. arXiv:1005.2698, 5 2010.

[10] Y. Brenier. Polar factorization and monotone rearrangement of vector-valued functions. *Com. Pure Appl. Math.*, 64:375–417, 1991.

[11] CGAL. Computational Geometry Algorithms Library. http://www.cgal.org.

[12] S. Chern. An elementary proof of the existence of isothermal parameters on a surface. *Proceedings of the American Mathematical Society*, 6(5):771–782, October 1955.

[13] B. Chow. The Ricci flow on the 2-sphere. *Journal of Differential Geometry*, 33(2):325–334, 1991.

[14] B. Chow, P. Lu, and L. Ni. *Hamilton's Ricci Flow*, volume 77 of *Graduate Studies in Mathematics*. AMS, 2006.

[15] B. Chow and F. Luo. Combinatorial Ricci flows on surfaces. *Journal Differential Geometry*, 63(1):97–129, 2003.

[16] J. R. CHUA C. S. Point signatures: A new representation for 3d object recognition. *Int.J.Comput.Vision*, 25:63–85, 1997.

[17] K. L. Clarkson and P. W. Shor. Applications of random sampling in computational geometry, ii. *Disc. & Comp. Geom.*, 4:387–421, 1989.

[18] J. Dai, X. Gu, W. Luo, S. tung Yau, and M. Zhang. Visualization of 2-dimensional ricci flow. *Pure and Applied Mathematics Quarterly*, 9(3):417–435, 2013.

[19] F. de Goes, K. Breeden, V. Ostromoukhov, and M. Desbrun. Blue noise through optimal transport. *ACM Trans. Graph. (SIGGRAPH Asia)*, 31(6), 2012.

[20] F. de Goes adn D.Cohen-Steiner, P. Alliez, and M. Desbrun. An optimal transport approach to robust reconstruction and simplification of 2d shapes. *Eurographics Sym. on Geometry Processing*, 30:1593–1602, 2011.

[21] M. P. DoCarmo. *Differential Geometry of Curves and Surfaces*. Pearson, 1 edition, February 1976.

[22] A. Dominitz and A. Tannenbaum. Texture mapping via optimal mass transport. *IEEE TVCG*, 16:419–433, 2010.

[23] F. H. F. Aurenhammer and B. Aronov. Minkowski-type theorems and least-squares clustering. *Algorithmica*, 2:61–76, 1998.

[24] B. Fischl, M. I. Sereno, and A. M. Dale. Cortical surface-based analysis II: Inflation, flattening, and a surface-based coordinate system. *NeuroImage*, 9(2):195 – 207, 1999.

[25] X. G. J. H. G Zou, J Hu. Authalic parameterization of general surfaces using lie advection. *IEEE Trans. on Visualization and Computer Graphics*, 17(2):2005–2014, 2011.

[26] Z. L. X. G. G Zou, J Hua and M. Dong. Intrinsic geometric scale space by shape diffusion. *IEEE Trans. on Visualization and Computer Graphics*, 15(6):1193–1200, 2009.

[27] C.-O. GAL R., SHAMIR A. Pose-oblivious shape signature. *IEEE Transactions on Visualization and Computer Graphics*, 13(2):261–271, 2007.

[28] G. L. J. P. H. GELFAND N., MITRA N. J. Robust global registration. *In Symposium on Geometry Processing*, (197-206), 2005.

[29] D. Glickenstein. Discrete conformal variations and scalar curvature on piecewise flat two and three dimensional manifolds. *Journal of Differential Geometry*, 87(2):201–238, 2011.

[30] X. Gu, R. Guo, F. Luo, J. Sun, and T. Wu. A discrete uniformization theorem for polyhedral surfaces ii. *arXiv:1401.4594*, 2014.

[31] X. Gu, F. Luo, J. Sun, and T. Wu. A discrete uniformization theorem for polyhedral surfaces. *arXiv:1309.4175*, 2013.

[32] X. Gu, F. Luo, J. Sun, and S.-T. Yau. Variational principles for minkowski type problems, discrete optimal transport, and discrete monge-ampere equations. *arXiv:1302.5472*, 2013.

[33] G. Guennebaud, B. Jacob, et al. Eigen. http://eigen.tuxfamily.org, 2010.

[34] S. Haker, L. Zhu, A. Tannenbaum, and S. Angenent. Optimal mass transport for registration and warping. *IJCV*, 60(3):225–240, 2004.

[35] R. Hamilton. Ricci flow on surfaces. *Mathematics and General Relativity, Contemporary Mathematics AMS, Providence, RI,*, 71:237–261, 1988.

[36] P. Henrici. *Applied and Computational Complex Analysis*, volume 3. John Wiley & Sons Inc., 1993.

[37] K. T. K. T. L. HILAGA M., SHINAGAWA Y. Topology matching for fully automatic similarity estimation of 3d shapes. *In Proc. SIGGRAPH*, 2001.

[38] H.Li, W.Zeng, J-M.Morvan, L.Chen, and X.Gu. Surface meshing with curvature convergence. *IEEE Transactions on Visualization and Computer Graphics*, 99(PrePrints):1, 2013.

[39] I. Izmestiev. A variational proof of alexandrov's convex cap theorem. Technical Report arXiv.org, March 06 2007.

[40] C. R. J. Jack, M. A. Bernstein, N. C. Fox, P. M. Thompson, G. Alexander, D. Harvey, B. Borowski, P. J. Britson, J. L. Whitwell, C. Ward, and e. al. The Alzheimer's disease neuroimaging initiative (ADNI): MRI methods. *J. of Mag. Res. Ima.*, 27:685–691, 2007.

[41] M. D. X. G. J.Hua, Z Lai and H. Qin. Geodesic distance-weighted shape vector image diffusion,. *IEEE Trans. on Visualization and Computer Graphics,*, 14(6):1643–1650, 2008.

[42] M. O. Jian Sun and L. Guibas. A concise and provably informative multi-scale signature based on heat diffusion. *Eurographics Symposium on Geometry Processing*, 28(5), 2009.

[43] M. Jin, J. Kim, F. Luo, and X. Gu. Discrete surface ricci flow. *IEEE Transactions on Visualization and Computer Graphics*, 14(5):1030–1043, 2008.

[44] L. V. Kantorovich. On a problem of Monge (russian). *Uspekhi Mat. Nauk.*, 3:225–226, 1948.

[45] P. Koebe. Kontaktprobleme der konformen abbildung. *Ber. Sächs. Akad. Wiss. Leipzig, Math. Phys. Kl.*, 88:141–164, 1936.

[46] K.Petkov, C.Papadopoulos, M.Zhang, AE.Kaufman, and X.Gu. Interactive visibility retargeting in vr using conformal visualization. *IEEE Transactions on Visualization and Computer Graphics*, 18(7):1027–1040, 2011.

[47] P. Li and S.-T. Yau. On the parabolic kernel of the Schrödinger operator. *Acta mathematics*, 156:153–201, 1986.

[48] G. I. LI X. Multi scale features for approximate alignment of point based surfaces. *In Symposium on Geometry processing*, pages 217–226, 2005.

[49] Y. Lipman and I. Daubechies. Surface comparison with mass transportation. *arXiv:0912.3488*, 2009.

[50] Y. Lipman, J. Puente, and I. Daubechies. Conformal wasserstein distance: Ii. computational aspects and extensions. *Journal of Math. Comp.*, 82:331–381, 2013.

[51] L. M. Lui, W. Zeng, T. Chan, S.-T. Yau, and X. Gu. Shape representation of planar objects with arbitrary topologies using conformal geometry. In *The 11th European Conference on Computer Vision (ECCV2010)*, Sep 5-11, 2010, Crete, Greece.

[52] F. Luo. Rigidity of polyhedral surfaces. *Journal of Differential Geometry*, 96(1):241–302, 2014.

[53] F. Luo, X. Gu, and J. Dai. *Variational Principles for Discrete Surfaces*. Advanced Lectures in Mathematics. High Education Press and International Press, 2007.

[54] W. Luo, Z. Su, M. Zhang, W. Zeng, J. Dai, and X. Gu. Shape signature based on ricci flow and optimal mass transportation. *Optical Engineering*, 53(11), 2014.

[55] R. R. M. Laplace-beltrami eigenfunctions for deformation invariant shape representation. *In Symposium on Geometry Processing*, pages 225–233, 2007.

[56] H. B. W. S. S. MANAY S., YEZZI A. J. Integral invariant signatures. *In Proceedings of ECCV*, pages 87–99, 2004.

[57] A. Marden and B. Rodin. *Computational methods and function theory (Valpara'iso,1989)*, volume 1435 of *Lecture Notes in Math.*, chapter On Thurston's formulation and proof of Andreev's theorem, pages 103–116. Springer, Berlin, 1990.

[58] Q. Merigot. A multiscale approach to optimal transport. *Comput. Graph. Forum*, 30:1583–1592, 2011.

[59] Q. Merigot. A comparison of two dual methods for discrete optimal transport. *Geometric Science of Information*, 8055:389–396, 2013.

[60] F. MÃl'moli. GromovâĂŞwasserstein distances and the metric approach to object matching. *Foundations of Computational Mathematics*, 11:417–487, 2011.

[61] M.Zhang, Y. Li, W. Zeng, and X. Gu. Canonical conformal mapping for high genus surfaces with boundaries. *Computers and Graphics*, 36(5):417–426, 2012.

[62] G. L. J. OVSJANIKOV M., SUN J. Global intrinsic symmetries of shapes. *Comput. Graph. Forum*, 27(5):1341–1348, 2008.

[63] H. Q.-X. Y. Y.-L. POTTMANN H., WALLNER J. Integral invariants for robust geometry processing. *Computer Aided Geometric Design*, 26(1):37–60, 2009.

[64] F. P. Preparata and S. J. Hong. Convex hulls of finite sets of points in two and three dimensions. *Commun. ACM*, 20:87–93, 1977.

[65] B. Rodin and D. Sullivan. The convergence of circle packings to the Riemann mapping. *Journal of Differential Geometry*, 26:349–360, 1987.

[66] R. Schneider. *Convex Bodies: the Brunn-Minkowski Theory*, volume Encyclopedia of Mathematics and its Applications. Cambridge University Press, 1993.

[67] R. Schoen and S.-T. Yau. *Lecture on Differential Geometry*, volume 1. International Press Incorporated, Boston, 1994.

[68] E. Sharon and D. Mumford. 2D-shape analysis using conformal mapping. *International Journal of Computer Vision*, 70:55–75, October 2006.

[69] W. P. Thurston. Geometry and topology of three-manifolds. *Princeton Lecture Notes*, 1976.

[70] W. P. Thurston. *The Geometry and Topology of 3-manifolds*. Princeton University Press, 1981.

[71] T.Rehman, E.Haber, G.Pryor, J.Melonakos, and A.Tannenbaum. 3d nonrigid registration via optimal mass transport on the gpu. *Medical Image Analysis*, 13:931–940, 2004.

[72] J. J. van Wijk. Image based flow visualization. In *SIGGRAPH '02: Proceedings of the 29th annual conference on Computer graphics and interactive techniques*, pages 745–754, New York, NY, USA, 2002. ACM Press.

[73] Y. Wang, M. Gupta, S. Zhang, S. Wang, X. Gu, D. Samaras, and P. Huang. High resolution tracking of non-rigid 3d motion of densely sampled data using harmonic maps. *International Journal of Computer Vision*, 76:283–300, 2007.

[74] Y. Wang, M. Gupta, S. Zhang, S. Wang, X. Gu, D. Samaras, and P. Huang. High resolution tracking of non-rigid motion of densely sampled 3d data using harmonic maps. *International Journal of Computer Vision*, 76(3):283–300, 2008.

[75] Z-X.He. Rigidity of infinite disk patterns. *Ann. of Math*, 149(1):1–33, 1999.

[76] W. Zeng and X. Gu. *Ricci Flow for Shape Analysis and Surface Registration*. SpringerBriefs in Mathematics. Springer New York, 2013.

[77] W. Zeng, X. Yin, M. Zhang, F. Luo, and X. Gu. Generalized Koebe's method for conformal mapping multiply connected domains. In *ACM Symposium on Solid and Physical Modeling (SPM'09)*, pages 89–100, 2009.

[78] M. Zhang, R. Guo, F. Luo, S. T. Yau, and X. Gu. The unified discrete surface ricci flow. *Graphic Model*, 76(5):321–339, 9 2014.

[79] L. Zhu, S. Haker, and A. Tannenbaum. Area-preserving mappings for the visualization of medical structures. In *MICCAI*, pages 277–284, 2003.

Appendices

Appendix A

Proof for the main theorem

In the appendix, we prove that the generalized Koebe's algorithm compute the uniformization of high genus surfaces with boundaries. Namely, S_k converges to a circle domain, when $k \to \infty$.

In the following, we prove the case for $g > 1$. The proof for the case $g = 1$ is very similar and simpler. The proof is based on the following idea, which is similar to the method in [36]. We lift the mappings to the universal covering space of $\bar{S}$, which are embedded on the hyperbolic space $\mathbb{H}^2$. At each step, one boundary component is transformed to a hyperbolic circle. Then the whole universal covering space of $\bar{S}$ can be reflected with respect to these circles. When the Koebe's iterations continue, the reflected images can be further reflected. All the reflected images almost cover the whole complex plane. The conformal mapping between original surfaces can be extended to all the reflected images, and eventually to the whole complex plane, which must be the identity under appropriate normalization condition.

A.1 Notations

The proof needs complicated notation system. In the following, we explain all of them in details.

The input topological surface is denoted as S with genus g, whose boundary components are:

$$\partial S = \Gamma^1 \cup \Gamma^2 \cup \Gamma^3 \cup \cdots \cup \Gamma^b.$$

We suppose the boundary components are Jordan curves and are well separated,and each boundary circle in the target circle domain has finite radius.In each step of *Koebe*'s iteration, the area of the each complement component in the fundamental polygon has finite area.There exists a closed topological surface $\bar{S}$, such that $S \subset \bar{S}$, so that the complements of S in $\bar{S}$ are topological disks. The fundamental group of $\bar{S}$ is denoted as $\pi_1(\bar{S})$, each element in the fundamental group is denoted as $\tau \in \pi_1(\bar{S})$.

Let $\bar{C}$ be the universal covering space of $\bar{S}$, the projection map is denoted as $\pi : \bar{C} \to \bar{S}$. Then the subsurface $C \subset \bar{C}$ is a covering space of S, where $C = \pi^{-1}(S)$. The deck transformation of S is isomorphic to the fundamental group of $\bar{S}$, $\pi_1(\bar{S})$.

Each boundary component Γ^i of S can be lifted to the covering space C, two such liftings differ by a deck transformation. The liftings of Γ^i are denoted as $\pi^{-1}(\Gamma^i) = \{\Gamma^{i,\tau} | \tau \in \pi_1(\bar{S})\}$. The boundary components of C are

$$\partial C = \{\Gamma^{i,\tau} | 1 \leq i \leq n, \tau \in \pi_1(\bar{S})\}.$$

In the Koebe's iteration algorithm, all the surfaces are Riemann surfaces with hyperbolic metric. Suppose at the k-th step, the resulting Riemann surface is S_k, the boundary components of S_k are $\Gamma_k^1, \Gamma_k^2, \cdots, \Gamma_k^b$. The covering space of S_k is denoted as C_k, the boundary components of C_k are

$$\partial C_k = \{\Gamma_k^{i,\tau} | \tau \in \pi_1(\bar{S})\}$$

S_k is a subsurface of a closed hyperbolic surface, $\bar{S}_k$, whose covering space is $\bar{C}_k$. $\bar{C}_k$ isometric to the hyperbolic space $\mathbb{H}^2$, represented as the upper half plane with Poincaré disk metric $ds = \frac{|dz|}{Imgz}$. This induces an isometric embedding of C_k into $\mathbb{H}^2$.

According to the uniformization theorem, for each S_k, there exists a hyperbolic surface $\tilde{S_k}$, and a conformal mapping $h_k : S_k \to \tilde{S_k}$, whose image is a circle domain. The universal covering space D_k of $\tilde{S_k}$ is isometric to $\mathbb{H}^2$. Then the conformal mapping between surfaces can be lifted to that between covering spaces. We use the same symbol to represent the lifted mapping

$$h_k : C_k \to D.$$

A.2 Schawrtz Reflection Principle

The key to the proof is the Schawtz Reflection principle.

A.2.1 Symmetry

In the following, we define the meaning of symmetry of two regions S and S' with respect to a closed curve Γ. If Γ is the unit circle, S' is the reflection image of S, the reflection is given by

$$z \to \frac{1}{\bar{z}}.$$

If Γ is not the unit circle, suppose there exists a conformal mapping f, such that $f(\Gamma)$ is the unit circle and the domain of f contains both S and S', $f(S)$ and $f(S')$ are symmetric with respect to the $f(\Gamma)$ defined above.

A.2.2 Reflection Principle

An analytic function defined on some open set in the upper half of the complex plane can be extended across the real line, in such a way that the extended to be an analytic function satisfies the symmetry equation

$$f(\bar{z}) = \overline{f(z)},$$

provided that the real part of $f(z)$ converges to 0 as z approaches the real line.

This can be generalized to the following version. Suppose S_1 is a planar domain, $\gamma_1 \subset S_1$ is a boundary component, which is a circle; similarly, S_2 is a planar domain, $\gamma_2 \subset S_2$ is a circular boundary component. $f : S_1 \to S_2$ is a conformal mapping. Let S'_k be the reflection of S_k with respect to the circle Γ_k, and the reflection is denoted as $\phi_k : S_k \to S'_k$. Then the conformal mapping $f : S_1 \to S_2$ can be extended to $F : S_1 \cup S'_1 \to S_2 \cup S'_2$,

$$F(z) = \begin{cases} f(z) & z \in S_1 \\ \phi_2 \circ f \circ \phi_1^{-1}(z) & z \in S'_1 \end{cases}$$

A more general reflection principle is as follows. Suppose γ_k's are not circles, S_k and S'_k are symmetric with respect to γ_k, then a conformal mapping $f : S_1 \to S_2$ can be extended to $F : S_1 \cup S'_1 \to S_2 \cup S'_2$ as well. Basically, the symmetry map is given by $\psi_k : S_k \to S'_k$, $\psi_k = f_k^{-1} \circ \phi_k \circ f_k$, where f_k maps γ_k to a circle, then

$$F(z) = \begin{cases} f(z) & z \in S_1 \\ \psi_2 \circ f \circ \psi_1^{-1}(z) & z \in S'_1 \end{cases}$$

A.3 Koebe's Iteration

Suppose at the k-th step, the resulting Riemann surface is S_k, the boundary components of S_k are $\Gamma_k^1, \Gamma_k^2, \cdots, \Gamma_k^b$. The covering space of S_k is denoted as C_k, the boundary components of C_k are

$$\partial C_k = \{\Gamma_k^{i,\tau} | \tau \in \pi_1(\bar{S})\}$$

Let us introduce a notion, if A and B are domain in the complex plane symmetric with respect to a simple closed curve c,we denote it by $A|B(c)$.The symmetric reflection of C_k with respect to $\Gamma_k^{i,\tau}$, if it defined,is denoted as $C_k^{(i,\tau)}$,ie.,

$$C_k | C_k^{(i,\tau)} (\Gamma_k^{i,\tau}).$$

The symmetric reflection of $C_k^{(i,\tau)}$ with respect to $\Gamma_k^{j,\eta}$, if it is defined is denoted as $C_k^{(i,\tau)(j,\eta)}$,ie.,

$$C_k^{(i,\tau)} | C_k^{(i,\tau)(j,\eta)} (\Gamma_k^{j,\eta}).$$

In general, the symmetric reflection of $C_k^{(i_1,\tau_1)(i_2,\tau_2)\cdots(i_{m-1},\tau_{m-1})}$ with respect to $\Gamma_k^{i_m,\tau_m}$ is

$$C_k^{(i_1,\tau_1)(i_2,\tau_2)\cdots(i_{m-1},\tau_{m-1})} | C_k^{i_1,\tau_1)(i_2,\tau_2)\cdots(i_{m-1},\tau_{m-1})(i_m,\tau_m)}$$

$$(\Gamma_k^{i_m,\tau_m}).$$

if $1 \le k \le b$, and $\tau \in \pi_1(\bar{S})$ the boundary component $\Gamma_k^{(k,\tau)}$ of C_k is a hyperbolic circle, then the symmetric reflection , $C_k^{(k,\tau)}$ is well defined. Furthermore, $C_k^{(i,\tau)}$ is always well defined, whenever

$k \geq i$. Similarly, when $k = b + j$, $\Gamma_k^{(j,\eta)}$ becomes a hyperbolic circle for the second time, then the second level symmetric reflection of $C_k^{(i,\tau)}$ with respect to $\Gamma_k^{(j,\eta)}$ is well defined, the image is $C_k^{(i,\tau)(j,\eta)}$. Then $C_k^{(i,\tau)(j,\eta)}$ is always well defined, whenever $k \geq b + j$. In general, if k is greater than mn, then the m level symmetric reflection images $C_k^{(i_1,\tau_1)(i_2,\tau_2)\cdots(i_m,\tau_m)}$'s are always well defined.

According to the uniformzation theorem, there exists a conformal mapping from S_k to a circle domain $\tilde{S}$. The covering space of $\tilde{S}_k$ on $\mathbb{H}^2$ is denoted as D. Because S_k and $\tilde{S}_k$ (C_k and D) are topologically equivalent, we use the same symbol to represent their corresponding boundary components. We also use the same notation to represent their corresponding symmetric reflection images. Assume $h_k : S_k \to \tilde{S}_k$ is the conformal mapping, which can be lifted to $H_k : C_k \to D_k$. According to the Schawtz reflection principle, H_k can be extended to the union of all symmetric reflection images. Define

$$\overline{C}_k := \bigcup \{C_k^{(i_1,\tau_1)(i_2,\tau_2)\cdots(i_m,\tau_m)} | 0 \leq m < \infty,$$

$$0 \leq i_1, i_2, \cdots, i_m < n, \tau_1, \tau_2, \cdots, \tau_m \in \pi_1(\bar{S})\}$$

$\overline{D}_k$ is define in the same way. Then H_k can be extended as a conformal mapping $\overline{H}_k : \overline{C}_k \to \overline{D}_k$.

A.4 Separation Module

From complex analysis, we know any doubly connected domain except the punctured plane is conformally equivalent to some annulus $r_1 < |z| < r_2$.

Definition 41. *(Modulus of an annulus) The modulus of the annulus $r_1 < |z| < r_2$ is defined to be*

$$\mu = r_2 / r_1$$

Remark: Usually the modulus of an annulus $r_1 < |z| < r_2$ is defined as $\frac{1}{2\pi} ln \frac{r_2}{r_1}$. Two doubly connected regions are conformally equivalent if and only if they have the same modulus.

To show that the mapping from C_k to D can be extended to an automorphism of $\mathbb{C}$, we need the following lemma which is given in [36](Lemma 17.7 C, page 503).

Lemma 20. *Let A be a doubly connected region with finite modulus $\mu > 1$, and let A be bounded on the outside by a Jordan curve γ^2 and on the inside by a Jordan curve γ^1. Then*

$$Area(\gamma^1) \leq \mu^{-2} Area(\gamma^2) \tag{A.4.1}$$

$$(Diam(\gamma^1)) \leq \frac{\pi}{2 \log(\mu)} Area(\gamma^2) \tag{A.4.2}$$

where $Area(\gamma)$ is the area enclosed by the Jordan cure γ and $Diam(\gamma)$ is the diameter of the Jordan cure γ.

In the circular domain $\tilde{S}$, we can expand each boundary circle $\tilde{\Gamma}^i(i = 1, \cdots, b)$ simultaneously by a factor $\rho > 1$ under the given metric. and at the time when two of the inflated circles $\hat{\Gamma}^i(i = 1, \cdots, b)$ touch each other or one of the circles touches itself, we get a factor ρ, which we call the separation module of $\tilde{S}$. And also we get b annulus regions which are bounded by $\tilde{\Gamma}^i$ and $\hat{\Gamma}^i$, which we denote as A^i. For the case $\tilde{S}$ with hyperbolic metric, if the boundary circle $\tilde{\Gamma}^i$ has the hyperbolic radius $\{r_i | i = 1, \cdots, b\}$, then we get b doubly connected regions which are concentric annuluses in the hyperbolic metric. Using *Mobiüs* transformation, we can map each doubly connected region conformally to annulus $\{\tanh(r_i) < |z| < \tanh(\rho r_i) | i = 1, \cdots, b\}$. Notice that $\{\tanh(\rho r_i)/\tanh(r_i) | i = 1, \cdots, b\}$ are the conformal modulus of the b doubly connected region, which are strictly bigger than 1. For the above b doubly connected region, we can also reflect them with respect to the inner circles $\tilde{\Gamma}^i$ to get $\hat{\Gamma}^{(i,i)}$. And because the modulus is conformal invariant, then after reflection the modulus doesn't change, then we get b doubly connected regions with modulus $\{\tanh^2(\rho r_i)/\tanh^2(r_i) | i = 1, \cdots, b\}$. While for the case $\tilde{S}$ with Euclidean metric, we get b doubly connected regions which are annuluses with the same modulus ρ^2 by the same process.

Now we consider on the covering space $\bar{D}$, the doubly connected region bounded by $\tilde{\Gamma}^{i,\tau_1}$ and $\hat{\Gamma}^{i,\tau_1}$ have the same modulus as the doubly connected region bounded $\tilde{\Gamma}^{i,\tau_2}$ and $\hat{\Gamma}^{i,\tau_2}$ for any $(\tau_1, \tau_2 \in \pi_1(\tilde{S}))$, because there exist a *Mobiüs* transformation between them.

Using above lemma, we can estimate the total area bounded by the level m reflected circles in one fundamental polygon. Here we only show the level one case, this step can do recursively. Inside circle $\tilde{\Gamma}^{(i,\tau)}$, the circles bound some positive area of all level one reflection of $\bar{D}$ are $\tilde{\Gamma}^{(j,\xi)(i,\tau)}$, then we have

$$\begin{aligned} \textstyle\sum_{(j,\xi)\neq(i,\tau)} \quad & Area(\tilde{\Gamma}^{(j,\xi)(i,\tau)}) \\ \leq \quad & \mu^{-2} \sum_{(j,\xi)\neq(i,\tau)} Area(\hat{\Gamma}^{(j,\xi)(i,\tau)}) \\ \leq \quad & \mu^{-2} Area(\hat{\Gamma}^{(i,\tau)(i,\tau)}) \\ \leq \quad & \mu^{-4} Area(\tilde{\Gamma}^{(i,\tau)}) \end{aligned} \tag{A.4.3}$$

where $\mu = Min\{\tanh(\rho r_i)/\tanh(r_i) | i = 1, \cdots, b\} > 1$.

So from above estimation, the total area of the complement of the level m reflected region will shrink by a factor at least $\mu^4 > 1$ comparing the $m - 1$ level. Then when m goes to ∞, the total area will goes to zero, also from the above lemma, the diameter of the boundaries of the level m reflected region go to zero as $m \to \infty$. Now we consider in the domain $\bar{C}_k (k = mb)$, using refection principle, we have the following similar estimation for level one reflected region

$$\sum_{(j,\xi)\neq(i,\tau)} Area(\Gamma^{(j,\xi)(i,\tau)}) \leq \mu^{-4} Area(f_b \circ \cdots \circ f_1(\Gamma^{(i,\tau)})) \tag{A.4.4}$$

where f_i is the ith step *Koebe*'s iteration.

Then from the assumption, both the area and diameter of each boundary component of the level m reflected region of $\bar{C}$ will go to 0, when m goes to ∞.

A.5 Convergence proof

From the discussion in the above section, we know that for when the iteration number k goes to ∞, the regions which still can not be extended will shrink to a point set P, which is the limit set of the reflections, and the image of these regions also will shrink to a point set Q, and there is a one-one corresponding between these two point sets. We denote limit of the mapping $h_k(k \to \infty)$ as h_∞. If $p \in P$ is a limit point attained from the nested Jordan curves $\gamma_1 \subset \gamma_2 \cdots$, where γ_i is a boundaries of the level i reflected region, then there is a q is the limit point attained from the nested circles $\tilde{\gamma}_1 \subset \tilde{\gamma}_2 \cdots$, where $\tilde{\gamma}_i = h_\infty(\gamma_i)$. Then we can extend the mapping h_∞ to the limit points for $h_\infty(p) = \lim_{i\to\infty} \frac{1}{2\pi i} \int_{\gamma_i} \frac{h_\infty(z)}{z-p} = q \lim_{i\to\infty} \frac{1}{2\pi i} \int_{\gamma_i} \frac{1}{z-p} = q$.

Now the conformal mapping h_∞ is well defined except for the reflection curves of the unit circle with respect to the boundary circles for hyperbolic case, and the reflection points of the ∞ for Euclidean case. For the latter case, there also a similar one-one corresponding to extend the mapping to the whole complex plane except ∞, then h_∞ is just a *Mobiüs* transformation. For the hyperbolic case, notice that the unit circle is the boundary of *Poincaré* disk, which means this part is what we can left to be undefine, h_∞ can be extended to a automorphism of the *Poincaré* disk, which means it is just a *Mobiüs* transformation. The complement of the union of all levels of reflection images is a Cantor set, when k goes to ∞, which is the limit set of the reflection group generated by inversion in each circles. Similarly, the complement of the union of all levels of reflection images of $\tilde{C_k}$ is a Cantor set, when k goes to ∞ as well. (This is from the fact that: the area of each connected component in the complement of the union of all levels of reflection images of $\tilde{C_k}$ goes to 0, when k goes to ∞; and then based on the Lemma 17.7 C ([36] page 503), the diameter of each connected component of the complement of the union of all levels of reflection images of $\tilde{C_k}$ also goes to 0 when k goes to ∞.) Now we have a conformal map $h_\infty : \mathbb{C} \setminus C_1 \to \mathbb{C} \setminus C_2$, where C_1 and C_2 are two Cantor sets. And from the sequences of reflection, there is a one-one corresponding from a point $p \in C_1$ to a point $q \in C_2$, then we can extend the map h_∞ continuously to the whole complex plane just let $h_\infty(p) = q$. Then h_∞ is a conformal automorphism of the whole complex plane $\mathbb{C}$, therefore it is a *Möbius* transformation. Therefore C_∞ is a circle domain Namely S_k converges to a circle domain on a Riemann surface, when $k \to \infty$.

Appendix B

Implementation of Unified Surface Ricci flow Algorithm

In the appendix, we explain the unified surface Ricci flow algorithm 7 in details, and reorganize all the formulae necessary for the coding purpose.

```
Algorithm 7: Unified Surface Ricci Flow
Input: The inputs include:
    1. A triangular mesh $\Sigma$, embedded in $\mathbb{E}^3$;
    2. The background geometry, $\mathbb{E}^2$, $\mathbb{H}^2$ or $\mathbb{S}^2$;
    3. The circle packing scheme, $\varepsilon \in \{+1, 0, -1\}$;
    4. A target curvature $\bar{K}$, $\sum \bar{K}_i = 2\pi\chi(\Sigma)$ and $\bar{K}_i \in (-\infty, 2\pi)$.
    5. Step length $\delta t$
Output: A discrete metric conformal to the original one, which realizes the target curvature $\bar{K}$.
 1: Initialize the circle radii $\gamma$, discrete conformal factor $u$ and conformal structure coefficient $\eta$, obtain the initial
    circle packing metric $(\Sigma, \gamma, \eta, \varepsilon)$
 2: while $\max_i |\bar{K}_i - K_i| > threshold$ do
 3:     Compute the circle radii $\gamma$ from the conformal factor $u$
 4:     Compute the edge length from $\gamma$ and $\eta$
 5:     Compute the corner angle $\theta_i^{jk}$ from the edge length using cosine law
 6:     Compute the vertex curvature $K$
 7:     Compute the Hessian matrix $H$
 8:     Solve linear system $H\delta u = \bar{K} - K$
 9:     Update conformal factor $u \leftarrow u - \delta t \times \delta u$
10: end while
11: Output the result circle packing metric.
```

Step 1. Initial Circle Packing (γ, η) Depending on different schemes, the initialization of the circle packing is different. The mesh has induced Euclidean metric l_{ij}. For inversive distance circle packing, we choose

$$\gamma_i = \frac{1}{3} \min_j l_{ij},$$

	u_i	Edge Length l_{ij}	$\tau(i,j,k)$	$s(x)$
$\mathbb{E}^2$	$\log\gamma_i$	$l_{ij}^2 = 2\eta_{ij}e^{u_i+u_j} + \varepsilon_i e^{2u_i} + \varepsilon_j e^{2u_j}$	$\frac{1}{2}(l_i^2 + \varepsilon_j\gamma_j^2 - \varepsilon_k\gamma_k^2)$	x
$\mathbb{H}^2$	$\log\tanh\frac{\gamma_i}{2}$	$\cosh l_{ij} = \frac{4\eta_{ij}+(1+\varepsilon_i e^{2u_i})(1+\varepsilon_j e^{2u_j})}{(1-\varepsilon_i e^{2u_i})(1-\varepsilon_j e^{2u_j})}$	$\cosh l_i \cosh^{\varepsilon_j}\gamma_j - \cosh^{\varepsilon_k}\gamma_k$	$\sinh x$
$\mathbb{S}^2$	$\log\tan\frac{\gamma_i}{2}$	$\cos l_{ij} = \frac{4\eta_{ij}+(1-\varepsilon_i e^{2u_i})(1-\varepsilon_j e^{2u_j})}{(1+\varepsilon_i e^{2u_i})(1+\varepsilon_j e^{2u_j})}$	$\cos l_i \cos^{\varepsilon_j}\gamma_j - \cos^{\varepsilon_k}\gamma_k$	$\sin x$

Table B.1: Formulae for $\mathbb{E}^2$, $\mathbb{H}^2$ and $\mathbb{S}^2$ background geometries.

this ensures all the vertex circles are separated. For Yamabe flow, we choose all γ_i to be 1. For virtual radius circle packing, we choose all γ_i's to be 1. Then γ_{ij} can be computed using the l_{ij} formula in Tab. B.1.

Step 3. Circle Radii γ The computation for circle radii from conformal factor uses the formulae in the first column in Tab.B.1.

Step 4. Edge Length l The computation of edge lengths from conformal factor u and conformal structure coefficient η uses the formulae in the 2nd column in Tab.B.1

Step 5. Corner Angle θ The computation from edge length l to the corner angle θ uses the cosine law formulae,

$$\begin{array}{rcll} l_k^2 &=& \gamma_i^2+\gamma_j^2-2l_il_j\cos\theta_k & \mathbb{E}^2 \\ \cosh l_k &=& \cosh l_i \cosh l_j - \sinh l_i \sinh l_j \cos\theta_k & \mathbb{H}^2 \\ \cos l_k &=& \cos l_i \cos l_j - \sin l_i \sin l_j \cos\theta_k & \mathbb{S}^2 \end{array}$$

Step 6. Vertex Curvature K The vertex curvature is defined as angle deficit

$$K(v_i) = \begin{cases} 2\pi - \sum_{[v_i,v_j,v_k]}\theta_i^{jk} & v_i \notin \partial\Sigma \\ \pi - \sum_{[v_i,v_j,v_k]}\theta_i^{jk} & v_i \notin \partial\Sigma \end{cases}$$

Step 7. Hessian Matrix H

$$\frac{\partial(\theta_i,\theta_j,\theta_k)}{\partial(u_i,u_j,u_k)} = -\frac{1}{2A}L\Theta L^{-1}D,$$

where

$$A = \sin\theta_i s(l_j)s(l_k),$$

and

$$L = diag(s(l_i), s(l_j), s(l_k)),$$

and

$$D = \begin{pmatrix} 0 & \tau(i,j,k) & \tau(i,k,j) \\ \tau(j,i,k) & 0 & \tau(j,k,i) \\ \tau(k,i,j) & \tau(k,j,i) & 0 \end{pmatrix}.$$

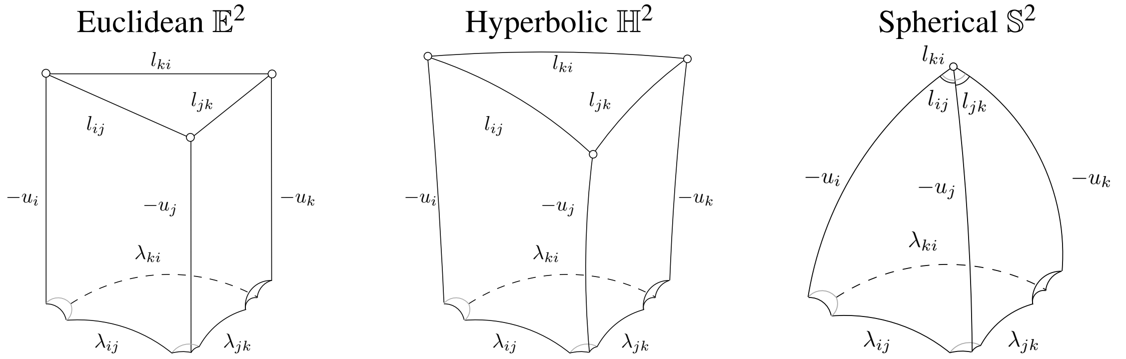

Inversive Distance Circle Packing

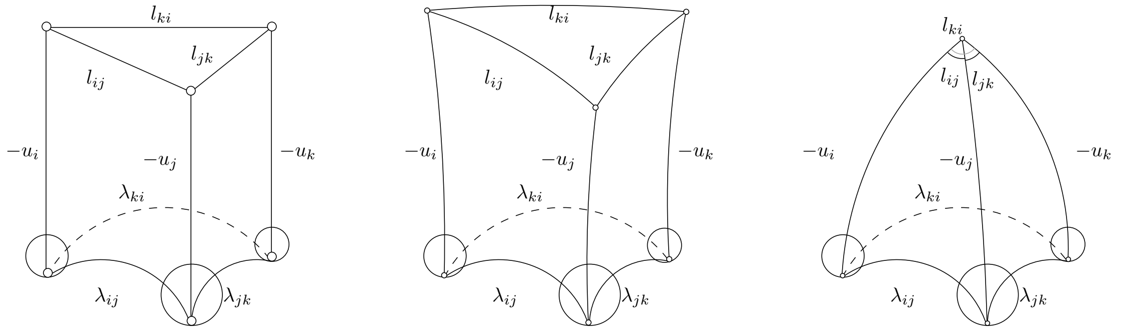

Yamabe flow

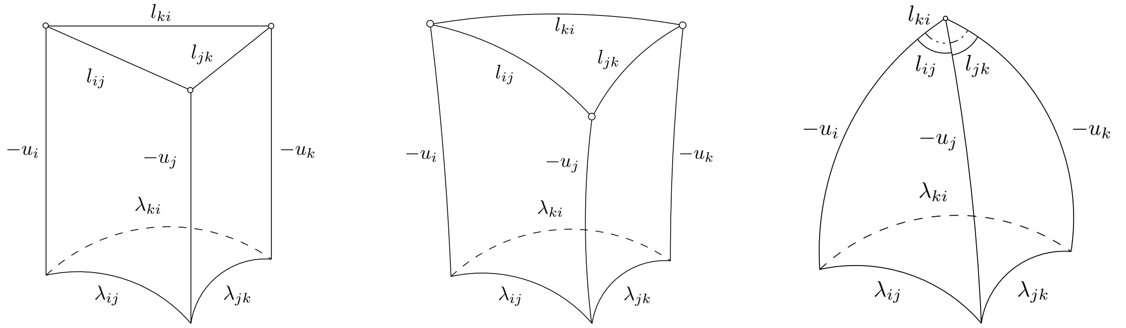

Virtual radius Circle Packing

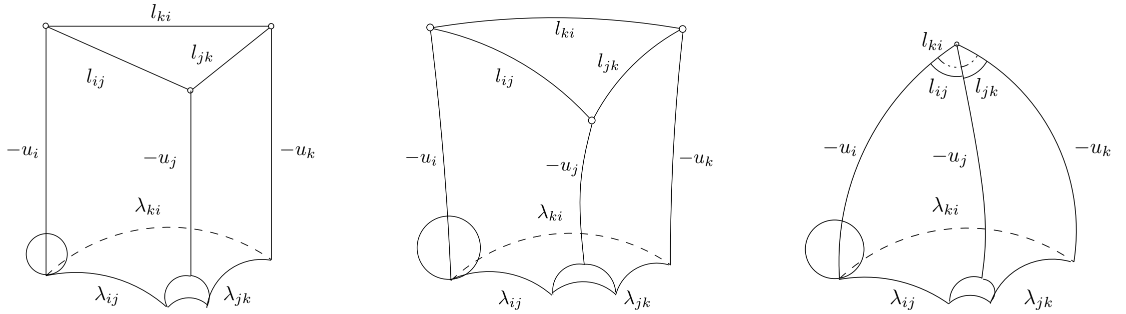

Mixed type schemes

Figure B.1: Geometric interpretation to discrete Ricci energy - volumes of generalized hyperbolic tetrahedra.

Step. 8 Linear System If the Σ is with $\mathbb{H}^2$ background geometry, then the Hessian matrix H is positive define; else if Σ is with $\mathbb{E}^2$ background geometry, then H is positive definite on the linear subspace $\sum_i u_i = 0$. The linear system can be solved using any sparse linear solver, such as Eigen [33].

For discrete surface Ricci flow with topological surgeries, we can add one more step right after step 4. In this new step, we modify the connectivity of Σ to keep the triangulation to be (Power) Delaunay. This will greatly improves the robustness as proved in [31] and [30].

Index